UNIVERSITY OF COPENHAGEN
FACULTY OF SCIENCE

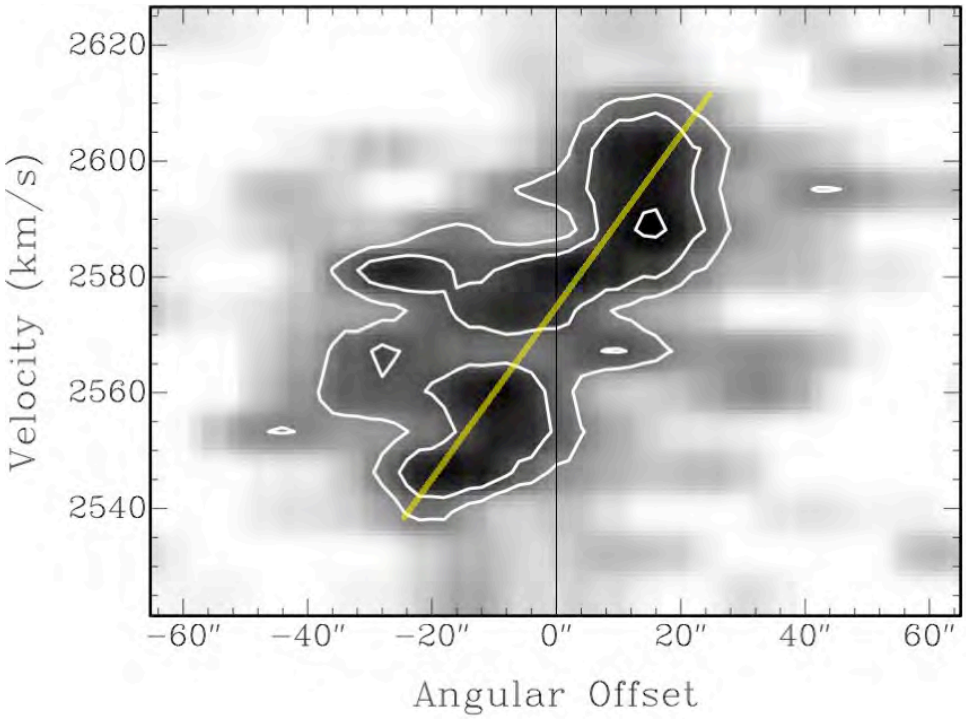

PhD thesis

Maryam Arabsalmani

Gas Kinematics in GRB Host Galaxies

Supervisors: Palle Møller (ESO) and Johan P. U. Fynbo (NBI)

Handed in: 21. October 2016

Dansk abstrakt

Universets stjernedannelseshistorie er et af de mest komplekse og interessante kapitler i vores bestræbelse på at forstå galaksedannelse og udvikling. Gammaglimt (Engelsk: gamma-ray bursts, GRBs) er fyrtårn til aktivt stjernedannende galakser med rødsforskydninger nær nul og tilbage til den kosmiske morgenskumring, da de første galakser opstod. Ydermere giver de adgang til en enestående metode til at udvælge galakser uden lysstyrkebias da GRB udvælgelsen af galakser er urelateret til lysstyrken af værtsgalaksen. Selv ved de højeste rødforskydninger, hvor værtsgalakserne ofte er for svage til at kunne blive detekteret, da kan andre af deres egenskaber udledes fra de absorptionslinjer deres interstellare stof giver anledning til i spektrene af GRBernes efterglød er. Derfor er GRBer uvurderlige værktøjer for undersøgelsen af Universets stjernedannelseshistorie tilbage til de tidligste kosmiske tider.

For dette formål er få et fyldestgørende billede af samspillet mellem stjernedannelsen og dens brændstof, den neutrale gas, i GRB-udvalgte galakser. Ydermere er det af største vigtighed at undersøge om denne klasse af galakser adskiller sig fra den generelle population af stjernedannende galakser (d.v.s. at afklare om GRB værtsgalakser udgør en særskilt galaksepopulation), før vi kan gøre os håb om at generalisere konklusioner fra denne særlige population til populationen af stjernedannende galakser som helhed.

I denne PhD afhandling fokuserer jeg på kinematikken af gassen i GRB værtsgalakser. Dette særlige område giver anledning til interessante indsigter i GRB værtsgalaksepopulationen specielt og i galaksedannelse og udvikling generelt.

For et stort katalog af GRB værtsgalakser benytter jeg den ”rumligt midlede” hastighedsfordeling af gassen som måles fra et integreret spektrum. Dette gøres v.h.a. både absorptions- og emissionslinjer som afspejler kinematikken af hhv. den neutrale og den ioniserede gas. Jeg har også udmålt et kort over 21-cm strålingen fra neutral hydrogen for en GRB værstgalakse (det første sådanne studium for en galakse af denne klasse). Dette kort giver mulighed for på én gang og med høj hastighedsopløsning at studere den rumlige fordeling og kinematik af den neutrale gas.

For det store katalog af GRB værstgalakser finder jeg, at den rumligt midlede hastighed korrelerer med metalliciteten i begge gasfaser (neutral og ioniseret). Dette indikerer en underligende masse-metallicitetsrelation. Jeg finder også, at hastighedsbredderne i de to gasfaser korrelerer med hinanden, hvilket ligeledes peger på en forbindelse mellem gaskinematikken og masse. Dette giver også information om hvordan metalliciteter bestemt fra absorptions- og emissionslinjer kan afvige fra hinanden. Endelig viser jeg i et konkret eksempel, hvordan hastighedsbredderne i begge gasfaser kan bruges som et mål for den totale stjernemasse i GRB værtsgalakser.

Jeg sammenligner skaleringsrelationer for det store katalog af GRB værtsgalakser med tilsvarende for andre galaksepopulationer. GRB værtsgalakser viser sig at følge samme hastigheds-metallicitetskorrelation som Dæmpede Lyman-α Absorbergalakser som er en population af galakser ved høj rødforskydning som detekteres i spektre af kvasarer. Jeg viser også, at GRB værtsgalakser følger samme masse-metallicitetsrelation som den generelle population af stjernedannende galakser. Dette er i modstrid med adskillige tidligere studier som har fundet, at GRB værtsgalakser falder udenfor den generelle masse-metallicitetsrelation.

For den enkeltstående GRB værtsgalakse med rumligt opløst hastighedsfelt fra 21-cm observationer udviser den rumligt opløste kinematik et forstyrret hastighedsfelt i hvilket mere end 20% af gassen har et andet bevægelsesmønster end gassen i den primære gasdisk. Et sådant meget forstyrret hastighedsfelt kan kun være resultatet af et galaksesammenstød. Ydermere detekterer jeg en hydrogenklump omkring 12 kpc fra galaksen, som synes at rotere sammen med den primære gasdisk og muligvis er relateret til galaksesammenstødet. Dette underbygger, at jeg i studiet af det store katalog af GRB værtsgalakser finder en antydning af, at galaksesammenstød også mere generelt må spille en rolle for kinematikken i GRB værtsgalakser.

Abstract

The star formation history of the Universe is one of the most complex and interesting chapters in our quest to understand galaxy formation and evolution. Gamma Ray Bursts (GRBs) are beacons of actively star forming galaxies from redshifts near zero back to the cosmic dawn. In addition, they provide a unique method for selecting galaxies without a luminosity bias as the GRB detectability is unrelated to the brightness of the host galaxy. Even at the highest redshifts, where the hosts are often too faint to be detected in emission, their properties can be inferred from the absorption features that their interstellar media imprint on the GRBs' spectra. Hence they are invaluable tools to probe the star formation history of the Universe back to the earliest cosmic epochs.

To this end, it is essential to achieve a comprehensive picture of the interplay between star formation and its fuel, neutral gas, in GRB selected galaxies. Moreover, it is crucial to investigate whether this galaxy population differs from the general population of star forming galaxies (if GRB hosts are a distinct galaxy population), before applying the findings from this selected population to the general population of galaxies.

In this thesis I focus on the gas kinematics in GRB host galaxies. This niche area of study provides interesting insights into the GRB host population as well as galaxy formation and evolution.

For a large sample of GRB hosts, I use the 'spatially averaged' velocity of gas which is measured from an integrated spectrum. This is done using both absorption and emission lines, tracing the gas velocity in neutral and ionised phases respectively. I also map the HI 21 cm emission line for a GRB host galaxy (first study of its kind). This allows studying the spatial distribution and the kinematics of the atomic gas simultaneously with a high velocity resolution.

For the large GRB sample, I find the spatially averaged velocity to correlate with metallicity in both gas phases. This is an indicator of a mass-metallicity relation. Moreover, the velocity widths in the two gas phases correlate with each other which too points towards a relation between gas kinematics and mass. This also provides information on how the metallicities measured from absorption and emission methods differ from each other. Finally, in a direct study I show that gas velocity widths in both phases can be used as a proxy of stellar mass in these galaxies.

I compare the large GRB host sample to other populations of galaxies using scaling relations. I find GRB hosts to follow the same velocity-metallicity correlation as Damped Lyman-α galaxies which are a population of high redshift galaxies detected in the sightlines of quasars. I also show that GRB hosts obey the same mass-metallicity relation as the general population of star-forming galaxies. This is contradictory to several previous studies that claimed GRB hosts to be below the general mass-metallicity relation.

For the sole GRB host with spatially resolved velocity field from HI 21 cm observations, the kinematically resolved data reveal disturbed gas with more than 20% of the gas mass being offset in velocity from the main gas disk. Such significantly massive offset gas could only be the remnant of a minor merger. In addition, I detect an HI knot about 12 kpc away from the galaxy, rotating aligned with the main gas disk which is possibly related to the merging event. This corroborates the fact that using scaling relations of the large GRB sample I find indication of merging systems being responsible for the kinematic characteristics of gas in GRB hosts galaxies.

Contents

List of Figures

List of Tables

Chapter 1

Introduction

1.1 Gamma Ray Bursts

1.1.1 What a GRB is

Gamma Ray Bursts (GRBs) are bright flashes with the peak energy in the γ-ray band, detected so far at redshifts ranging from $z = 0.0087$ (for GRB 980425, Fynbo et al., 2000) to $z = 8.23$ (spectroscopically confirmed redshift for GRB 090423, Tanvir et al., 2009). Their serendipitous discovery in 1967 was actually announced in 1973 (Klebesadel et al., 1973; Mazets et al., 1974). Since then, theoretical and observational efforts have been dedicated to understand the origin of these energetic phenomena. This includes the launching of several dedicated satellites to observe these extremely bright bursts: The Burst And Transient Source Experiment (BATSE, 1991-2000), *Swift* (2004), and *Fermi* (2008).

GRBs were initially thought to come from sources within the Milky Way. But their isotropic distribution on sky (with no dipole and quadrupole components) pointed to their cosmological origin (see Fig. 1.1). The GRB radiation starts with an intense and short emission in gamma ray with a low energy tail in X-ray (and longer wavelengths). This is known as 'prompt emission'. The prompt X-ray emission smoothly continues into the decaying 'afterglow' emission (lower-energy and longer-lasting) which goes all the way to radio wavelengths.

The prompt emission can last from only a few percent of a second to several hundreds of seconds. This duration was found to have a bimodal distribution, suggesting two distinct GRB populations (see Piran, 1999, and references therein). In fact based (mainly) on how long the prompt emission last, GRBs are divided to two categories: short (less than 2 seconds which usually have harder spectra) and long (more than 2 seconds) duration GRBs. The life-time of the afterglow varies with wavelength. X-ray and optical afterglows usually fade away fast and can't be followed a few weeks after the burst , while radio afterglows have been detected several years after the explosions. The presence of the bright afterglow leads to accurately locating the GRB positions and hence makes it possible to identify the galaxies hosting GRBs.

The GRB prompt emission is fitted well with a Band function (Band et al., 1993) in wavelength space: a broken power-law with a smooth joint. Afterglow spectrum too has the simple power law shape in wavelength space. When the afterglow emission passes through the GRB host galaxy several absorption features from the material in the inter stellar medium get imprinted on the spectrum. These features can be detected in optical wavelengths from the ground, making it possible to infer the host galaxy properties. Similarly, absorption profiles caused by the intervening systems

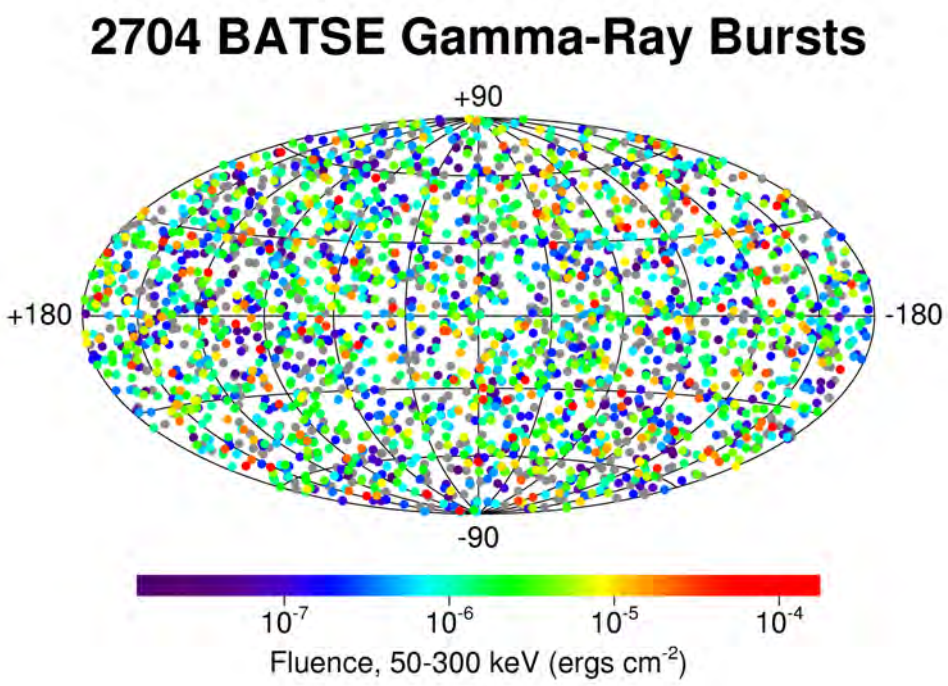

Figure 1.1: The locations of a total of 2704 Gamma-Ray Bursts recorded with the Burst and Transient Source Experiment on board NASA's Compton Gamma-Ray Observatory during its nine-year mission (isotropic distribution on sky). The map is taken from http://www.batse.msfc.nasa.gov/batse/grb/skymap/.

(at redshifts lower than the GRB redshift) provide information on the intervening galaxies in the GRB sightlines. The simple shape of the afterglow emission makes it possible to extract accurate information about the absorption profiles in the spectrum.

1.1.2 GRB progenitors

It has been proposed that the formation of a black hole or a magnetar with the accretion disk around acts as the inner engine that produces a GRB. This process is believed to be different for short and long GRBs. Short GRBs are likely to be the production of merging binary systems (Neutron star binary mergers or neutron star-black hole binary mergers), while long duration GRBs are believed to be produced as a result of the collapses of a single stars with very large masses and angular momentums (known as collapsar model).

The collapsar model, the most believed model for long duration GRB production, was first proposed by Woosley (1993) (see also Zhang et al., 2003; MacFadyen and Woosley, 1999; Aloy et al., 2000). In this model, the core of a rotating massive star ($M > 30M_{\odot}$) collapses to a black hole and creates an accretion disk. This is followed by leaking of the stellar material through a collimated jet along the rotation axis. The powerful jet with relativistic speed penetrates the stellar envelope and produces a GRB.

The requirement for sufficient angular momentum in the collapsar model puts constraints on the metallicity of the progenitor star. Several studies proposed that GRBs should be more probable in regions of low metallicity as massive metal rich stars do not retain sufficient angular momentum due to the mass loss through their strong winds (see Woosley and Heger, 2006, and references therein). On the other hand, the slow merger of a binary system, which is less metal-sensitive, seems to be a possible but a less likely channel for long-GRB production (Langer and Norman, 2006; Podsiadlowski et al., 2010). Observational evidences of finding long-GRBs in star-forming regions strengthened the links between their progenitors and massive stars and favoured the single star model to the merging binary model (see Paczyński, 1998, , and also references mentioned in section 1.2.1). The single star picture was also favoured by the young ages ($\lesssim 10$ Myr) found for the dominant stellar populations in GRB hosts (e.g. Chary et al., 2002; Christensen et al., 2004). Finally, the observed GRB-supernova connection presented the most direct evidence of the physical link between GRB progenitors and massive stars (see Hjorth and Bloom, 2012, and references therein).

1.2 GRB selected galaxies

The fundamental differences between the required environmental conditions for the formation of the two GRB population leads to the their distinct host galaxy populations. In this section I briefly discuss some of the findings in the field of researching host galaxies of long-duration GRBs. ***This thesis is about long duration GRBs and hereafter the term 'GRB' refers only to long duration GRBs.***

1.2.1 Star formation

The origin of GRBs in massive stars points to recent star formation activities in GRB host galaxies. Indeed, initial studies of a few GRB hosts revealed extremely blue galaxies with signature of young and very massive stars (see Fruchter et al., 1999; Bloom et al., 1999; Vreeswijk et al., 2001a, for host galaxies of GRBs 990123, 980326, 990510 and 990712). This was confirmed by Le Floc'h et al. (2003) who presented the photometric properties of 19 GRB hosts in a redshift range of $0.4 \sim< z <\sim 4.5$ and found them to exhibit very blue colours, comparable to those of the faint blue star-forming sources at high redshifts. Moreover, a few years later Fruchter et al. (2006) carried out the HST imaging of 42 GRB host galaxies and showed that GRBs occur in the very brightest regions of their hosts, ie. the most intensely star forming regions.

Initial attempts to investigate the star formation properties of GRB hosts were undertaken for individual cases using the OII emission line as well as radio and sub-mm measurements (Djorgovski et al., 1998, 2001; Berger et al., 2001; Frail et al., 2002; Vreeswijk et al., 2001b,a). Sokolov et al. (2001) presented the SEDs of 5 GRB hosts which were found to be best fitted by template SEDs of star-burst galaxies. Chary et al. (2002) measured the star formation rates of a sample of 7 GRB host galaxies ($0.6 \sim< z <\sim 3.4$) and showed all of them to have specific star formation rates (sSFRs) higher than that for typical nearby star-burst galaxies (median sSFR of $15\,\mathrm{Gyr}^{-1}$, see Fig. 1.2). Christensen et al. (2004) carried out a detailed study of 10 GRB host galaxies in the redshift range $0.4 \sim< z <\sim 2.0$ and found all the hosts to have SEDs similar to young star-burst galaxies with sSFRs higher than the average sSFR of field galaxies. Savaglio et al. (2009b) extended this study to 46 host galaxies and found the SFRs to vary in a range of $0.01 - 36\,\mathrm{M}_{\odot}\mathrm{yr}^{-1}$, with a median sSFR of $0.8\,\mathrm{Gyr}^{-1}$, similar to Lyman break galaxies, but more than an order of magnitude larger than the general population of star forming galaxies. Similar findings were presented by Svensson

et al. (2010) who showed that GRBs occur in galaxies with specific and surface star formation rates higher than those of core-collapse (CC) Supernova (SN) hosts. Castro Cerón et al. (2010) presented the Spitzer imaging of 30 GRB hosts and measured their dust-uncorrected SFRs to be in a range of $0.01 - 10 M_{\odot}\,yr^{-1}$, with relatively lower sSFRs compared to the previous findings. They proposed extinction by dust to be the cause of the inconsistency with former studies.

In a comprehensive study Graham and Fruchter (2013) compared the star formation rate distribution of a GRB host sample (containing 14 galaxies) with those of other star-forming galaxy populations. This included the host galaxies of Type IC and Type II SNe, and local star-forming galaxies (SDSS). Their results showed that the SFRs of GRB hosts are consistent with the SFR distribution of other star-forming galaxy populations.

An interesting work was carried out by Kelly et al. (2014) in order to study the SFR density in a sample of 15 GRB hosts at $z \lesssim 1.2$. They used the HST images of the hosts and measured the projected star formation densities of the sample and found them to be (on average more than an order of magnitude) higher than the local star-forming galaxies (see the upper panel in Fig. 1.3). They proposed the formation efficiency of young, bound star clusters as a plausible explanation for the association of GRBs with regions of higher star formation densities.

GRB host galaxies are star-forming galaxies, with somewhat higher specific star formation and star-formation rate densities compared to the general star-forming galaxy population with similar stellar masses.

1.2.2 Stellar mass

Initial stellar mass measurements for small samples of GRB host galaxies showed the lack of massive galaxies among GRB selected galaxies (e.g Chary et al., 2002; Castro Cerón et al., 2006). This was confirmed by studies of larger samples: Le Floc'h et al. (2003) presented the photometry of 19 GRB host galaxies and found them all to be sub-luminous compared to other star-forming galaxies at similar redshifts. Fruchter et al. (2006) presented the HST imaging of 42 GRB host galaxies and compared their photometric properties with those of a sample of CC SN hosts. The two galaxy populations were expected to share similar galaxy environments as both host massive stars (as the progenitors of the GRBs and CC SNe). But they found the two populations to be fundamentally different. 41 out of the 42 GRB hosts appeared to be faint irregular galaxies, while the host galaxies of the CC SNe were commonly bright spiral galaxies. They proposed this to be due to the different metal enrichment and chemical evolution of the two galaxy populations. Similar results were obtained by Svensson et al. (2010) who found the fraction of massive spirals to be 10% for GRB hosts against 50% for CC SN hosts. Savaglio et al. (2009b) measured the stellar masses of a large sample of GRB hosts (40 long duration GRBs) basing it on SED modelling and found the median stellar mass of GRB hosts to be $10^{9.3} M_{\odot}$, lower than that of field galaxies. Castro Cerón et al. (2010) found a consistent result (a median stellar mass of $10^{9.7} M_{\odot}$) using 30 GRB host galaxies.

All of the above mentioned works were focused on the host galaxies of GRBs localised using their optical afterglows. Detection of massive galaxies hosting dark GRBs (dust obscured GRBs) put a question mark on biases introduced by selection effects (Hashimoto et al., 2010; Hunt et al., 2011; Svensson et al., 2012). This was strengthened by systematic studies of dust-obscured GRB hosts which showed that most of them were massive and luminous galaxies (Krühler et al., 2011a; Rossi et al., 2012a; Perley et al., 2013a). However, dark GRBs appeared not to be the dominant

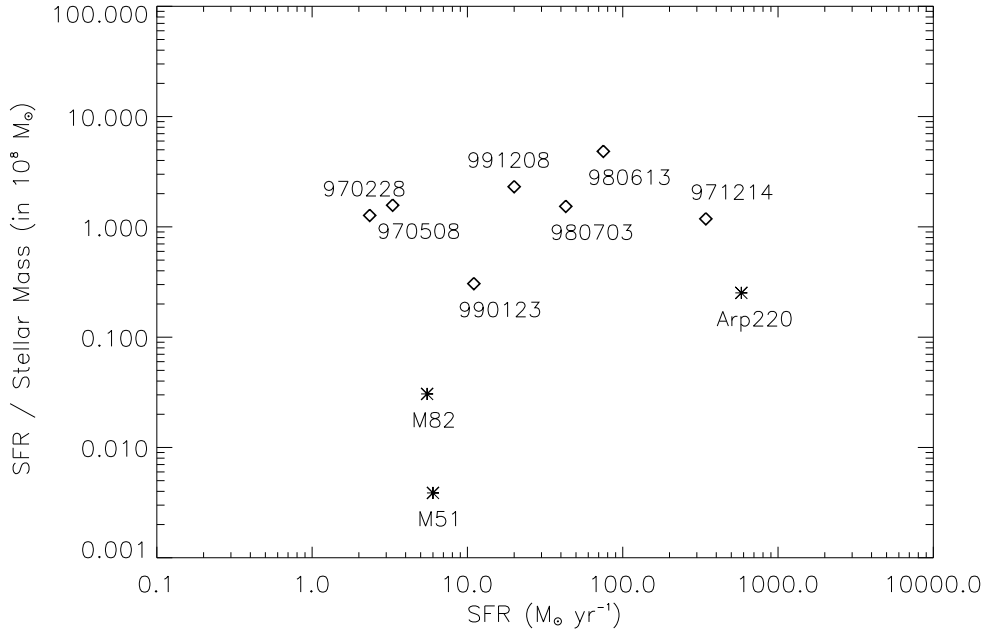

Figure 1.2: High sSFRs for seven GRB host galaxies (marked with diamonds) compared to nearby starburst galaxies (marked with asterisk), from Chary et al. (2002).

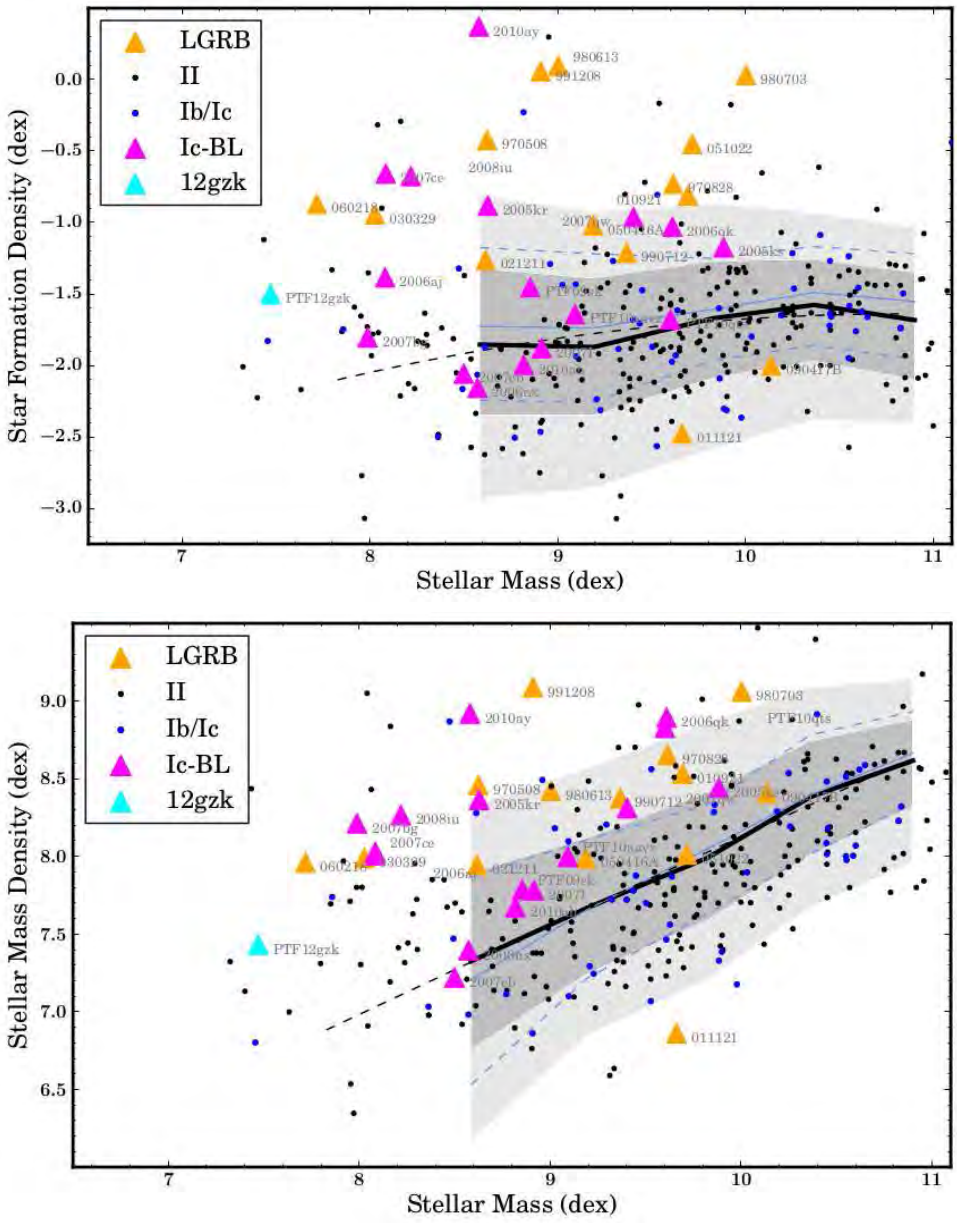

Figure 1.3: Star formation density (upper panel) and stellar mass density (lower panel) against host stellar mass for host galaxies of GRBs (marked as LGRB: long duration GRB) and CC SNe from Kelly et al. (2014). Dark gray region (68%), and light gray region (95%) show the distribution of SDSS star-forming galaxies. Host galaxies of GRBs show high star formation and stellar mass densities for their stellar masses.

population, and even after including them, the apparent deficiency of massive GRB hosts seemed to remain. This deficiency was proposed to be related to the nature of GRB host galaxy population (Greiner et al., 2011; Perley et al., 2013a).

Kelly et al. (2014) used the HST images of 15 GRB hosts at $z \sim< 1.2$ (including both optically luminous and dust-obscured GRBs) and measured the projected stellar mass densities of the sample. They found the GRB hosts to have high stellar mass densities for their stellar masses, on average more than an order of magnitude higher than the local star-forming galaxies (see the lower panel in Fig. 1.3).

In order to draw a robust picture, homogeneous GRB host samples were defined and similar studies were carried out for the uniformly defined samples with reduced selection biases. Such systematic studies was mainly possible after the launch of *Swift* in 2004 which stimulated GRB studies by detecting ~ 100 GRBs per year (see Gehrels et al., 2009, for a review on GRBs in the *Swift* era). The main large uniform samples so far are *BAT6* (Salvaterra et al., 2012), *TOUGH* (Hjorth et al., 2012b), and *SHOALS* (Perley et al., 2016a), containing 58, 69, and 119 GRB hosts respectively. The SED based stellar mass measurements of 14 $z < 1$ GRB hosts in *B*AT6 sample showed a population of faint low-mass star-forming galaxies (Vergani et al., 2015a). A bias towards low mass and metallicity was concluded for the *T*OUGH sample based on the luminoxity function of the hosts which are at $0 < z < 4.5$ (Schulze et al., 2015a). However, this was contradicted by Greiner et al. (2015) who found the luminosity function of GRB hosts in the redshift range of $3 < z < 5$ to be fully consistent with that of Lyman break galaxies. Finally, Perley et al. (2016e) compared the rest-frame near-infrared luminosities and stellar masses of *S*HOALS sample to those of the general population of star forming galaxies in the vast redshift range of $z \sim 0.3-6$ (Fig. 1.4). They found the $z < 1.5$ GRB hosts to be much fainter than the general star forming population, while $1.5 < z < 3$ hosts in their sample were slightly under-luminous with much more modest differences, and $z \sim> 3$ host were consistent with the general galaxy population (consistent with results of Greiner et al., 2015)).

GRB host galaxies at low redshifts appears to have lower stellar masses compared to the general population of star-forming galaxies, while at higher redshifts ($z \gtrsim 3$) they follow the luminosity function of the general galaxy population.

1.2.3 Metallicity

The single star collapsar model for GRB production requires the progenitor massive star to have low metallicity. This is needed in order to avoid mass loss through stellar winds and to conserve the angular momentum of the progenitor (see section 1.1.2). Such a model suggests that the environment in which GRB progenitors form need to be metal poor, and is supported by the observed low luminosities and stellar masses of GRB hosts. However, it should be kept in mind that the chemical abundance of the progenitor stars may not be a good measure of the mean metallicities in GRB environments as shown through simulation by Nuza et al. (2007).

Quantifying the metal content of the close environment of GRBs is needed in order to observationally confirm whether low metallicity conditions are required for the formation of GRBs. This is possible in a very few cases of nearby GRBs where the distance to the host allows detail observations and studies of the GRB environment as well as comparison to the other regions of the host galaxy (GRBs 980425 at $z = 0.0087$, 060505 at $z = 0.09$, and 080517 at $z = 0.09$ are the best

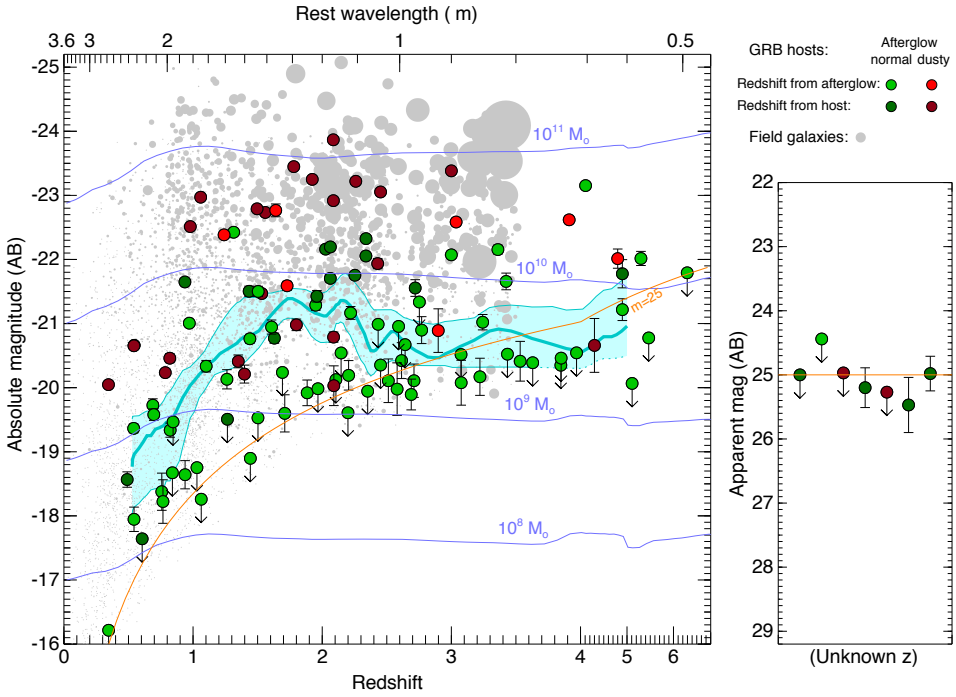

Figure 1.4: NIR absolute magnitudes of a uniform sample of 119 GRB host galaxies of SHOALS sample from Perley et al. (2016e). Green points indicate bursts not known to be obscured; red points indicate dust-obscured and "dark" bursts. Darker shades of both colors indicate redshifts measured from late-time host galaxy observations, while redshifts of lighter-shaded points are measured from target-of-opportunity afterglow observations. Field galaxies are plotted in gray with area scaled according to SFR.

candidates). But in almost all cases the overall metallicity content of host galaxies have been used as a measure of metal enrichment in GRBs environments. This is not unfair since in small galaxies metallicity is not expected to vary much in different regions of the galaxy (see Hidalgo-Gámez et al., 2001, and references therein), (also see Graham and Fruchter, 2013, for comparing the metallicities of GRB hosts with those in GRB sites).

Metal enrichment of gas in GRB host galaxies has been quantified using both absorption and emission methods. In emission, ratios of strong emission lines (like the ratio of Oxygen from OII or OIII lines to Hydrogen obtained from Hα or Hβ lines) are used to derive an Oxygen abundance 12+log(O/H) as a measure of the metal content of the ionised gas. This mainly measures the metallicity of the HII regions of the galaxy as the flux of the nebular emission lines are usually dominated by emission from these regions. These methods require certain calibrations for strong-line diagnostics which are typically based on physical conditions in low-redshift galaxies. This needs to be kept in mind while dealing with emission metallicity measurements at high redshifts ($z \gtrsim 2$, for detailed discussions see Maiolino et al., 2008; Steidel et al., 2014).

In absorption the ratio of the column densities of metals to that of neutral Hydrogen provides a direct and accurate metallicity measurement of the neutral gas in the host. Unlike in emission, absorption metallicities do not suffer from calibration uncertainties and therefore are more reliable measurements of galaxy metal enrichment, specially at high redshifts. Moreover, the absorption features can be detected up to the highest redshifts regardless of the host brightness. This makes it possible to obtain accurate metallicity measurements for the high redshift hosts for which emission lines are too faint to be detected.

Emission metallicities

The first few measurements of relative oxygen to Hydrogen abundances in GRB hosts (measured from nebular emission lines such as OIII and Hβ) revealed sub-solar metallicities (see Vreeswijk et al., 2001b, for GRB 990712 ; Fynbo et al., 2000; Sollerman et al., 2005, for GRB 980425; Bersier et al., 2006; Hammer et al., 2006, for GRB 020903; Prochaska et al., 2004; Sollerman et al., 2005, for GRB 031203:; Hjorth et al., 2003b; Gorosabel et al., 2005, for GRB 030329). Stanek et al. (2006) compared the oxygen abundances of 5 GRB hosts at $z \leq 0.25$ with that of the local star-forming galaxies and found the GRB hosts to have the lowest metallicities (Fig. 1.5). These 5 GRBs were all associated with SNe Ic and Modjaz et al. (2008) compared their hosts with galaxies hosting SNe Ic with no associated GRBs. They found the GRB hosts to have lower metallicities compared to the SN hosts, consistent with the findings of Fruchter et al. (2006) (based on mass-metallicity relation, see section 1.2.5) who found GRB hosts to be smaller galaxies compared to SN host galaxies (see section 1.2.2).

Such spectroscopic studies were extended to larger samples of GRB host galaxies. Savaglio et al. (2009b) performed metallicity measurements for 17 GRB host galaxies at $z \lesssim 1$ and found them relatively low, in the range 0.1 solar to solar with an average metallicity of 0.16 solar. Levesque et al. (2010a) studied 10 GRB host galaxies at $z < 1.0$ and found them to be significantly metal poor compared to the general galaxy population. Graham and Fruchter (2013) compared the metallicities of 14 $z < 1.0$ GRB hosts with those of general star-forming galaxies at similar redshifts. They found $\sim 75\%$ of GRB hosts to have $12 + \log(\mathrm{O/H}) < 8.6$, while only $\sim 10\%$ of star-forming galaxies had such low metallicities. This was when the metallicity distribution of their SN host sample was consistent with the metallicity distribution of the general galaxy population (see Fig. 1.6). Based on the difference between metallicity distributions of GRB hosts and local star-forming

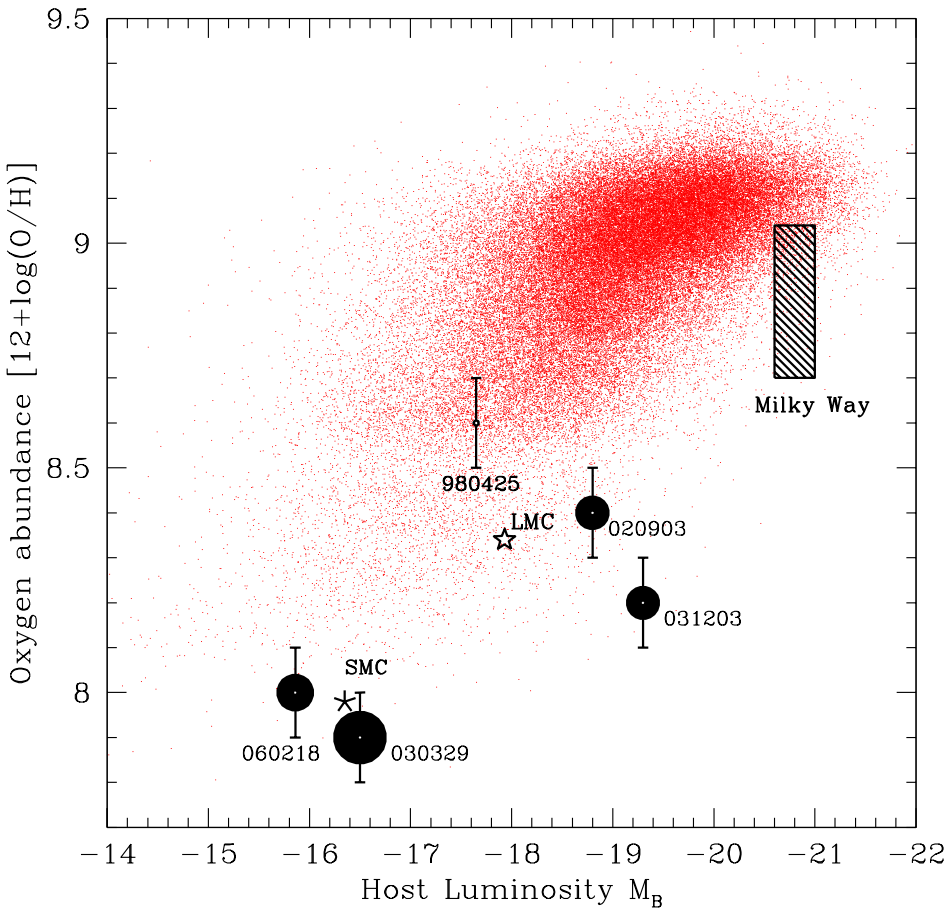

Figure 1.5: Oxygen abundance versus galaxy luminosity for Five low- z GRB/SN hosts (filled circles), local star forming galaxies (red small points), Milky Way, the LMC and the SMC from Stanek et al. (2006).

galaxies, they concluded the metallicity below half-solar to be a fundamental component of the evolutionary process that separates GRBs from the bulk of local star formation. Similar conclusions were obtained by Krühler et al. (2015) using metallicity measurements for 44 GRB host galaxies at $0.3 < z < 3.4$. They found the fraction of GRB hosts at $z < 1$ with super-solar metallicties to be $\sim 20\%$, a significantly less fraction compared to star-forming galaxies at similar redshifts.

The observed low metallicties for GRB hosts were consistent with earlier findings on GRB hosts' low stellar mass values. Several studies used the information on brightness/stellar mass of GRB hosts and proposed a metallicity threshold for the formation of GRBs, based on the scaling relations of the general star-forming galaxies (see section 1.2.5 for a detailed discussion on scaling relations for GRB hosts). With photometric information of 16 GRB hosts and assuming that GRB hosts follow the luminosity-metallicity relation of star-forming galaxies, Wolf and Podsiadlowski (2007) concluded solar-metallicity to be more or less the metallicity cut-off for GRB selected galaxies. They ruled out the requirement of metallicity cutoffs well below one-half the solar abundance as this would have needed GRB hosts to be much less luminous than the observed hosts in the sample of Fruchter et al. (2006). Kocevski et al. (2009) used the MZ relation and with assuming a metallicity threshold for GRB host galaxies estimated an upper limit on the stellar mass as a function of redshift. They compared their model stellar mass with the available measurements from Savaglio et al. (2009b) and Castro Cerón et al. (2010) and found a significant fraction of observed host galaxies with larger stellar masses than their upper limits. So they ruled out the metallicity cut-offs below 0.5-solar and instead proposed a solar metallicity cut-off.

Such studies were also carried out using the uniformly defined sample (see section 1.2.2). Vergani et al. (2015a) compared the distribution of the stellar masses of the *BAT6* sample with the results of simulated GRB host galaxies with applied metallicity thresholds on the progenitor star and found the distribution to be well reproduced for a metallicity threshold of 0.3-0.5 solar. Perley et al. (2016e) used the luminosity distribution of the 110 *SHOALS* GRB host sample in several redshift bins to check whether the increase of stellar mass with redshift is a product of a metallicity threshold for the GRB hosts. They used the redshift-dependent MZ relation and found their observations to be consistent with a redshift-invariant metallicity threshold of about solar metallicity.

While the value of the metallicity cut-off for GRB hosts is still under debate, reported solar and super-solar metallicities for several GRB host galaxies question the existence of a strict metallicity threshold for GRB formation (GRB 020819B at z=0.41 by Levesque et al., 2010c ; GRB 110918A at z=0.98 by Elliott et al., 2013a ; and several GRB hosts in the sample of Krühler et al., 2015, with metallicities up to $12 + \log(\mathrm{O/H}) = 9.0$).

A very interesting study was done by Nuza et al. (2007) by simulating the host galaxies of GRBs using two different models for the progenitor stars. The first model required the progenitor star to be only a massive one, which yielded a host population with similar properties to general galaxy population. Their second model required an additional condition on the metallicity of the progenitor in a way that only massive stars with metallicities lower than 0.1-solar were taken as GRB progenitors. They found this model to produce host population with properties in general agreement with observed ones. According to this model, at $z < 1$ GRB hosts tend to be smaller (and hence less metal-enriched) than the general galaxy population, but with high star formation efficiencies. But at higher redshifts, where all galaxies have higher star formation efficiencies and larger low-metallicity gaseous reservoirs, the metallicity bias of GRB hosts disappears. Also, using this model their simulated host sample included some host galaxies with super-solar metallicities. A few years later, Campisi et al. (2011) carried out a N-body simulation to study the effects imposed by the presence of a metallicity threshold for the generation of GRBs on their host galaxies. They

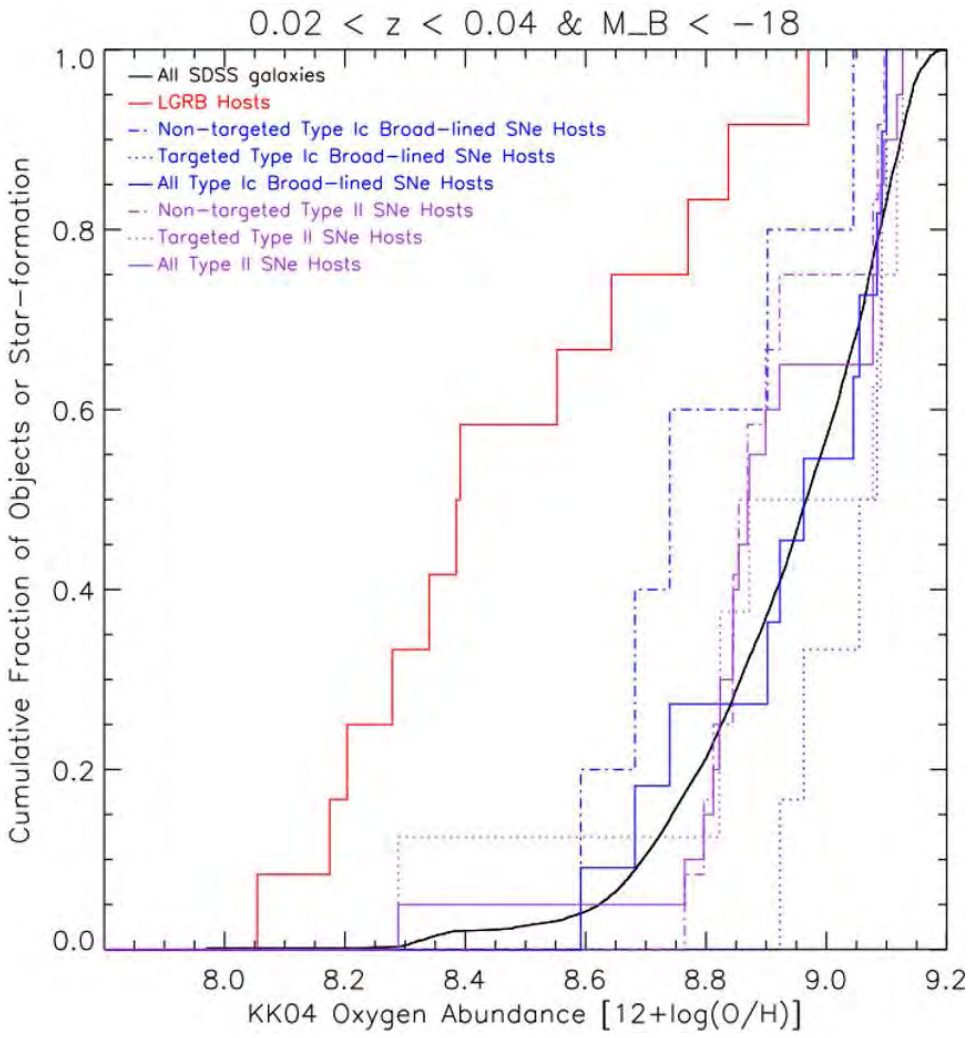

Figure 1.6: Cumulative fraction of population versus emission metallicity from Graham and Fruchter (2013). The magnitudes of both the host and SDSS samples are restricted to ensure that host magnitude does not bias the metallicity selection. The GRB hosts show considerably lower metallicities.

simulated three samples of star forming galaxies, one with no metallicity threshold and the other two with metallicity thresholds of 0.1 and 0.3 solar. They compared their simulated samples to 18 GRB host galaxies on mass-metallicity (1.2.5) and fundamental metallicity relations (see Fig. 1.7). They found that the sample with no metallicity threshold provides a very good match to the data and concluded that a threshold on metallicity is not necessary to reproduce the observed distribution of hosts' metallicities.

While the existence of a metallicity threshold for GRB formation is still under debate, GRB hosts appear to be generally metal poor galaxies.

Absorption metallicities

The presence of the GRBs' afterglows makes it possible to study GRB host galaxies through the absorption features that their interstellar media (ISM) imprint on the GRBs' spectra. Accurate measurements of Hydrogen and metal abundances allow accurate metallicity measurements for the GRB host galaxies up to very high redshifts (see Fig. 1.8 for the optical spectrum of a GRB at $z = 5.0$ with a clear Ly-α absorption profile).

The metallicity obtained from absorption profiles relative to the solar metallicity is defined as:

$$[\mathrm{X/H}] := \log \frac{\mathrm{N(X)}}{\mathrm{N(HI)}} - \log \frac{\mathrm{N(X)}_{\odot}}{\mathrm{N(HI)}_{\odot}}, \tag{1.1}$$

where X is a metal element (Zn, S etc.), and N(X) is the column density of the element X. Note that [X/H] measures the gas-phase metallicity as it is based on the column densities in gas-phase and it does not include the dust contribution. In order to have a reasonable estimate of metallicity one needs to choose the X element from those which are least depleted in dust. Zn, Si, and S are the commonly used elements as they are believed to have a very low fraction depleted into dust. Elements such as Fe, Ni, are the highly depleted elements and their abundances are usually used to study the dust content of GRB hosts. Another issue to consider while measuring the absorption metallicity is the ionization correction. This is to include the contribution of metals at high ionization levels (with small oscillator strengths) which are typically too weak to be detected in absorption. This contribution is negligible in systems where the dominant part of hydrogen is in a neutral phase. These systems, with HI column densities above a certain threshold, are selfshielded, have a negligible fraction of ionised hydrogen and with a negligible fraction of metals in high ionisation states.

Ly-α line with the rest frame wavelength of 1250 Åis the best profile to measure N(HI) . This line has a large oscillator strength and is usually highly saturated. However, at high column densities the damping wings of the Ly-α profile show up. This allows accurate N(HI) measurements which along with the negligible ionization correction allow accurate metallicity measurements. Such systems are known as Damped Lyman-α systems (DLAs) which are defined with $\mathrm{N(HI)} \gtrsim 2 \times 10^{20}\,\mathrm{cm}^{-2}$ (Wolfe et al., 2005).

GRB host galaxies do show very large column densities of Neutral Hydrogen as measured using their Ly-α absorption profiles (see section 1.2.4). But since GRBs fade away rapidly, optical afterglow spectroscopy is typically limited to ground-based telescopes for which (redshifted) Ly-α absorption line are only detectable at redshifts $\gtrsim 1.7$ due to atmospheric cut-off. Therefore, absorption metallicities are usually not measured for GRB hosts at $z \lesssim 1.7$. On the other hand, detection of

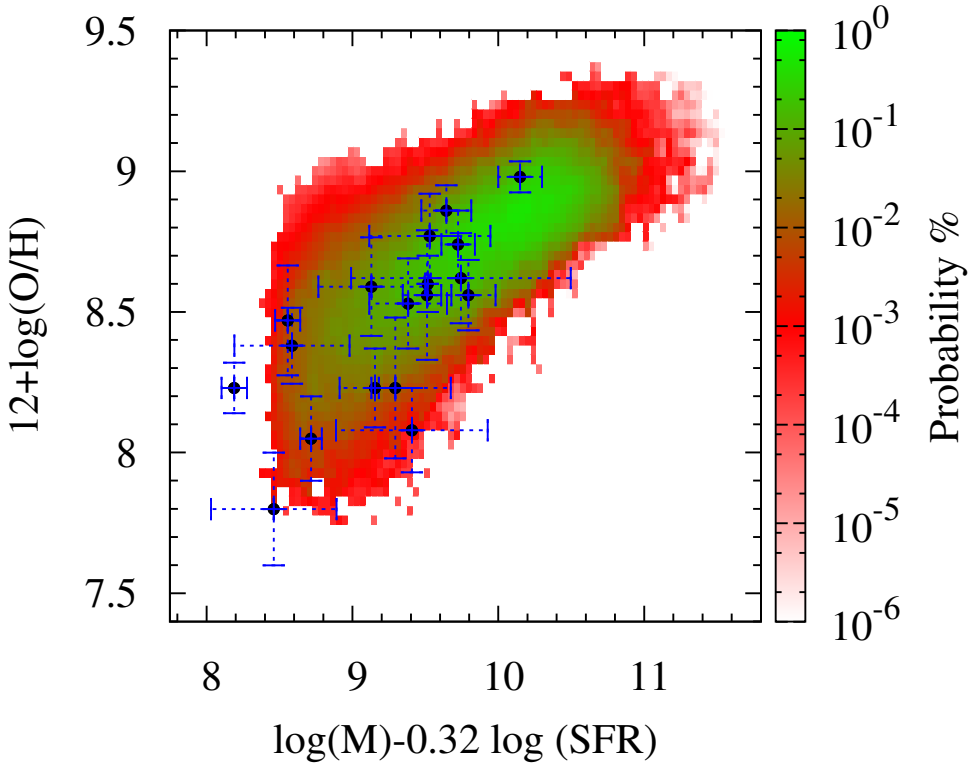

Figure 1.7: Simulated GRB hosts galaxies with no metallicity cut-off on the fundamental metallicity plane from Campisi et al. (2011). The colour-coded map show the probability of the simulated galaxies hosting a GRB and the blue points refer to the observed GRB hosts.

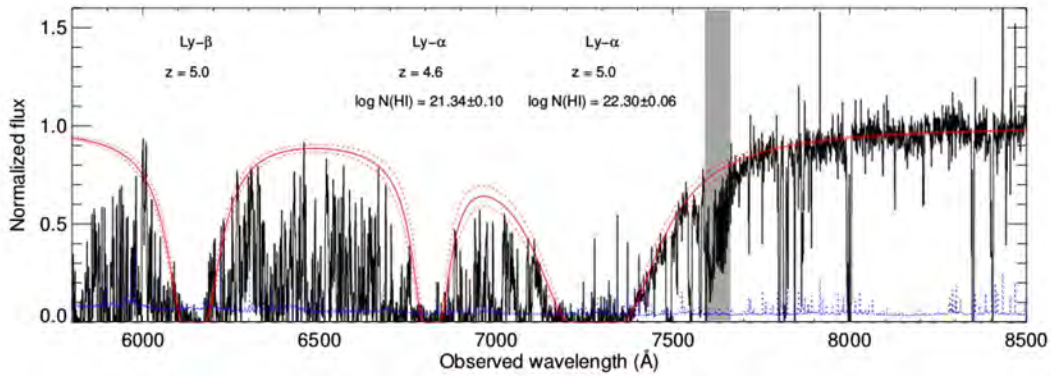

Figure 1.8: Optical spectrum of a GRB at $z = 5.0$ from Sparre et al. (2014) with the strong Ly-α and Ly-β absorption lines from the GRB host. The metal absorption lines are detected on the red side of the spectrum. We also see a strong Lyman-α (Ly-α) absorption from an intervening galaxy at $z = 4.6$.

Ly-α and metal lines at very high redshifts have allowed measurements of absorption metallicties up to very high redshifts where emission lines are too faint to be detected and emission metallicities are impossible to measure (the highest redshift for a GRB host with measured absorption metallicity is so far $z = 5.9$, Hartoog et al., 2015). This makes GRBs possible tools to study the chemical-evolution of the Universe.

The first measurements of absorption metallicities for GRB host galaxies showed sub-solar values : [Zn/H] = -0.25 for GRB 000926 at $z = 2.04$ Castro et al. (2003), [S/H] = -1.26 ± 0.2 for GRB 030323 at $z = 3.37$ by Vreeswijk et al. (2004), [S/H] = -2.0 ± 0.1 for GRB 050730 at $z = 3.97$ by Chen et al. (2005), [Zn/H] = -1.0 ± 0.4 for GRB 050401 at $z = 2.90$ by Watson et al. (2006) (see Savaglio, 2006, for more examples). A sub-solar metallicity value was the case for all further measurements, except for the host of GRB 090323 at $z = 3.58$ with a super-solar metallicity of $[\mathrm{X/H}] = 0.25$, reported by Savaglio et al. (2012).

Berger et al. (2006) compared the absorption metallicities of 6 GRB-DLA systems to those of the intervening DLAs in the sightlines of quasars (QSO-DLAs). They found GRB-DLAs to follow the trend of increased metallicity with lower redshift same as QSO-DLAs reported by Prochaska et al. (2003b). They also found the metallicity of GRB-DLAs to be systematically higher compared to QSO-DLAs. Fynbo et al. (2006) used a sample of 9 GRB-DLAs and compared them with the QSO-DLAs as well as local gas-rich galaxies. They found GRBs to have larger metallicities than the other two populations, and argued this do be a result of the metallicity gradients considering the smaller impact parameters in GRB hosts (see also Vreeswijk et al., 2004; Berger et al., 2006). They concluded that GRB hosts at $z > 2$ do not differ from typical star forming galaxies in metal-enrichment and suggested to use GRBs as complementary probes of chemical evolution at high redshifts. Similar studies were carried out using larger samples and hence with better statistics (see Savaglio, 2006; Savaglio et al., 2009b; Fynbo et al., 2009; Thöne et al., 2013; Cucchiara et al., 2015; Perley et al., 2016c). All these studies showed that GRB-DLAs tend to be (on average several times) more metal-rich than QSO-DLAs and to have a flatter redshift evolution (see Fig. 1.9). Hydrodynamic numerical studies of DLA systems carried out by Pontzen et al. (2010) showed

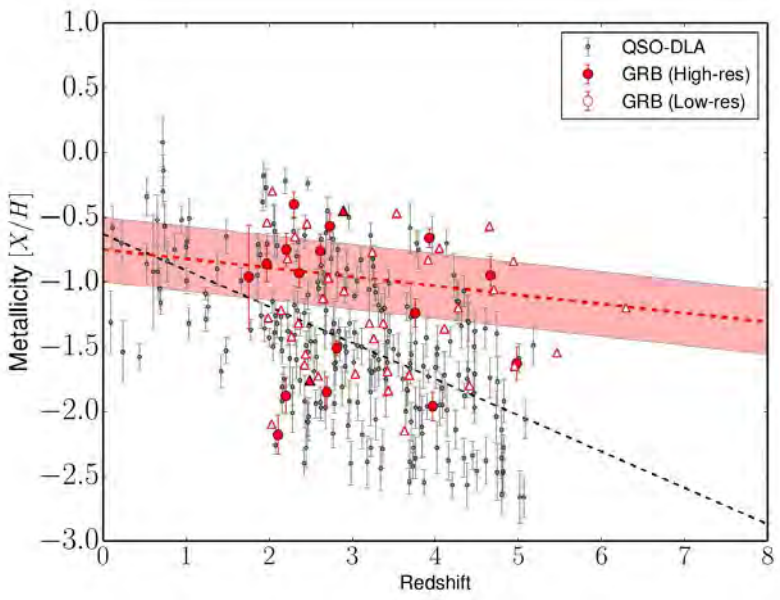

Figure 1.9: Metallicity evolution for GRB-DLAs (red) and QSO-DLAs (gray) from Cucchiara et al. (2015). Lower limits are indicated by upward triangles. A linear fit of the QSO-DLA metallicity is marked by the black dashed black line. The red dashed line and the shaded area represent the linear fit of the GRB-DLA data and the 1-σ error in the fitting parameters respectively.

similar results.

Absorption metallicity measurements for DLA systems intrinsic to GRB hosts reveal metal poor systems but with somewhat larger values compared to DLA systems in the sighlines of quasars.

1.2.4 Neutral Gas Content

Atomic gas

GRB host galaxies show very high column densities of neutral Hydrogen detected through Ly-α absorption line, mostly above $2 \times 10^{20}\,\mathrm{cm}^{-2}$ which is the DLA threshold. The first direct indication of a connection between GRB host galaxies and DLA systems was reported by Jensen et al. (2001) who measured a column density of $\mathrm{N(Hi)} = 21.2 \pm 0.5\,\mathrm{cm}^{-2}$ based on the Ly-α line in the spectrum of GRB 000301C at $z = 2.04$. This was followed by HI column densities of $21.3\,\mathrm{cm}^{-2}$ for GRB 000926 at $z = 2.04$ (Fynbo et al., 2001), $21.7 \pm 0.2\,\mathrm{cm}^{-2}$ for GRB 020124 at $z = 3.20$ (Hjorth et al., 2003a), $21.6 \pm 0.2\,\mathrm{cm}^{-2}$ for GRB 030429 at $z = 2.66$ (Jakobsson et al., 2004), and $21.90 \pm 0.07\,\mathrm{cm}^{-2}$ for GRB 030323 at $z = 3.37$ (Vreeswijk et al., 2004). Up to date more than 60 DLA systems intrinsic to GRB hosts have been detected in GRBs' spectra (Cucchiara et al., 2015, and

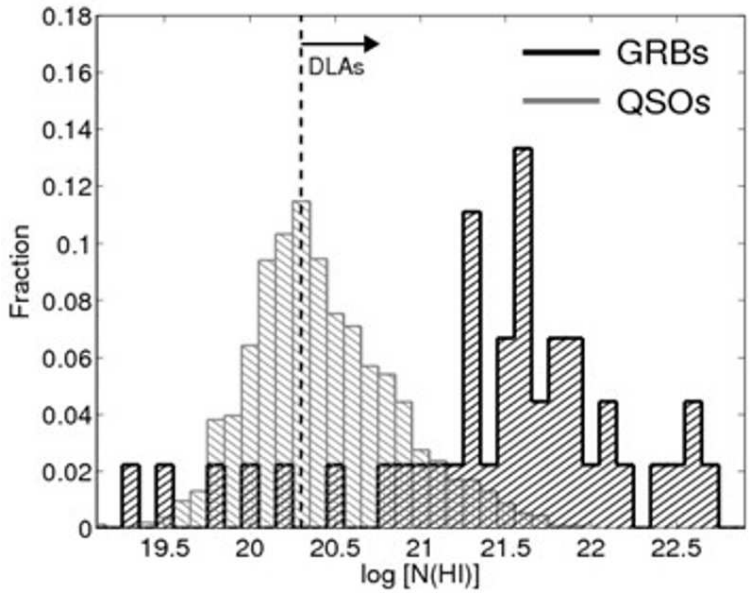

Figure 1.10: Normalized distribution of N(HI) in GRB-DLAa compared to the normalized N(HI) distribution of QSO-DLA, from http://slideplayer.com/slide/6856733/ by Edo Berger.

references therein). Given this, it is natural to compare the GRB host galaxies with the DLA systems in sightlines of quasars (see Fynbo et al., 2008; Prochaska et al., 2008).

Vreeswijk et al. (2004) compared the HI column density distribution of QSO-DLAs with that of 5 GRB-DLAs and found the GRB-DLAS to have columns amongst the highest values and presumed this to be due to GRBs probing star-forming regions with high density gas. Berger et al. (2006) extended the GRB sample to GRB hosts and compared them with 313 quasar intervening systems and found the GRB-DLAs to have higher column densities with about one-third exceeding the values measured in any QSO-DLA. Fynbo et al. (2009) carried out a similar study using 33 GRB hosts with measured N(HI) varying in a range between 10^{17} to $\sim 10^{23}\,\mathrm{cm}^{-2}$ and compared them to $\sim$ 1400 QSO-DLAs (Noterdaeme et al., 2009, sample). They found 80% of the hosts to have measured HI column densities above the DLA threshold. Besides the significant overlap between the QSO-DLA and GRB-DLA, they showed that the HI column densities of GRB-DLAs extend to significantly higher values than what was seen in the much larger QSO-DLA sample. They argued that the selection methods for the two DLA populations and the distance between the location of the GRB and the absorbing material were the two factors to cause the apparent higher N(HI) of GRB-DLAs (see Fig. 1.10 for a comparison between the N(HI) distributions of the two DLA populations).

The large Hydrogen column densities seen in GRB hosts could indicate the large content of neutral Hydrogen in the host galaxy, consistent with intense star forming activity and massive-star progenitor scenario. However, these absorption features only trace the gas along the narrow beam in the GRB sightline and carry little information on the whole galaxy. Understanding the nature of GRB host galaxies and conditions for GRB formation critically requires emission studies in the atomic and molecular gas. The detection of HI 21 cm emission from GRB host galaxies, followed

by mapping of the HI distribution, would allow one to estimate the total HI mass, the spatial distribution and the kinematics of the atomic gas, and the total dynamical mass by modelling the velocity field. Combining this information on the HI content with the information from optical and infrared wavelengths on star formation and the stellar mass would enable us to have a comprehensive picture of galaxies hosting GRBs and to compare them with the general population of galaxies (See Chapter 4 of this thesis).

GRB hosts usually show very high column densities of HI , on average about an order of magnitude larger than those of DLA systems in quasars sightlines. Though large N(HI) could point to large contents of neutral gas in these galaxies, 21 cm studies are required to measure the atomic gas content of these galaxies.

Molecular gas

As mentioned above, GRB host galaxies display the highest HI column densities of all absorbers measured through Ly-α absorption lines. Contrarily, molecular gas in absorption has been detected in the spectra of only four GRBs (Prochaska et al., 2009; Krühler et al., 2013; D'Elia et al., 2014; Friis et al., 2015a). Dissociation by GRB afterglow radiation was ruled out as the cause of molecular gas deficiency, considering the typical distances of the detected gas from the GRB location (a few hundred pc to a few kpc, see Ledoux et al., 2009). However, studies of QSO-DLAs show that the detection of molecular gas is not coupled to the high N(HI) , but rather to high metallicities and depletion factors, i.e., high dust content, which increases the formation rate of H_2 onto dust grains (Noterdaeme et al., 2008), consistent with the detection rate in GRB population (Ledoux et al., 2009; Krühler et al., 2013). Moreover, one should note that the detectability of H_2 lines in absorption requires high spectral resolution and S/N which is hard to achieve in GRB spectra given the short time in which the optical afterglows fade away (as short as a few hours).

The first attempts at CO emission line studies of GRB hosts, targeting four systems, yielded non-detections. (see Stanway et al., 2015, and references therein). But recently detection of CO emission has been achieved by ALMA for two GRB hosts with high metallicities at $z = 0.41$, and $z = 0.81$ (Hatsukade et al., 2014), and by IRAM for a nearby host with high dust content at $z = 0.89$ (Stanway et al., 2015). The three galaxies fall on the average $M(\mathrm{H_2}) - M_*$ relation of the general population of local star-forming galaxies (see upper panel of Fig 1.11). However, all three curiously show short timescales for gas consumption ($M(\mathrm{H_2})/\mathrm{SFR}$) for their stellar masses compared to the star-forming galaxies in the local Universe, but consistent with their high SFRs (lower panel of Fig. 1.11, see Stanway et al., 2015, for a detailed discussion). This means that the three GRBs occurred in a short-lived star formation episode that is not sufficient to produce the stellar masses of their hosts. If applicable to the general GRB population, this would suggest that GRBs form towards the end of star formation episodes in a galaxy. This is puzzling, since the most massive stars are expected to form in the early stages of such star-formation episodes. Extending such molecular gas studies to a larger GRB sample is of much interest, to test whether this pattern is typical of GRB hosts.

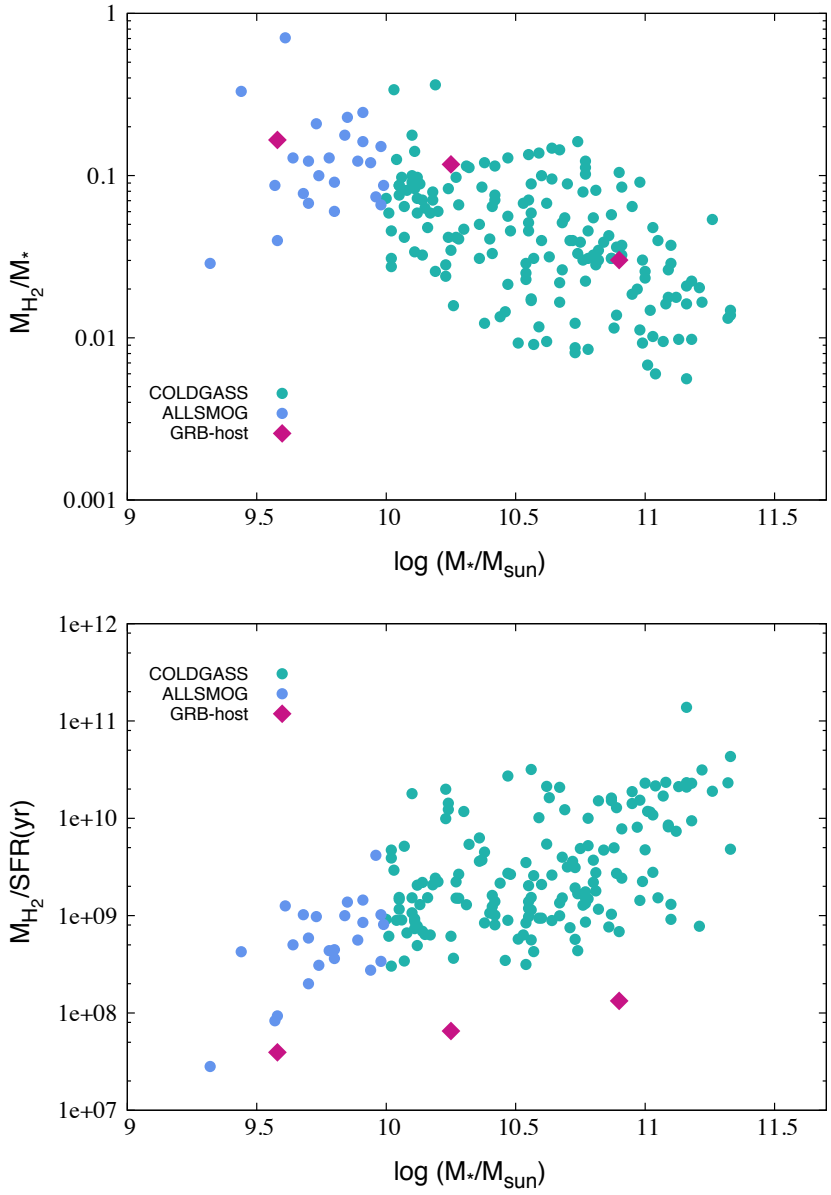

Figure 1.11: *Upper panel:* The three GRB hosts with detected CO in emission shown on the $M(H_2) - M_*$ relation for local star-forming galaxies (see Bothwell et al., 2014; Saintonge et al., 2011, for ALSMOG and COLDGASS surveys respectively). *Lower panel:* Gas consumption time scale for local star-forming galaxies and the GRB host galaxies with detected CO emission vs. stellar mass. Based on this small sample, it seems that the GRB hosts have short time scales for their stellar masses.

The few GRB hosts galaxies with measured molecular gas content (through CO emission lines) appears to have short timescales for gas consumption. Investigating the molecular gas contenet for a larger sample of GRB selected galaxies is required to see whether this is a general behaviour for this galaxy population.

1.2.5 Scaling relations

The low mass and metallicity of GRB host galaxies is expected to put them on the lower mass end of the mass-metallicity (MZ) relation of star-forming galaxies (e.g. Tremonti et al., 2004), but still on the MZ relation (of course within the scatter). However several studies have found the GRB hosts to be placed below the MZ relation, towards the lower metallicities. This means that GRB hosts are a distinct population from the general population of star-forming galaxies. This is contradictory though to the findings of several studies where GRB hosts were shown to obey the MZ relation of the general star-forming galaxy population. This has remained an issue under debate over the last decade.

Mass-metallicity relation for GRB host galaxies was first investigated by Savaglio et al. (2006) for 7 GRB host galaxies. The 7 hosts with redshifts varying from $z = 0.4$ to $z = 1$ were consistent with the MZ relation of the general star-forming galaxies at similar redshifts, though six of them were below the main relation towards the low metallicities. Stanek et al. (2006) studies the luminosity-metallicity relation for 5 nearby GRB host galaxies ($z \lesssim 0.25$) and compared them with local star-forming galaxies. They concluded that local GRB hosts strongly prefer metal-poor and therefore low-luminosity galaxies. Kewley et al. (2007) performed a similar study and also found the GRB hosts to be offset from the MZ relation towards lower metallicities. Meanwhile, Nuza et al. (2007) claimed that GRBs pick galaxies that trace the general MZ relation at all redshifts through performing a cosmological hydrodynamical simulations to generate GRB events and investigating the properties of GRB-selected galaxies in their simulations.

Savaglio et al. (2009b) found no MZ relation to hold for a sample of 9 GRB host galaxies. However, they did not find any indication that GRB hosts have metallicities lower than expected for their stellar masses. A year later, Levesque et al. (2010b) used a sample of 13 $z < 1.0$ GRB hosts and concluded that GRBs occur in host galaxies with lower metallicities than the general population for their stellar masses, with an average offset of ~ -0.4 from the MZ relation of star-forming galaxies at similar redshifts.

Mannucci et al. (2011) extended the GRB sample to 18 hosts. They too found GRB hosts to have a systematic offset with respect to the MZ relation. However, they considered the star formation properties of the hosts in their study and found the GRB hosts to be fully consistent with the fundamental metallicity relation (Mannucci et al., 2010). They concluded that the apparent low metallicity of GRB hosts is a consequence of the higher than average SFRs of GRB host galaxies. But Graham and Fruchter (2013) contradicted this by comparing the metallicity and SFR distributions of GRB hosts with those of the general star-forming galaxy population (Fig. 1.12). They concluded that the low-metallicity preference of GRB hosts is not primarily driven by the anti-correlation between star formation and metallicity, but is overwhelmingly due to the astrophysics of the GRBs themselves.

The connection between star formation rate and other properties of GRB hosts was earlier discussed by Savaglio et al. (2009b). They suspected the existence of a correlation between SFR and stellar mass for GRB hosts. Consistent with this, together with the MZ relation, Krühler et al. (2015) found a correlation between SFR and metallicity in different redshift bands for a large GRB host

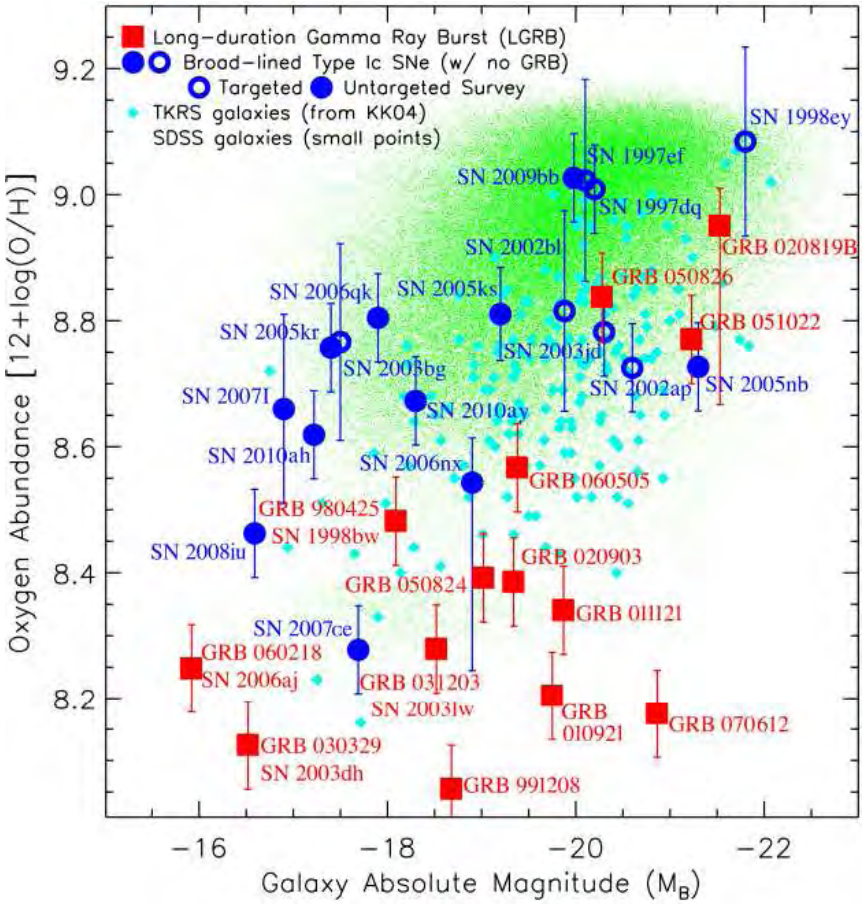

Figure 1.12: Metallicity versus absolute B-band galaxy luminosity of GRB (squares) and broad-lined Type Ic SNe hosts (circles) from Graham and Fruchter (2013). Star-forming galaxies from the SDSS (small dots) and TKRS (diamonds) are plotted in the background to provide a low and high redshift comparison sample, respectively. The profound difference between the GRB metallicity values and those of the Type Ic-bl SNe can be clearly seen in this plot.

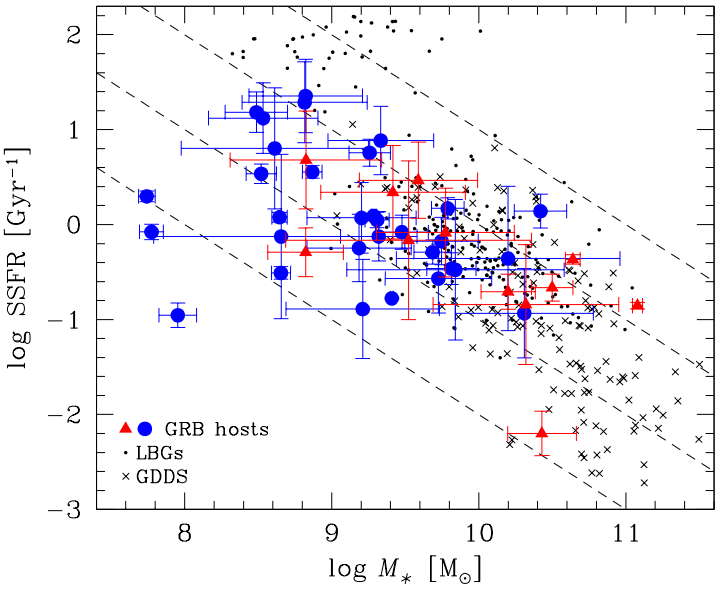

Figure 1.13: sSFR as a function of stellar mass from Savaglio et al. (2009b). The filled circles and triangles are GRB hosts, while crosses are star-forming GDDS galaxies and dots are LBGs.

sample. Savaglio et al. (2009b) also showed that GRB hosts follow an anti-correlation between sSFR and stellar mass similar to that seen for star-forming galaxies, but with lower masses and higher sSFRs compared to star-forming galaxies at similar redshifts (Fig 1.13). Though, for a fixed sSFR, GRB hosts appeared to have stellar masses several times smaller than Lyman break galaxies. Later works confirmed these findings (Svensson et al., 2010; Castro Cerón et al., 2010). Another scaling relation discussed for GRB hosts is the magnitude-size relation. Fruchter et al. (2006) and Svensson et al. (2010) investigated this relation for GRB hosts and compared it to that of galaxies hosting core collapse SNe. Both studies found the two populations to follow the same relation with GRB hosts falling on the lower mass end of the relation.

The consistency of GRB host galaxies with the MZ relation of the general star-forming galaxy population is a subject under debate. Nevertheles, it is important to appreciate that the low metal contents of GRB hosts differ from them being below the MZ relation of the general galaxy population.

1.3 A bigger picture

1.3.1 GRBs and Cosmic History

GRBs are beacons of star-forming galaxies up to very high redshifts. Their precise positions obtained from their afterglows allow follow up observations for detection of their host galaxies after

they fade away. The detectability of GRBs is unrelated to the brightness of their hosts and hence they provide complementary probes of the early Universe to emission-selected galaxy surveys. Also, accurate metallicity measurements of GRB hosts in absorption up to very high redshifts ($z \sim 6.0$ Hartoog et al., 2015) makes GRBs possible tools to study the chemical evolution of the universe (see section 1.2.3).

Tanvir et al. (2012) carried out follow up HST observations to image 6 GRB hosts lying at $5.0 \lesssim z \lesssim 9.5$ in order to study the luminosity function of galaxies. Only one of the hosts was detected, but using the information obtained from their observations they put constraints on the galaxy luminosity function and its evolution with redshift. McGuire et al. (2016) carried out a similar study and detected 3 $z \sim 6$ GRB hosts.

The star formation history of the Universe is another aspect which could be traced by GRBs up to very high redshifts. Since GRBs trace star-forming galaxies, the GRB rate is expected to trace the redshift-dependent star formation rate density. Several studies have been carried out to investigate the consistency of the GRB rate with the SFR history derived by traditional galaxy survey methods (e.g. Elliott et al., 2012; Robertson and Ellis, 2012; Lien et al., 2014; Yu et al., 2015). Many of these found the GRB rate to differ from that of SFR, with GRB rate underestimating the SFR in low redshifts and over-estimating it at high redshifts. However, applying the required conditions for GRB formation (such as metallicity thresholds, mass range boundaries etc.) appeared to take care of the inconsistency. In the most recent study Perley et al. (2016e) investigated the star formation efficiency of GRB hosts galaxies (using the SHOALS sample) by comparing their luminosities to the general population of star-forming galaxies. They used their findings to correct the GRB rate and found it to be quite consistent with the SFR history obtained from other galaxy surveys (Fig 1.14).

1.3.2 GRBs and Reionisation epoch

The nature of reionisation epoch is one of the central topics of research in cosmology today. This is believed to have taken place at a redshift ranging between $z \sim 6$ to $z \sim 20$, and possibly by the light of first stars and galaxies in the universe. While detection of Gunn-Peterson (GP) troughs in the spectra of quasars at $z \sim 6$ indicates the reionisation of the IGM, the cosmic microwave background observations suggests a redshift of $z \sim 9-10$ for the reionisation epoch. Therefore, measuring the neutral fraction of IGM ($x_{HI} = n_{HI}/nH$) at high redshifts is crucial to reveal the reionisation history.

Lyman-α emitters (LAEs) and Lyman-break galaxies (LBGs), the two possible probes of reionisation, suffer from uncertainties introduced by selection biases or lack of understanding of their natures. On the other hand, the spectral shape of the damped wings of the GP troughs in the spectra of $z \gtrsim 6$ quasars provide constraints on the neutral fraction of the IGM. However, the ionisation of the surrounding medium due to the strong ionising radiation of the quasar itself plus the poor understanding of the quasar spectral shape put question marks on the measured values of x_{HI}. This is where GRBs provide a possibility to probe the cosmic reionisation with advantages compared to LAEs, LBGs, and quasars (see Totani, 2012; Cucchiara et al., 2016). The intrinsic shape of GRB spectra has a much simpler shape (power law) compared to the spectra of quasars or LAEs and LBGs, which makes the fitting analysis to the damping wings of the GP troughs in the spectra more precise and decrease the model uncertainties. Also, GRB spectra are much brighter than LAEs and LBGs, and sometimes even brighter than quasar spectra, if observed quickly after the burst. Moreover, unlike in the case of quasars, the IGM ionisation state of the surrounding regions of GRBs is expected not to had been effected by the ionising flux of the GRB.

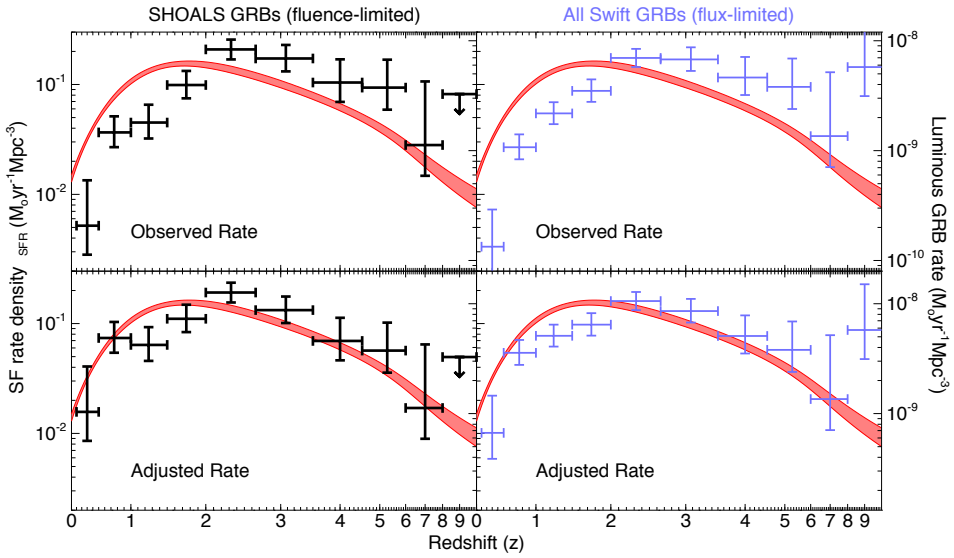

Figure 1.14: Cosmic rate density of GRBs compared to that of star formation from Perley et al. (2016e). The top panels show the raw, uncorrected GRB rate. An “excess" in the GRB rate relative to the galaxy-inferred SFR density is seen at high-z. The bottom panels show the corrected rates based on the observed tendency for GRBs to avoid luminous galaxies at low-z. Applying this correction produces good consistency in the respective rates (see Perley et al., 2016e, for details).

The possibility of studying the IGM and reionisation epoch using high-redshift GRBs has been investigated in a few cases. Totani et al. (2006) carried out such study using the spectrum of GRB 050904 at $z = 6.30$. Similar studies were performed for GRB 130606A at $z = 5.91$ by Totani et al. (2014); Hartoog et al. (2015); Totani et al. (2016).

1.4 What can be learnt from gas kinematics

Kinematic characteristics provide powerful tests for scenarios of galaxy formation. In this section I briefly discuss the information obtained through gas kinematics in the field of galaxy formation and evolution, using both absorption and emission methods.

1.4.1 Gas Kinematics in Emission

In the standard picture of galaxy formation, halos of dark matter set the stage for galaxy formation. This non-baryonic component of a galaxy dominates the dynamics of the galaxy. This picture is most supported by 'flat rotation curves' observed in nearby spiral galaxies (Rubin and Ford, 1970; Roberts and Rots, 1973; Rubin et al., 1978). To paint a general picture, the rotation curve rises steeply in the innermost few kpc of a galaxy, and then flattens (with a turnover and a minor slow decline in more massive galaxies Persic et al., 1996; Sofue and Rubin, 2001). The rotation velocity stays high beyond the outer edge of the optical disc which points to the presence of dark matter halos (if light traced mass the velocity would drop off sharply instead of flattening). This can be traced best through the HI gas, specially since its radial extent is often (a few times) larger than that of the visible disk

The neutral hydrogen in galaxies can be studied through the HI 21 cm emission line. This line is a powerful tool to obtain information on galaxy kinematics. The width of this line gives a rough estimate of the rotational velocity in a galaxy. Tully and Fisher (1977) reported a correlation between the HI line width and the optical luminosity for nearby disk galaxies, known as Tully-Fisher (TF) relation. Mapping the HI 21 cm from galaxies with interferometers improved constraining the rotational velocity and provided valuable information on the distribution and kinematics of gas in detail and with high velocity and spatial resolutions. This included the best evidence of cold gas accretion as the fuel of active star formation which plays a fundamental role in galaxy evolution.

In addition to providing a direct measure of the accreting gas, HI 21 cm observations are powerful tracer of merger events and can be used for modeling and estimating timescales in interacting systems. Peculiar and disturbed HI structures and kinematics point at ongoing or recent processes of accretion. In some cases multiple systems with similar masses are found to be associated with long tails or bridges which indicate the ongoing tidal interactions and major mergers. Disturbed structure and kinematics (specially in outer regions) in galaxies with small companions or in some cases with no visible companion also have been considered as minor mergers or gas infall (see Fig. 1.15 for an example). Peculiar structures and kinematics seen through HI observations appears not to be rare in the nearby universe. HI studies of a large sample of galaxies (300, spirals and irregulars) have shown that at least 25% of them have signatures of some kind of interaction, ongoing or past (see Sancisi et al., 2008, for a review on peculiar structures and kinematics through HI observations).

The sensitivity of today's radio telescopes limits HI 21 cm emission studies to relatively low redshift for individual galaxies (typically $z \lesssim 0.2$, though see Fernández et al., 2016, for detection of HI 21 cm emission from a galaxy with a high gas mass at $z \sim 0.38$, the single galaxy with

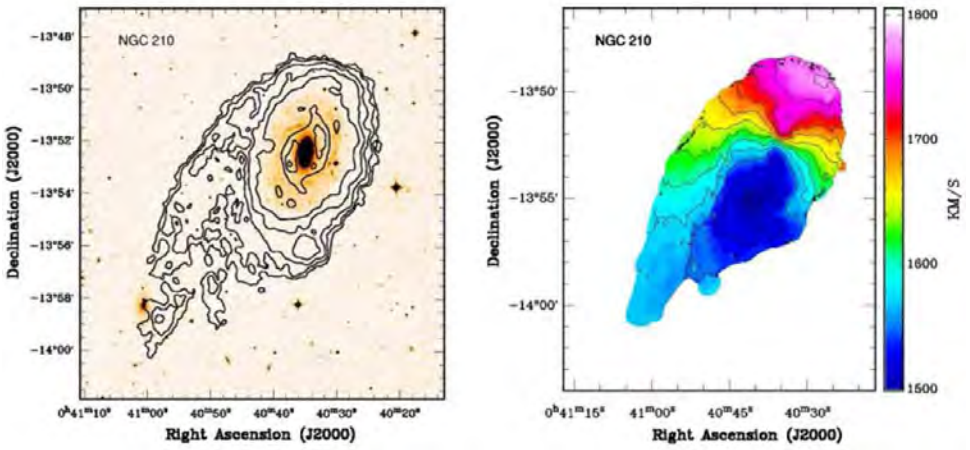

Figure 1.15: An example of a galaxy (NGC 210) showing signs of interactions/accretion from Sancisi et al. (2008). The left panel shows the HI density distribution superposed on the optical image and the right panel shows the velocity field of the galaxy.

detected HI 21 cm beyond $z \sim 0.2$; also see Lah et al., 2009, for reaching a redshift of $z \sim 0.37$ by stacking the signals of 324 galaxies). Bright emission lines from ionised gas (such as Hα) have hence been used instead to study the kinematics properties of galaxies at higher redshifts. Initial studies of galaxies at high redshifts showed that they had rotational curves similar to low redshifts ones (Vogt et al., 1996), revealing the existence of rotating disks at high redshifts. These high-z galaxies also appeared to follow the TF relationship with significantly increased scatter compared to the local relation. Also, the fraction of Galaxies with anomalous kinematics were found to be significant ($\gtrsim 25\%$) (Simard and Pritchet, 1998; Ziegler et al., 2002; Böhm et al., 2004).

Several surveys extended these studies to larger numbers of galaxies in redshift ranges from $z \sim 0.6$ up to $z \sim 3$ (see the excellent review by Glazebrook, 2013, for detailes). More importantly, resolved kinematic measurements through integral field Unit spectroscopy at high redshifts, and with high spatial resolutions, led to information which were missed in photometric studies. In numerous cases, galaxies that were morphologically irregular (as seen in photometric studies) were found to be kinematically regular. In fact, significant fractions of galaxies at high redshifts turned out to be rotating disks, though with high intrinsic velocity dispersions compared to local disk galaxies (Förster Schreiber et al., 2009; Law et al., 2007, 2009; Flores et al., 2006; Wright et al., 2007, 2009; Wisnioski et al., 2011). Such large intrinsic dispersions were argued to be due to high gas fractions, star formation feedback, cold gas accretion, and clumpiness (see Genzel et al., 2008, 2011; Swinbank et al., 2012a; Gnerucci et al., 2011).

Comparable fractions of high-z galaxies showed complex kinematic structures, such as galaxies with little evidence for systemic rotation but large intrinsic velocity dispersion (dispersion dominated systems, see Fig. 1.16), galaxies with disturbed rotating kinematics (due to minor mergers or infall/outflow), or systems with kinematic structures showing clear major mergers (Förster Schreiber et al., 2009; Law et al., 2007; Flores et al., 2006; Epinat et al., 2012; Gnerucci et al., 2011; Wisnioski et al., 2011; Swinbank et al., 2012b; Lemoine-Busserolle and Lamareille, 2010; Lemoine-Busserolle et al., 2010). As for the TF relation, it appeared that high-z galaxies follow it

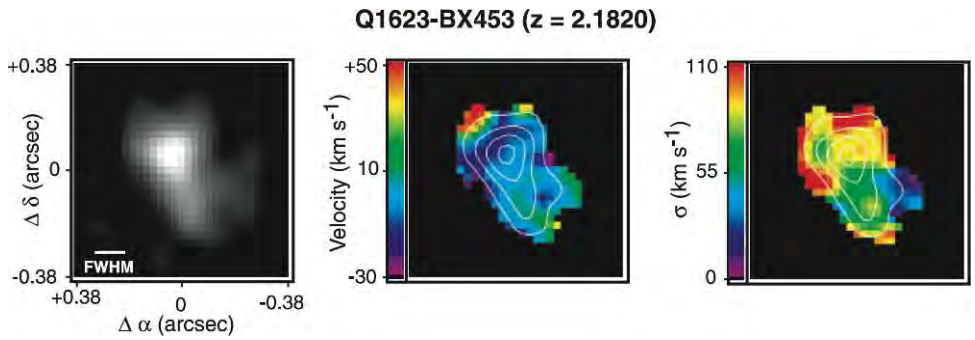

Figure 1.16: An example of a UV-selected dispersion-dominated galaxy at $z = 2.18$ from Glazebrook (2013). The three panels from left to right are Hα intensity, velocity, and dispersion.

or its modified version, the stellar-mass TF relation, with increased scatter about the mean relation due to the presence of non-rotators. The redshift evolution of the stellar mass TF relation is still under debate (see Glazebrook, 2013, and references therein).

1.4.2 Gas Kinematics in Absorption

Kinematic characteristics of gas in QSO-DLA systems have been used in order to explain the origin and structure of this high redshift galaxy population. The proposed scenarios include the thick-disk model in which DLAs are rotating galaxies similar to but thicker than the present-day disk population, and the protogalactic clump scenario where multiple clumps are bound to a virialized dark matter halo (see the review article by Wolfe et al., 2005, and references therein). The absorption profiles in DLA systems usually show several components or clouds tracing the velocity field in these high-z galaxies. Each of these components has a broadening of a few km s^{-1}, but the total velocity width of the system is much larger, varying from a few tens of km s^{-1} to several hundreds km s^{-1}.

The kinematics structure of high-ion profiles (like CIV and SiIV lines) are significantly different from those of the low-ion lines (Lu et al., 1996). The two sets of profiles have different velocity widths, with high-ion lines probing larger values of velocity spread. Also, the components (clouds) in low ion profiles are misaligned in velocity space from those in high-ion lines (Wolfe and Prochaska, 2000). However the centres of both profiles seem to be aligned (Wolfe and Prochaska, 2000; Prochaska et al., 2008).

Further insight into the nature of DLA systems was gained by relating their kinematics to their other properties. The existence of a correlation between metallicity and velocity width for these galaxies was first noted by Wolfe and Prochaska (1998), indicating that there is a relation between kinematics and mass in these high-z systems (see also Ledoux et al., 2006; Møller et al., 2013; Neeleman et al., 2013). Wolfe and Prochaska (1998) also found that DLAs with larger velocity widths had smaller column densities of HI. This was contradictory to the rotating disk and multiple clump models of DLAs. Similar studies were carried out by Prochaska et al. (2008) and Neeleman et al. (2013) who found no specific trend between N(HI) and the kinematics of DLA systems.

Sevaral high resolution simulations have been performed in order to investigate the nature of the DLA population (Pontzen et al., 2008 ; Tescari et al., 2009; Bird et al., 2015; see also Pontzen

et al., 2010, for simulations of GRB-DLAs). Although these studies have succeeded in matching the observed rate, column density distributions, and the relation between metallicity and velocity width for DLAs, they have failed to produce the observed kinematics of the absorption profiles. Specifically the number of high velocity width systems generated by these simulations are underestimated compared to observations.

The absorption features in the spectra of GRBs show similar kinematic properties. Prochaska et al. (2008) used a modest sample of GRB-DLAs and compared their kinematics to those of QSO-DLAs. They found that the distribution of the low-ion velocity widths were similar for both populations, with a median of ~ 80 km s^{-1}and a significant tail extending to velocity widths as large as several hundreds of km s^{-1}. They proposed this similarity to be due to comparable galaxy masses for both the populations.

1.5 This thesis

I present here a comprehensive study of the gas kinematics in GRB host galaxies, using both absorption and emission methods. The presence of GRBs' spectra makes it possible to study the hosts's properties in absorption, using the absorption features imprinted on GRBs' spectra by the host galaxies. Also, the short lifetime of GRBs provide the opportunity of follow up observations of host galaxies in emission after the bright GRBs fade away. The unique opportunity of obtaining information from both methods for this galaxy population and comparison between them provides the most complete picture for this galaxy population. I investigate the properties of gas in GRB host galaxies through a multi-wavelength study. I use optical and radio data from leading observational facilities in the world to study and compare the properties of different phases of gas, their interconnections, and their relation with other properties of GRB hosts. Moreover, I compare these findings to those of other galaxy populations in order to investigate if GRB-selected galaxy population is distinct from the general population of star-forming galaxies.

In chapter 2, I present a study of gas kinematics for GRB host galaxies at redshifts $z \gtrsim 2.0$ in absorption. Using optical data (mainly from Very Large Telescope, VLT) I investigate the correlation between the velocity width of the absorption profiles and the metallicity for a large sample of GRB-DLAs. I extend the absorption study of gas kinematics to lower redshifts (down to $z = 0.34$) in chapter 3. In this chapter I compare the properties of neutral gas (obtained from absorption) to those of the ionised gas (obtained from emission) using a large GRB sample. I investigate the relationships between gas kinematics, metallicity, and stellar mass, using both absorption and emission methods. Finally, I present the mass-metallicity relation for a large sample of GRB hosts and investigate whether it differs from the mass-metallicity relation of the general star-forming galaxy population. In chapter 4, I present the first mapping of the HI 21 cm emission line for a GRB-selected galaxy, the host of the closest known GRB (GRB 980425) at $z = 0.0087$. This allows studying the spatial distribution and the kinematics of the atomic gas simultaneously. Finally, I summarise the conclusions of the research done for this thesis in chapter 5 .

Chapter 2

Velocity-metallicty correlation for GRB hosts galaxies through absorption studies

This chapter containes the folllowing paper:
"On the velocity-metallicity relation of Damped Lyman-alpha systems intrinsic to GRB host galaxies"
Arabsalmani, Maryam; Moller, Palle; Fynbo, Johan; Christensen, Lise; Freudling, Wolfram; Savaglio, Sandra; Zafar, Tayyaba
2015, Monthly Notices of the Royal Astronomical Society, Volume 446, Issue 1, p.990-999

2.1 Abstract

We analyze a sample of 16 absorption systems intrinsic to long duration GRB host galaxies at $z \gtrsim 2$ for which the metallicities are known. We compare the relation between the metallicity and cold gas velocity width for this sample to that of the QSO-DLAs, and find complete agreement. We then compare the redshift evolution of the mass-metallicity relation of our sample to that of QSO-DLAs and find that also GRB hosts favour a late onset of this evolution, around a redshift of ≈ 2.6. We compute predicted stellar masses for the GRB host galaxies using the prescription determined from QSO-DLA samples and compare the measured stellar masses for the four hosts where stellar masses have been determined from SED fits. We find excellent agreement and conclude that, on basis of all available data and tests, long duration GRB-DLA hosts and intervening QSO-DLAs are consistent with being drawn from the same underlying population.

GRB host galaxies and QSO-DLAs are found to have different impact parameter distributions and we briefly discuss how this may affect statistical samples. The impact parameter distribution has two effects. First any metallicity gradient will shift the measured metallicity away from the metallicity in the centre of the galaxy, second the path of the sightline through different parts of the potential well of the dark matter halo will cause different velocity fields to be sampled. We report evidence suggesting that this second effect may have been detected.

2.2 Introduction

Stellar mass and metallicity are two of the most fundamental physical properties of galaxies. The metal enrichment of the inter stellar medium (ISM) of a galaxy is a consequence of supernova explosions and stellar winds and is therefore related to the star formation history (SFH) of the galaxy. Also, the amount of mass in stars is a function of galaxy SFH. Therefore, understanding the evolution of the two properties and the relation between them is fundamental to understand the formation and evolution of galaxies. Observations have shown that for local and low redshift galaxies a tight relation exists between the galaxy mass and its metallicity (see e.g. Dekel and Woo, 2003; Tremonti et al., 2004). The evolution of the mass-metallicity (MZ) relation has been studied using emission lines from HII regions in galaxies out to $z \gtrsim 3$ and reveal for a galaxy of a given stellar mass a trend of a decreasing metallicity with increasing redshift (Savaglio et al., 2005; Erb et al., 2006; Maiolino et al., 2008; Troncoso et al., 2014). Whether the numerous galaxies at the faint end of the luminosity function follow extrapolations of the MZ relation cannot easily be addressed using emission selected samples, and most studies have focused on composite spectra or a few individually selected massive galaxies (Erb et al., 2006; Henry et al., 2013; Cullen et al., 2014). Gravitational lensing which magnifies the flux of background sources is a powerful tool to probe the faint end of the galaxy luminosity function. Studies of low-mass gravitationally lensed galaxies hint at a weaker evolution of the MZ relation and an increasing scatter out to $z = 2$ (Richard et al., 2011; Wuyts et al., 2012; Christensen et al., 2012; Belli et al., 2013).

Alternative selection techniques to luminosity-limited galaxy samples allow us to form a complementary picture of the MZ evolution with cosmic time (the MzZ relation hereafter, following Christensen et al. (2014)). Long duration Gamma-ray burst (GRB) selected galaxies are preferentially blue, star-forming galaxies (e.g. Le Floc'h et al., 2003; Christensen et al., 2004) with low metallicities (e.g. Savaglio et al., 2009b; Graham and Fruchter, 2013). Earlier studies were biased towards GRBs with bright optical afterglows, and recent unbiased GRB samples (Hjorth et al., 2012b) have shown that the hosts follow the general trend of star-forming galaxies at similar redshifts (Michałowski et al., 2012). Damped Lyman-α (DLA) absorption line systems which arise in the GRB host galaxies can be observed out to very high redshifts (e.g. Sparre et al. (2014) analyse the DLA system at $z \sim 5$ in the GRB 111008A afterglow spectrum and Chornock et al. (2014) obtain metallicity contraints of GRB 140515A at $z = 6.33$) and their metallicity can be measured accurately from absorption lines which arise in the ISM. Since GRB afterglows are transients one can study the host galaxy properties later when the GRB afterglows have faded away. Therefore, GRBs are ideal systems to study the MZ relation and its evolution at high redshifts.

Conventional studies of DLA systems in quasi stellar object (QSO) spectra are used to probe a differently selected population of high redshift galaxies. Metallicities of intervening QSO-DLAs have been measured accurately for several hundred systems at redshifts out to $z = 5$ (Pettini et al., 1997; Ledoux et al., 2002; Prochaska et al., 2003a; Rafelski et al., 2012). However, due to the large difference in magnitudes between the bright background QSOs and the continuum emission from the much fainter foreground galaxies, these are extremely difficult to detect when the line of sight to the galaxy and QSO is very close. This prevents the direct measurement of the stellar masses for most DLA galaxies in the sightlines of QSOs, and prevents a direct comparative MZ study of this population. To date, only five QSO-DLA galaxies at $z > 2$ have measured stellar masses (Krogager et al., 2013b; Fynbo et al., 2013; Christensen et al., 2014).

While masses of the QSO-DLA galaxies are not known for the majority of the population, the velocity width of low-ionisation species of absorption lines can be used as a proxy for the mass.

Table 2.1: Sample of 20 GRB host DLA systems with their metallicities and selected low ion lines used for velocity width measurements. Metallicity measurements are based on element X. References for redshifts, *HI* column densities, metallicity measurements, and published low-ionization profiles are quoted in the table footnote.

GRB	redshift	$\log[N_{HI}/(cm^{-2})]$	$[X/H]$	X	selected line[a]	Instrument	Ref.[b]
000926	2.0379	21.3 ± 0.2	-0.13 ± 0.21	Zn	SiII 1808	Keck/ESI	(1),(2)
030323	3.3718	21.90 ± 0.07	-1.26 ± 0.20	S	SII 1253	UT4/FORS2	(3)
050401	2.8992	22.60 ± 0.30	-1.0 ± 0.4	Zn	SiII 1808	VLT/FORS2	(4)
050505	4.2748	22.05 ± 0.10	$-1.2\pm...$	S	SiII 1527	Keck/LRIS	(5)
050730	3.9686	22.10 ± 0.10	-2.18 ± 0.11	S	NiII 1370	VLT/UVES	(6)
050820A	2.6147	21.05 ± 0.10	-0.39 ± 0.10	Zn	NiII 1741[c]	VLT/UVES	(6),(7)
050922C	2.1992	21.4 ± 0.3	-1.82 ± 0.11	Si	FeII 1608	VLT/UVES	(6),(8)
060206	4.0480	20.85 ± 0.10	-0.84 ± 0.10	S	SII 1253	WHT/ISIS	(9)
060510B	4.941	21.3 ± 0.1	-0.85 ± 0.15	S	NiII 1317	Gemini/GMOS	(10)
070802	2.4549	21.50 ± 0.20	-0.50 ± 0.68	Zn	SiII 1808	VLT/FORS2	(11)
071031	2.6922	22.15 ± 0.05	-1.73 ± 0.05	Zn	NiII 1317[d]	VLT/UVES	(6),(7)
080210	2.641	21.90 ± 0.10	-1.21 ± 0.16	Si	SiII 1808	VLT/FORS2	(12)
081008	1.9683	21.11 ± 0.10	-0.52 ± 0.11	Zn	CrII 2056	VLT/UVES	(13)
090313	3.3736	21.28 ± 0.3[e]	-1.4 ± 0.3	Fe+0.3[f]	MgI 2852	VLT/Xshooter	(14),(15)
090323	3.5690	20.76 ± 0.08	0.25 ± 0.09	Zn	SiII1808	VLT/FORS2	(16)
090926A	2.1071	21.60 ± 0.07	-1.85 ± 0.10	S	FeII 2374	VLT/X-shooter	(17)
100219A	4.6672	21.14 ± 0.15	-1.1 ± 0.2	S	SII1 253	VLT/X-shooter	(14)
111008	5.0	22.30 ± 0.06	-1.70 ± 0.10	S	NiII 1370	VLT/X-shooter	(18)
120327A	2.8145	21.01 ± 0.09	-1.17 ± 0.11	Zn	CrII 2056	VLT/X-shooter	(19)
120815A	2.358	21.95 ± 0.10	-1.15 ± 0.12	Zn	MnII 2594	VLT/X-shooter	(20)

[a]Transition line used to determine the velocity width of low-ionization line profiles.
[b]References: (1) Castro et al. (2003); (2) Savaglio (2006); (3) Vreeswijk et al. (2004); (4) Watson et al. (2006); (5) Berger et al. (2006); (6) Ledoux et al. (2009) ; (7) This work; (8) Piranomonte et al. (2008); (9) Fynbo et al. (2006); (10) Price et al. (2007) ; (11) Elíasdóttir et al. (2009); (12) De Cia et al. (2011); (13) D'Elia et al. (2011); (14) Thöne et al. (2013) ; (15) de Ugarte Postigo et al. (2010); (16) Savaglio et al. (2012); (17) D'Elia et al. (2010); (18) Sparre et al. (2014) ; (19) D'Elia et al. (2014) ; (20) Krühler et al. (2013)
[c] ESO Science Achive, Program Id: 075.A-0385(A), Fynbo et al. (2009)
[d] ESO Science Achive, Program Id: 080.D-0526(A)
[e] J. X. Prochaska, private communication.
[f] Only iron lines are available for this system and we therefore follow the standard procedure (Rafelski et al., 2012) and apply an upward correction of 0.3 dex to the metallicity, to correct for iron depletion and α-element enhancement.

Indeed, measurements of the velocity widths, defined as Δv_{90}, are shown to correlate with the QSO-DLA metallicities (Ledoux et al., 2006; Prochaska et al., 2008; Møller et al., 2013; Neeleman et al., 2013). In addition, Møller et al. (2013) find evidence for redshift evolution of this correlation, reminiscent of the evolution of the MzZ relation for luminosity-selected galaxies. Simulations demonstrate that galaxies with more massive halos are more likely to produce metal absorption lines in the cold gas of DLA systems with large velocity widths, while small halos produce more of metal absorption lines with low velocity widths (Pontzen et al., 2008; Tescari et al., 2009; Bird et al., 2015) supporting the interpretation of the velocity width-metallicity (VZ) relation as a mass-metallicity (MZ) relation for QSO-DLAs. In what follows we shall therefore use both VZ and MZ, chosen for clarity in the given context, to describe the relation. Whether a VZ relation also holds true for GRB-DLA galaxies is not yet known. Prochaska et al. (2008) analyse four GRB host galaxies, and while the four galaxies are in the VZ locus of QSO-DLAs, the small sample size does not allow a conclusion about the existence of a VZ relation for GRB-DLAs.

Although both QSO-DLAs and GRB-DLAs are defined based on the large column density of neutral hydrogen, they are selected in different ways; GRB-DLA systems are selected based on the star formation rate (SFR) of the galaxy hosts, while QSO-DLAs are absorption cross-section selected galaxies (Møller and Warren, 1998; Fynbo et al., 1999; Prochaska et al., 2008). Hence, they could be drawn from distinct populations of high-redshift galaxies and it is not known whether an MZ relation holds for GRB-DLA systems.

The aim of this paper is to investigate the VZ correlation for a complete literature sample of GRB-DLA galaxies, and place that into context with the relation from QSO-DLAs. Throughout this paper, when we refer to GRBs they are always long duration GRBs.

The paper is organized in the following way. The sample selection is given in section 2.3. We discuss the velocity width and the effect of spectral resolution in subsections 2.3.2 and 2.3.3. In subsection 2.3.4, the final sample is presented. Our results on the VZ relation for GRB-DLAs and several aspects of comparisons between GRB host galaxies and QSO-DLAs are presented in section 2.4. A summary of this work and our conclusions are given in section 2.5.

2.3 Data

2.3.1 Sample selection

In order to compile a GRB host DLA sample suitable for comparison to the existing samples of QSO-DLAs, we follow Møller et al. (2013) and search the literature for DLA systems in optical spectra of GRBs. In order to be included in our sample the DLA must fullfill the following requirements:
1) $\log N_{HI} \geq 20.3\ cm^{-2}$
2) it must be intrinsic to the GRB host
3) it must have a reported absorption metallicity
4) it must have at least one unsaturated low ionization line with signal-to-noise appropriate for determination of velocity width.

We find a total of 20 DLAs fulfilling all criteria, and they make up our complete literature sample spanning the redshift range from $z = 1.97$ to $z = 5.0$ (Table 2.1). Five of the systems have high resolution observations (VLT/UVES, FWHM$\sim 7\ kms^{-1}$), 8 medium (FWHM$\sim 30-60\ kms^{-1}$), and 7 low resolution (FWHM$\sim 110-480\ kms^{-1}$).

Table 2.2: High resolution line profiles used to correct Δv_{90} for low/medium resolution line profiles

Quasar/GRB	$z_{\rm DLA}$	λ [a]	Δv_{90}	Instrument	Ref.[b]
B 2355-106	1.172	2852	129	VLT/UVES	(1)
J 1201+2117	3.798	1808	485	Keck/Hires	(2)
Q 0449-1645	1.007	1862	200	VLT/UVES	(3)
Q 0454+039	0.860	2260	112	VLT/UVES	(4)
J 1107+0048	0.740	2852	178	VLT/UVES	(5)
J 0256+0110	0.725	2852	355	VLT/UVES	(5)
GRB 050730	3.969	1618	26	VLT/UVES	(6)
GRB 050820A	2.615	1608[c]	307	VLT/UVES	(7)
GRB 050922C	2.199	1608	89	VLT/UVES	(8)
GRB 071031	2.692	1559	51	VLT/UVES	(9)

[a]Rest-frame wavelength of transition lines smoothed to low/medium resolutions.
[b]References: (1) Ellison et al. (2012); (2) Rafelski et al. (2012); (3) Péroux et al. (2008); (4) Pettini et al. (2000); (5) Péroux et al. (2006); (6) Ledoux et al. (2009); (7) This work; (8) Piranomonte et al. (2008); (9) Fox et al. (2008).
[c] ESO Science Achive, Program Id: 075.A-0385(A)

2.3.2 Velocity width

To ease comparison with previous work, we use the definition of velocity width given in Prochaska and Wolfe (1997) which is the velocity interval that contains 90% of the area under the apparent optical depth spectrum (Δv_{90}). We follow Ledoux et al. (2006) and Møller et al. (2013) for the line selection rules and measuring method. The lines we select to measure Δv_{90} for GRB-DLAs in our sample are listed in Table 2.1.

The accuracy of Δv_{90} measurements critically depends on the resolution of the spectra. Quasar DLA absorption line analysis is effectively only carried out on spectra with resolution high enough that the absorption line profiles are well sampled. Due to the rapid fading of GRB optical transients (OTs), most often we do not have the luxury of high resolution spectra, and we must instead use spectra of lower resolution. Observing at low resolution causes a smearing of the absorption lines which will in turn lead to a measurement of Δv_{90} which is larger than the true Δv_{90}. The magnitude of the effect depends on both the true Δv_{90} and the resolution of the spectrum. If the true width is large then even very low resolution spectra may still be used, if the true width is very small then the width information may have been lost completely even in a medium resolution spectrum and hence only an upper limit for the velocity width can be derived. For each resolution there is a range of line widths where the effect of the smearing can be computed and corrected for. Prochaska et al. (2008) showed how such a correction could be carried out for observations with FWHM$= 45\ kms^{-1}$ resolution. Here we seek to generalize this method for a large range of resolutions.

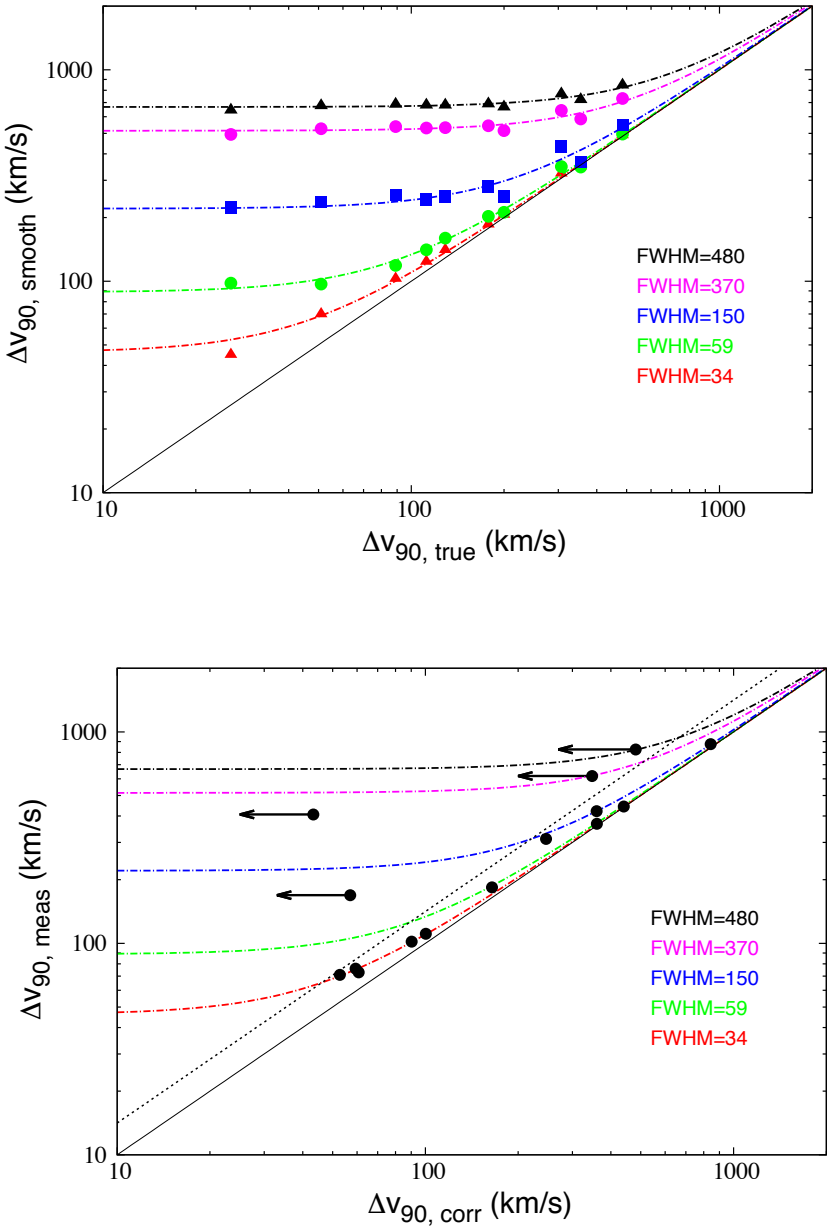

Figure 2.1: Left panel: Δv_{90} of the smoothed line profiles given in Table 2.2 versus Δv_{90} of the original profiles. Dash-dotted curves show the effect of smoothing to low resolution data as explained in section 2.3.2. The solid black line marks $\Delta v_{90,smooth}$=$\Delta v_{90,true}$; Right panel: Dash-dotted curves and full line are the same as in left panel. The dotted line marks $r = 0.4$ (see section 2.3.3). Filled circles are the measured values for medium/low resolution lines in our sample. Four points are to the left of $r = 0.4$ so we obtain only upper limit for their intrinsic widths (see Table 2.3).

2.3.3 Velocity width correction

First we examine our data set and identify the resolution (FWHM) of each of the different instrument/setting configurations used (listed in Table 2.3). Next we search the literature and select several high resolution (VLT/UVES or Keck/Hires) observed line profiles (Table 2.2) with Δv_{90} covering a wide range of widths ($\sim 25-485$ kms^{-1}). The velocity widths of those high-resolution profiles are considered to be the true line widths. We then smooth each of the high resolution lines to each of the lower resolutions (to smooth a line, we convolve it with a Gaussian with σ related to the lower resolution) and measure the $\Delta v_{90,\mathrm{smooth}}$. In Fig. 2.1 (left panel) we plot the resulting widths of the smoothed lines versus their true widths for 5 representative resolutions, using different symbols (and colour coded in the online version) for each resolution. We find that a simple hyperbola of the form

$$\Delta v_{90,\mathrm{smooth}} = (\Delta v_{90,\mathrm{true}}^2 + a^2)^{0.5} \tag{2.1}$$

where $a = 1.40 \times \mathrm{FWHM}$, provides an excellent fit in all cases. The best fit curves of the form given in equation 2.1 (determined by using a nonlinear least-squares algorithm) are shown in Figure 2.1. We can now use those fitted curves as a prescription to correct our medium and low resolution data back to their intrinsic values.

As pointed out above, the correction can only be trusted if the resolution FWHM is not large enough to completely dominate over the intrinsic width of the line. In case the intrinsic width is equal to the resolution then the measured width will be a factor $\approx \sqrt{2}$ larger, which is fully possible to correct for. We have therefore chosen a conservative approach to only trust corrections if the measured width is less than 1.4 times the width after correction. In other words, we define a parameter r such that

$$r := \frac{\Delta v_{90,meas} - \Delta v_{90,corr}}{\Delta v_{90,corr}}. \tag{2.2}$$

and only consider systems correctable if $r \leq 0.4$. The line corresponding to $r = 0.4$ is shown as a dotted straight line in Figure 2.1 (right hand panel). It is seen that four systems are to the left side of the $r = 0.4$ line, on the flat, uncorrectable part of the curves. These four systems are consequently excluded from further analysis when Δv_{90} is involved.

2.3.4 Final sample

In Table 2.3 we provide Δv_{90} before and after correction, and also r values for the 20 DLAs in our sample. For four DLA systems (GRBs 030323, 050401, 050505 and 070802) we cannot reliably correct Δv_{90} and do not include them in any further analysis which involve Δv_{90}. Our final sample consists of 16 GRB host galaxies, spanning the redshift range from $z = 1.97$ to $z = 5.0$.

2.4 Are GRB host galaxies and DLA galaxies the same?

2.4.1 Mass-Metallicity relation

DLAs are most commonly observed in the spectra of QSOs, and a large body of data is available in the literature for such DLAs. In this section we investigate whether there is any evidence that the MZ relation of the GRB host galaxies differs from that of QSO-DLAs. For that purpose, we

Table 2.3: Final results for velocity widths of the GRB-DLA sample

GRB	$\Delta v_{90,meas}$ (kms^{-1})	$\Delta v_{90,corr}$ (kms^{-1})	r	line resolution (kms^{-1})
High Resolution				
050730	34	34	...	...
050820A	300	300	...	...
050922C	89	89	...	...
071031	86	86	...	...
081008	60	60	...	...
Medium Resolution				
000926	368	362	0.022	54
060206	444	441	0.008	39
090313	184	165	0.118	59
090926A	71	53	0.344	34
100219A	76	59	0.280	34
111008	111	100	0.106	34
120327A	102	90	0.130	34
120815A	73	61	0.202	29
Low Resolution				
030323	169	≤ 57	1.963	114
050401	619	≤ 348	0.780	367
050505	407	≤ 43	8.398	290
060510B	422	360	0.173	158
070802	826	≤ 481	0.716	481
080210	312	247	0.265	137
090323	876	843	0.039	170

The second and third columns are Δv_{90} before and after correction respectively (see equation 2.1). r values as defined in equation 2.2 are given in the fourth column. The resolution (FWHM) of the selected line profiles used for measuring velocity Δv_{90} are given in the fifth column. For four DLA systems (GRBs 030323, 050401, 050505, and 070820) $r > 0.4$ and hence values of $\Delta v_{90,corr}$ for these systems are upper limits.

compare the VZ data of GRB hosts presented in section 2.3 to the QSO-DLA data presented by Møller et al. (2013).

In the upper panel of Figure 2.2 we present a plot of the two data sets. It can be seen that the observed metallicities fully overlap. A least-square fit of a straight line to both of the data sets individually, shows that the parameters of the fits are identical to within the uncertainties. For the further analysis, we adopt the slope of 1.46 for the line, as found by Ledoux et al. (2006), and we fit only intercept for the two samples individually. These fits are shown as full line (GRB hosts) and dotted line (QSO-DLAs) in Figure 2.2.

2.4.2 Redshift evolution

The MZ relation of QSO-DLA galaxies, as well as that of emission line galaxies, evolves with redshift. Our current sample is too small to independently derive a model for the redshift evolution. However, it is possible to investigate whether the data is consistent with any previously proposed model for the redshift evolution (MzZ). For each MzZ model we use

$$[\mathrm{X/H}] = [\mathrm{X/H}]_e + f(z) \tag{2.3}$$

to compute an evolution corrected metallicity ($[\mathrm{X/H}]_\mathrm{e}$), where $f(z)$ is the shift in the MZ relation as a function of redshift and z is the redshift of the galaxy.

We consider three different evolution models. Neeleman et al. (2013) study a sample of DLAs covering the redshift interval from 2 to 5, and report that the MZ relation evolves linearly with a slope of -0.32. Our first model is to use a line with this slope for the whole redshift range covered by our data as $f(z)$.

Based on a study of QSO-DLAs covering the wider redshift interval from 0.1 to 5.1, Møller et al. (2013) find that the MzZ relation of DLAs cannot be well described by a single slope. Rather the relation is constant from the highest observed redshifts to a redshift of 2.6, and evolves then linearly with a slope of -0.35 at lower redshifts. We use this prescription as our second model, and refer to it hereafter as the "late evolution" model. In the lower panel of Figure 2.2, we show the evolution corrected VZ relation based on the "late evolution" model for both the GRB host and the QSO-DLA samples. The scatter for the evolution corrected relation is lower than that of the uncorrected relation shown in the upper panel. This is a preliminary indication that the GRB host data is consistent with this evolution model.

Finally, Maiolino et al. (2008) investigate the metallicity evolution of emission line selected galaxies. Their data are consistent with linear evolution with a slope of -0.35. Our third evolution model is again to adopt this slope for evolution throughout our redshift range.

In order to compare the different evolution models, we adopt the following procedure. First, we determine the intrinsic scatter of the VZ relation before and after correcting with each of the evolution models. Following Møller et al. (2013), we separate the total observed scatter σ_tot into contributions from measurement errors $\sigma_\mathrm{met}(i)$ for each GRB host i and the intrinsic scatter of the relation σ_scatter. For this we define C^2_dof as

$$C^2_\mathrm{dof} = \sum_{i=1}^{16} (([\mathrm{M/H}](i) - 1.46 \log(\Delta v_{90}(i)) - zp) / \sigma_\mathrm{tot}(i))^2 / \mathrm{dof}, \tag{2.4}$$

where $\sigma_\mathrm{tot}(i) = \left(\sigma_\mathrm{met}(i)^2 + \sigma^2_\mathrm{scatter}\right)^{1/2}$, zp is the intercept of the fitted line, and dof is the degrees of freedom, which in this case is 15. We then set C_dof to its expected value of unity, and numerically

Table 2.4: Redshift evolution models and their effect on the intrinsic scatter of the VZ relation

Redshift evolution model	Observed $\sigma_{\rm scatter}$	Relative likelihood[a]
late evolution	0.411	1
Constant slope of -0.32	0.453	0.060
Constant slope of -0.35	0.467	0.035
Uncorrected	0.446	0.255

[a] Relative number of times that the simulation of a model reproduces the observed behaviors in scatter.

solve equation (2.4) for $\sigma_{\rm scatter}$ as a function of zp. Finally, we adopt the minimum of this function as the value of $\sigma_{\rm scatter}$.

The values found for $\sigma_{\rm scatter}$ for each of the evolution models are reported in table 2.4. The "late evolution" model provides the least intrinsic scatter, and therefore the best fit to the data. From table 2.4 it is also seen that both "constant slope" models provide larger scatter than the "uncorrected" data. We carry out sets of Monte-Carlo simulations to test the significance of this finding. In each set of simulations, we assume one of the evolution models to be true, and then count the number of times that the intrinsic scatter of the evolution corrected MZ relations computed with different models behave as the real data.

The detailed procedure is the following. In each of the simulations, we assign to each GRB host a value for $[{\rm X/H}]_e$ based on its redshift using one of the evolution models, and its measured Δv_{90}. We then add normally distributed noise based on the measurement errors $\sigma_{\rm met}$, and additional intrinsic noise $\sigma_{\rm scatter}$. We then compute the observed evolved metallicities with each of the evolution models, and determine zp and intrinsic scatter as we have done for the real data. For each imposed evolution model, we perform 10^6 simulations. We then count the number of times that applying each of the evolution corrections moves the intrinsic scatter as much as the real data do or more.

The relative number of times this happens is reported in table 2.4. We conclude that if the "late evolution" model is true, it is more than 17 times as likely to observe the scatter behave as observed than if any of the fixed slope evolution models are true. In conclusion of this section, we find that among the 3 models tested, GRB hosts are in better agreement with the late evolution model with a break around $z \sim 2.6$.

2.4.3 GRB host metallicities

It has been pointed out that GRB hosts in general have higher observed metallicities than QSO-DLAs at similar redshifts (Fynbo et al., 2006; Savaglio, 2006; Prochaska et al., 2007; Fynbo et al., 2008; Cucchiara et al., 2015). In Figure 2.3 (left panel) we show the histogram of metallicities (corrected for redshift evolution, i.e. the projection onto the left axis of Figure 2.2, lower panel) for both GRB hosts and QSO-DLAs. The median metallicity for the two samples is -1.19 and -1.53 respectively, consistent with previous reports. In the right panel we show the corresponding histograms for the Δv_{90}, and it is seen that there also is a corresponding shift of the GRB hosts towards slightly larger velocity widths (median of 95 km/s versus 75 km/s for QSO-DLAs). Seen

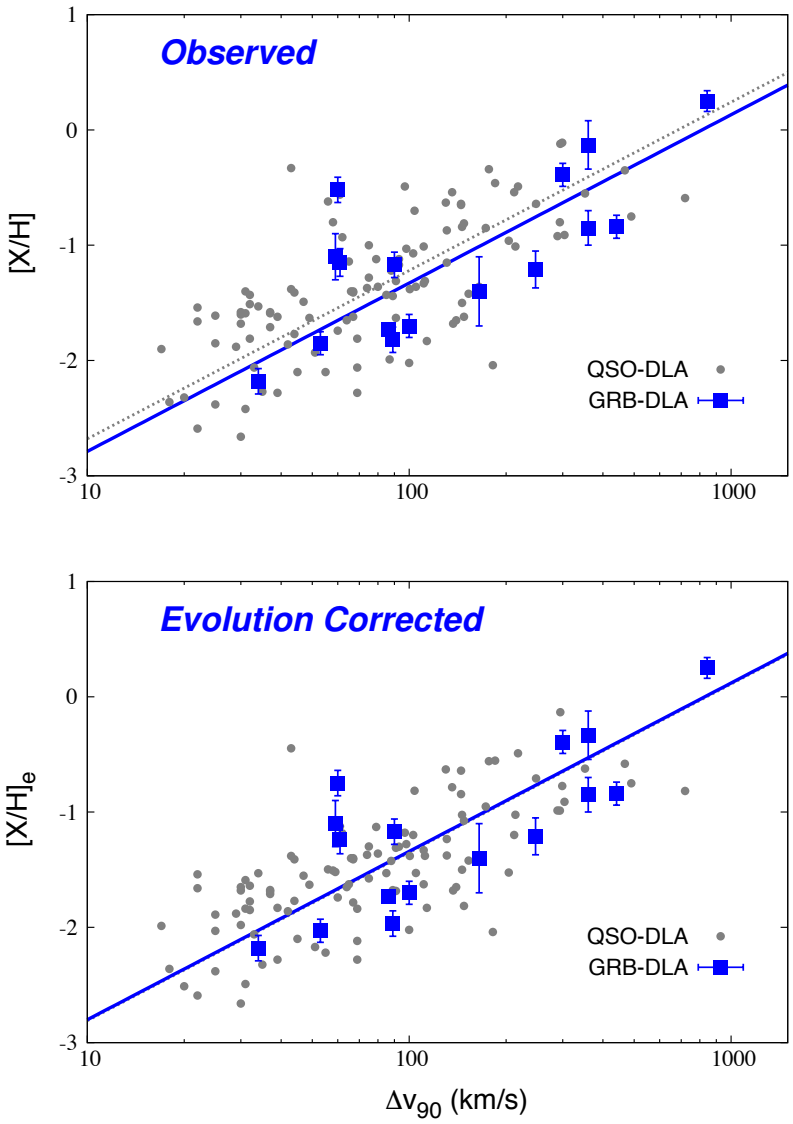

Figure 2.2: Metallicity vs velocity width for QSO-DLAs (small dots) and GRB host DLAs (large blue squares). Upper panel: observed values; Lower panel: [X/H] values corrected for the redshift evolution determined for QSO-DLAs. For both samples the scatter is reduced indicating that their MZ relations follow similar redshift evolutions. Best fits (using equation 2.4) are shown as dotted lines (QSO-DLAs), full lines (GRB-DLAs).

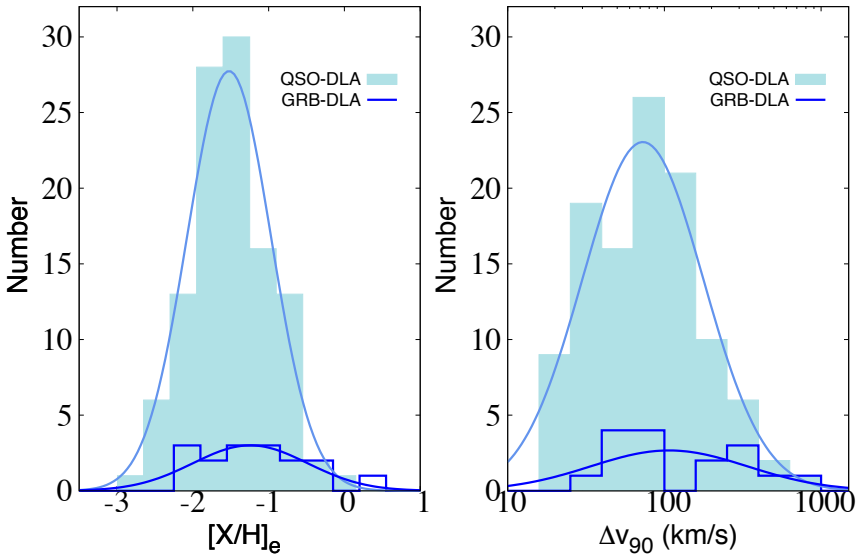

Figure 2.3: Histograms of metallicity and Δv_{90} are presented in left and right panels respectively. The light blue shade show the histograms for the 110 QSO-DLA galaxies (Møller et al., 2013) and the solid dark blue lines are for the 16 GRB-DLA galaxies in our sample (see Tables 2.1 and 2.3). Best fit Gaussians are overplotted.

together the two shifts thus form a shift of the GRB hosts along the relation towards the upper right such that both samples follow the same relation, but the GRB hosts populate the part of the diagram for slightly larger masses than QSO-DLAs. One possible way of understanding this could be that QSO-DLAs and GRB hosts are selected in two different ways from the same underlying sample. Following Fynbo et al. (2008) one may argue that GRB hosts are selected by SFR (as already demonstrated by Christensen et al. (2004)), i.e. weighted $\propto L$ (luminosity), while QSO-DLAs are selected by cold gas projected absorption area, i.e. $\propto R^2$ (gas disk radius squared). We know that $R^2 \propto L^{2t}$ where t is the Holmberg parameter (Fynbo et al., 1999), and it is now easy to understand how a shift along the relation may occur. For $t = 0.5$ there will be no shift, for $t < 0.5$ QSO-DLAs will preferentially be found to the lower left relative to GRB hosts, while for $t > 0.5$ they will in general be more Luminous than GRB hosts and therefore be found in the upper right. From Fynbo etal, (1999) we see that t is 0.4 at $z = 0$ but that it was smaller (0.25) in the past (at higher redshifts). As a consequence we predict that GRB hosts, on average, will be slightly more massive than QSO-DLAs and that the difference will be larger at higher redshifts. This may be the reason for the metallicity offset reported, but there is an additional effect which may cause GRB hosts to be shifted in the lower plot of Figure 2.2. The effect is related to the different impact paramet distributions, it is discussed in the following sections and shown in Figure 2.6. Note that where the effect of selection bias discussed above should only shift along the relation, the effect discussed below is more complex and may possibly result in a shift away from the relation. It is therefore not trivial that the two relations match so well in Figure 2.2, they could have formed two separate relations.

2.4.4 Impact parameter, metallicity gradient and gravitational well

The one thing we know is different between QSO-DLAs and GRB host DLAs are the sightlines. A QSO-DLA is sampling the HI gas in the intervening DLA galaxy and its halo via random selection. This results in a distribution of impact parameters reflecting the size, shape and inclination of the gas associated with the galaxy (for details see discussion in Møller and Warren, 1998). In contrast GRBs are mostly located closer to the centres of their hosts (typically few kpc), and therefore they sample gas closer to the centre of the galaxy.

This difference in paths changes the observed spectral lines in three different ways. First the HI column density of GRB-DLAs is higher because of the known impact parameter vs HI column density anti correlation (Møller and Warren, 1998; Zwaan et al., 2005; Krogager et al., 2012), second this will have an effect on the measured metallicity if the galaxies have metallicity gradients (van Zee et al., 1998; Swinbank et al., 2012b), and third the sightlines will sample different paths through the dark matter gravitational well of the galaxy and they will therefore sample different depths of this gravitational well. We illustrate this in Figure 2.4. In the bottom panel we see a typical QSO-DLA sightline through the shallow part of the gravitational well, in the top panel the light from a GRB passes from the centre through the deep part of the gravitational well, but only through half of it.

The first point listed above has no effect on our observations, but the other two will move the data points in the VZ plots as explained below.

Metallicity gradient

For easy comparison we correct measured metallicities to the metallicity at the centre of the galaxy. The metallicity gradient of DLA galaxies has been determined observationally to be -0.022 ± 0.004 dex per kpc (Christensen et al., 2014), but for QSO-DLAs the impact parameter is mostly unknown, and the authors also give the observationally determined mean correction which is 0.44 ± 0.10. In Figure 2.6 we show this "corrected to central" mass metallicity relation for QSO-DLAs.

We search the literature for measurements of impact parameters of the GRBs in our sample but find that only two have been reported (Castro et al., 2003; Thöne et al., 2013). We find that the image of the host has been obtained for an additional GRB (D'Elia et al., 2014) for which we measure the impact parameter. All three values can be found in Table 2.5. For the impact parameters of the remaining sample we shall use a mean value determined from a representative sample of GRB hosts. Such a sample is provided in Bloom et al. (2002) but we find that for a number of the OTs in that sample better astrometry was subsequently provided by Fruchter et al. (2006), and for those we reassess the impact parameters based on the Fruchter et al. (2006) data. From the sample of Perley et al. (2013a) we include all GRBs for which coordinates of both hosts and OTs are provided with uncertainty $\leq 0.3''$, and for which redshifts are known. The final values of impact parameters are presented in Table 2.5 and shown in histogram form in Fig 2.5.

Based on this table we find that the mean, the weighted mean, and the median values are 2.3 kpc, 2.5 kpc, and 2.3 kpc respectively. All those values are small and very similar and we choose to use the mean value for those hosts with no measured impact parameter. Following Christensen et al. (2014), we use the metallicity gradient of -0.022 dex per kpc and correct the metallicity of the GRB-DLAs in our sample to the central metallicity (Figure 2.6).

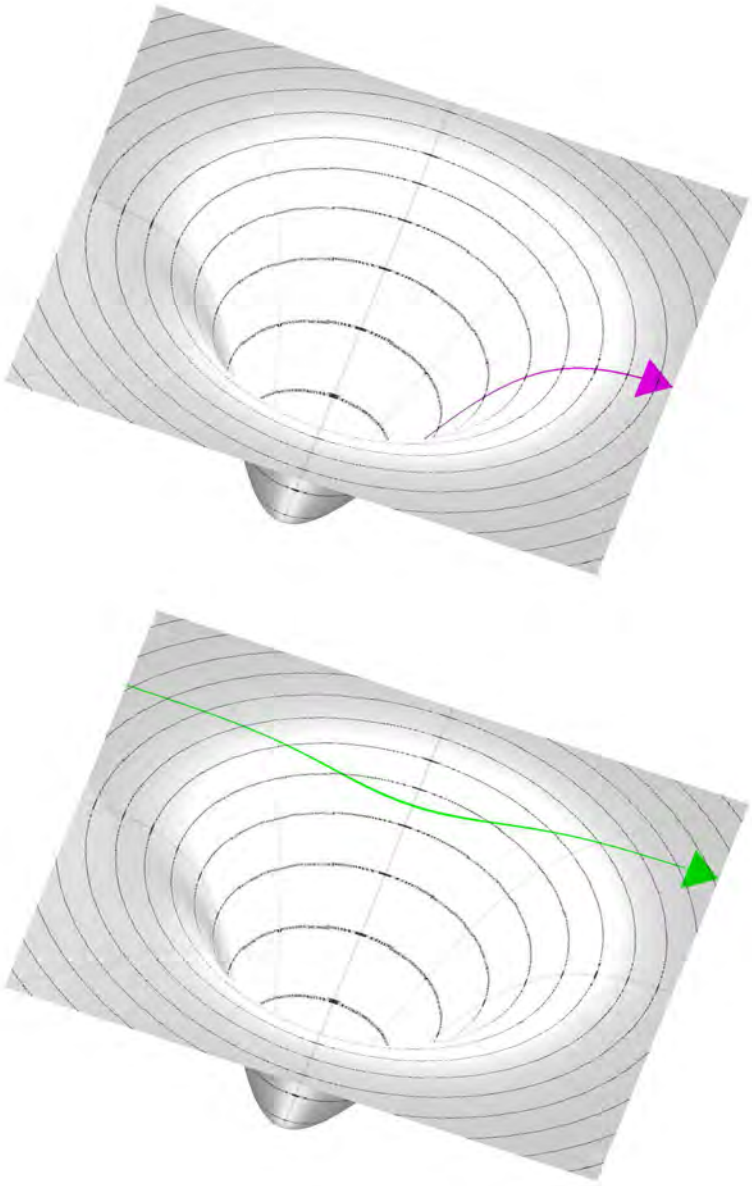

Figure 2.4: Paths of light through the potential well of the host galaxy. The upper panel illustrates a sightline from a GRB that explodes in the centre of the host galaxy, while the lower panel illustrates the random line of sight of a QSO that intersects an intervening galaxy.

Table 2.5: List of impact parameters

GRB	Redshift	impact parameter (kpc)	error-bar (kpc)	Reference[a]
GRBs in our sample				
000926	2.038	0.29	0.037	(1)
100219A	4.667	2.6	0.2	(2)
120327A	2.815	3.19	2.39	(3)
other GRBs				
970228	0.695	0.17	0.24	(3)
970508	0.835	0.09	0.09	(4)
970828	0.958	4.05	4.33	(4)
971214	3.418	1.11	0.56	(4)
980425	0.008	2.34	0.01	(4)
980613	1.096	0.78	0.67	(4)
980703A	0.966	0.96	0.54	(4)
990123	1.6	6.11	0.03	(4)
990506	1.31	2.68	4.14	(4)
990510	1.619	0.60	0.08	(4)
990705	0.84	7.17	0.38	(4)
990712	0.434	0.30	0.49	(4)
991208	0.706	0.00	0.62	(3)
991216	1.02	3.12	0.28	(4)
000301C	2.03	0.62	0.06	(4)
000418	1.118	0.20	0.56	(4)
010222	1.477	0.376	0.76	(3)
010921	0.45	2.53	0.52	(3)
011121	0.362	3.98	1.11	(3)
011211	2.141	2.97	2.97	(3)
020405	0.69	5.95	1.57	(3)
020813	1.255	0.18	0.19	(3)
020903	0.251	2.23	2.23	(3)
021004	2.330	0.37	0.37	(3)
021211	1.006	0.71	0.36	(3)
030115	2.5	2.53	1.52	(3)
030329	0.168	0.37	0.13	(3)
040924	0.859	1.70	1.02	(3)
041006	0.716	2.54	1.28	(3)
050915A	2.527	6.72	0.90	(5)
051022	0.8	1.83	1.51	(5)
061222A	2.088	3.12	1.03	(5)
070802	2.455	3.63	1.50	(5)
080325	1.78	5.73	1.04	(5)
080607	3.036	3.30	1.43	(5)
081221	2.26	3.97	0.76	(5)

Redshift of GRBs are given in second column. The third and fourth columns present the impact parameter and corresponding error.

[a] References: (1) Castro et al. (2003); (2) Thöne et al. (2013); (3) this work; (4) Bloom et al. (2002); (5) Perley et al. (2013a)

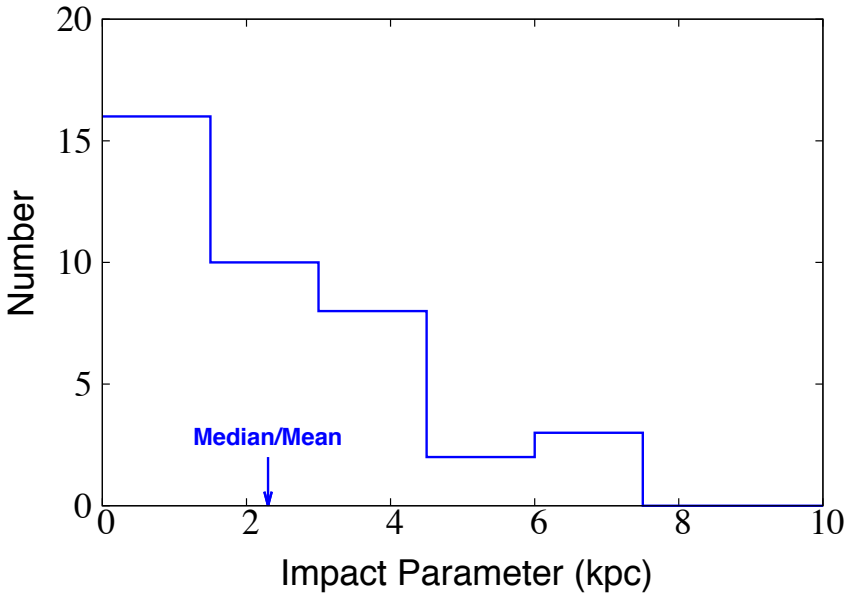

Figure 2.5: Histogram of impact parameters of GRB host galaxies given in Table 2.5 with both mean and median equal to 2.3 *kpc*

Potential well depth

The line of sight to the OT in a GRB host samples only half of the gravitational well in which the host resides (see Figure 2.4, upper panel). It is hard to predict exactly which value for Δv_{90} one would have observed in case the line had been complete through the other side of the host, but it certainly would not be less than for the observed half galaxy. One could make the simple assumption that the cold clumps in the ISM and halo gas move randomly, but that most are bound inside the gravitational well. In that case Δv_{90} would increase by about a factor $\sqrt{2}$. The same type of argument can be applied to sightlines to QSOs through intervening DLA galaxies. Such sightlines will in most cases not pass close to the centre, but rather at impact parameters of order $\approx$ 10kpc (see Figure 2.4, lower panel). Again, only a fraction of the full well will be sampled, and the measured Δv_{90} will be smaller than if sampled through the centre. The precise magnitude of those effects is hard to quantify. Detailed high resolution hydro-dynamic simulations would be required to get an estimate.

In Figure 2.6 we apply the empirical corrections for metallicity gradients, and it is seen that there is now a large shift between the two populations. If we interpret this shift as an effect of different sampling of gravitational wells, then the shift corresponds to a factor 2 change of Δv_{90} for galaxies with the same metallicity at a given redshift. The shift is in the sense that QSO-DLAs have Δv_{90} a factor of 2 less than a GRB host with the same metallicity. The shift is therefore in the direction we would expect in case it is due to the gravitational well sampling effect. This may therefore be the effect we have predicted, but at present it is not possible to conclusively prove this.

It is curious, though, that the two samples overlap so perfectly in Figure 2.2. This means that either there are no metallicity gradients in neither QSO-DLA galaxies, nor in GRB hosts, and also there is no effect due to the gravitational well sampling - or, the effect of metallicity gradients ex-

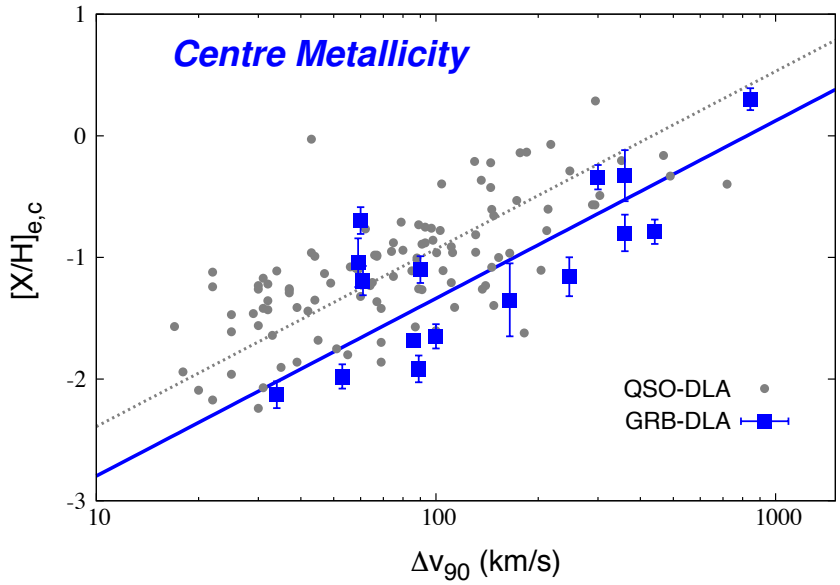

Figure 2.6: Metallicity corrected with the late evolution model and also corrected to the central metallicity ($[X/H]_{e,c}$) vs velocity width for QSO-DLAs (small dots) and GRB host DLAs (large blue squares). Best fits (using equation 2.4) are shown as dotted lines (QSO-DLAs), full lines (GRB-DLAs).

actly cancels the effect of gravitational well sampling. If the latter is the case then this means that the general concept of an MZ relation plus metallicity gradients simply is a convolved and roundabout way of describing a much simpler underlying relation between metallicity and gravitational well depth.

2.4.5 Stellar mass

A prescription for computation of the stellar mass of QSO-DLA galaxies from only metallicity and redshift was given in Møller et al. (2013). Christensen et al. (2014), improved this prescription by adding the effect of metallicity gradients and also performed a test comparing the computed stellar mass to the measured stellar mass from the SED fits. This test was carried out using the complete set of QSO-DLA galaxies for which the test is currently possible. They concluded that the prescription is confirmed for galaxies of stellar masses down to $\log(M_\star/M_\odot) = 8$, while for lower stellar masses there are no available data. Here we use the prescription from Christensen et al. (2014) (their equation (3) including the metallicity gradient term Γb) to compute the predicted stellar masses of all the host galaxies in our sample (listed in Table 2.6). For 3 of those, stellar masses have been determined directly via SED fitting (also provided in Table 2.6). For the host of GRB 090323, we use the photometric data given in McBreen et al. (2010b) and determine the stellar mass following the procedure described in Glazebrook et al. (2004) and the initial mass function given in Baldry and Glazebrook (2003). In order to obtain the full distribution function of the allowed mass, a Monte Carlo simulation re-sampling the photometric errors is done. We measure the stellar mass for this host to be $\log(M_\star/M_\odot) = 11.20 \pm 0.75$. The large error bar is due to only

Table 2.6: For the sample of the GRB-DLA galaxies, redshift, impact parameter, and metallicity are presented in second, third, and fourth columns respectively. Predicted and measured stellar masses are given in the fifth and sixth columns.

GRB	redshift	$b\ (kpc)$	$[X/H]$	Predicted mass, $\log(M_\star/M_\odot)$	Measured mass, $\log(M_\star/M_\odot)$
000926	2.0379	0.29	-0.13 ± 0.21	9.91 ± 0.81	9.52 ± 0.84
030323	3.3718	...	-1.26 ± 0.20	8.34 ± 0.80	...
050401	2.8992	...	-1.0 ± 0.4	8.80 ± 1.01	...
050505	4.2748	...	$-1.2\pm...$	$8.45\pm>0.72$	...
050730	3.9686	...	-2.18 ± 0.11	6.73 ± 0.75	...
050820A	2.6147	...	-0.39 ± 0.10	9.88 ± 0.74	$8.64^{+0.58}_{-0.23}$
050922C	2.1992	...	-1.82 ± 0.11	7.11 ± 0.75	...
060206	4.048	...	-0.84 ± 0.10	9.08 ± 0.74	...
060510B	4.941	...	-0.85 ± 0.15	9.07 ± 0.77	...
070802	2.4549	3.63	-0.50 ± 0.68	9.64 ± 1.40	$9.7^{+0.2}_{-0.3}$
071031	2.6922	...	-1.73 ± 0.05	7.52 ± 0.73	...
080210	2.641	...	-1.21 ± 0.16	8.43 ± 0.78	...
081008	1.9683	...	-0.52 ± 0.11	9.26 ± 0.75	...
090313	3.3736	...	-1.40 ± 0.30	8.10 ± 0.90	...
090323	3.569	...	0.25 ± 0.09	11.00 ± 0.74	11.20 ± 0.75
090926A	2.1071	...	-1.85 ± 0.10	7.00 ± 0.74	...
100219A	4.6672	2.6	-1.10 ± 0.20	8.64 ± 0.80	...
111008	5.0	...	-1.70 ± 0.10	7.57 ± 0.74	...
120327A	2.8145	3.19	-1.17 ± 0.11	8.54 ± 0.75	...
120815A	2.358	...	-1.15 ± 0.12	8.39 ± 0.75	...

References for measured stellar masses: Savaglio et al. (2009b) for 000926; Chen et al. (2009) for 050820A; Krühler et al. (2011a) for 070802; This work for 090323.

having upper limits on the rest frame optical photometry.

We find the measured stellar masses for these four hosts to be in complete agreement with our computed values provided we use the prescription including the metallicity gradient. If we instead use equation (1) from Christensen et al. (2014), which assumes a constant offset between absorption metallicity and emission metallicity, then the agreement is much poorer with the computed masses in the mean being 1 dex higher than the measured stellar masses. I.e. our data support the hypothesis that the stellar masses of GRB-DLA galaxies follow the same prescription as do QSO-DLA galaxies, and that they have metallicity gradients with a slope similar to that of QSO-DLAs.

In a related study of a sample of 18 low redshift GRB hosts with measured emission line metallicities and stellar masses from SED fits, Mannucci et al. (2011) showed that those host galaxies follow the same M-Z relation as SDSS galaxies, but only after correcting for the high SFR which is a result of the SFR weighted selection we discussed in section 2.4.3. It therefore appears that the available samples of emission selected galaxies, GRB selected galaxies, and DLA selected galaxies follow the same M-Z relations (when corrected for their specific selection function) and likely are drawn from the same underlying galaxy sample.

In Section 2.4.3 we described how the metallicity offset seen in Figure 2.3 could be understood as a result of selection functions, but from Figure 2.6 it is seen that the offset could just as well be caused by the effect of metallicity gradients and different impact parameter distributions. Our sample covers a range of stellar masses from $10^{6.7}$ to 10^{11} $M_{\odot}$, with a median of $10^{8.5}$ (Table 2.6). This median mass is identical to that reported by Møller et al. (2013) for DLA galaxies which, held together with the better fits using metallicity gradients described above, supports that at least part of the metallicity offset is a result of different impact parameter distributions. In that case the shift between the two samples seen in Figure 2.6 is most easily interpreted as the effect of different paths through the gravitational potentials.

The interpretation of the observed distribution of data points in Figure 2.2 is therefore complex. Effects of redshift evolution, impact parameter distributions, metallicity gradients, and differently weighted selection functions all work to move the data-points, which causes at least part of the scatter of the relation. We here repeat from the conclusions of Møller et al. (2013) that in order to move forward towards an understanding of those objects we need to identify and understand the sources of the scatter. One of the sources (redshift evolution) has already been identified. Christensen et al. (2014) recently found that half of the scatter in their sample was removed when the effect of metallicity gradients were included. Here we have proposed that the effect of gravitational well depth could be an additional cause of scatter.

2.5 Conclusions

Most long duration GRB host galaxies display strong intrinsic DLA absorption systems similar in nature to the intervening DLA systems seen in QSO spectra. The GRB host systems are, however, different in two ways: they originate inside the host galaxies rather than behind them and they are found at much smaller impact parameters. In addition they are also reported generally to have higher HI column densities and often to have higher metallicities than intervening DLAs at the same redshift.

It is important to establish if those differences simply are a result of two different selection functions applied to the same underlying sample of high redshift galaxies, or if the two types of galaxies are truly two different populations.

We have here analysed the mass/metallicity/redshift relations of a complete literature sample of GRB host galaxies and a sample of intervening DLA galaxies in order to address this question. We have found that
1) The two samples are fully consistent with being drawn from the same underlying population with a single MZ relation, and a single redshift evolution of this relation with a break around $z \approx 2.6$. GRB hosts are in better agreement with this redshift evolution compared to linear evolutions with constant slopes.
2) There is evidence that the GRB host galaxies have higher metallicities, but this is most likely a secondary correlation. The primary correlation is with either impact parameter, with stellar mass, or, presumably, with a combination of the two. The smaller impact parameters combined with a metallicity gradient will produce a metallicity offset, SFR selection bias is predicted to select galaxies of somewhat larger stellar mass than DLA galaxies which will likewise cause an offset in metallicity.
3) There is weak evidence that the Δv_{90}-metallicity relation for the GRB hosts is offset towards larger Δv_{90} values, as one would predict since their sightlines pass through a deeper part of the dark matter halo potential well than a random sightline to an intervening DLA in a halo of the same mass.

It has been shown previously that QSO-DLAs and Lyman Break Galaxies (LBG) are consistent with being drawn from the same underlying population by two very different selection functions, where QSO-DLAs are drawn from the very low-mass end of the LBG population (Møller et al., 2002). With the results presented here we have now added long duration GRB hosts to this list, which means that we have made another important step towards a global description of galaxies and galaxy evolution in the early universe.

Since the sample used in this pilot study is limited, it will be quite feasible to improve the accuracy of all results reported here simply by increasing the sample size. GRB host are ideally suited to shed light on the structure of high redshift galaxies. They combine the data from emission selected galaxies directly with those of absorption selected galaxies. I.e. we obtain in the ideal case both absorption metallicity, emission metallicity, stellar mass from SED fits, impact parameter and Δv_{90} for a single galaxy.

Acknowledgment

We would like to thank Jason X. Prochaska for providing the HI column density for the host of GRB 090313 prior to publication. We thank an anonymous referee for a careful reading of our manuscript and for many insightful and valuable comments which significantly improved the presentation of our results. We thank Karl Glazebrook and Damien Le Borgne for helping with the stellar mass calculation of the host of GRB 090323. MA thanks Max-Planck-Institut für Astrophysik for hosting her during the initial part of this work. JPUF acknowledges support from the ERC-StG grant EGGS-278202. This work was funded by an ESO DGDF grant to PM and WF. The Dark Cosmology Centre is funded by the Danish National Research Foundation.

Chapter 3

Absorption versus emission, neutral gas veres ionised gas

This chapter containes the folllowing paper:
"Connecting absorption and emission studies of gas metallicity and kinematics in GRB host galaxies"
Arabsalmani M., et al.
Sumitted to MNRAS in October 2016

3.1 Abstract

We present a comprehensive study of gas kinematics in both absorption and emission in GRB host galaxies, the galaxy population that provides the unique opportunity for such a study. We explore the connection between kinematic characteristics of gas in different phases, and investigate their relations with other galaxy properties. We find that the velocity widths of ionised and neutral gas, obtained from emission and absorption methods respectively, correlate with each other. We also show that the velocity widths can be used as proxies of stellar mass. We find the absorption velocity widths to be larger than expected and speculate this to be due to the significant contribution from interacting systems and mergers.

We also study the mass-metallicity relation for GRB host galaxies using a sample of GRB hosts with uniformly measured stellar mass and metallicities, spanning a redshift range of $z \sim 0.3 - 3.4$. We show that with considering the redshift evolution of the relation, GRB selected galaxies follow the mass-metallicity relation of the general population of star forming galaxies. We also investigate the relation between metallicity and gas kinematics in these galaxies using both absorption and emission methods. Finally, we infer a relation between the metallicities measured from absorption and emission methods.

3.2 Introduction

Gamma Ray Bursts (GRBs) are flashes of gamma ray, followed by the afterglow emission in wavelengths starting from X-ray up to radio. These bright explosions are divided into two different classes based on mainly the duration of their prompt emission. The ones with long durations are

believed to originate in the collapse of very massive stars. Indeed, they have proven observationally to be located in the star-forming regions of their host galaxies. In this paper we only discuss long duration GRBs and hereafter the term 'GRB' refers only to long duration GRBs. GRBs are dust-penetrating and extremely bright explosions, and are detectable up to very high redshifts (highest confirmed spectroscopic redshift for a GRB is $z = 8.2$, Tanvir et al., 2009). The detectability of GRBs is independent of the brightness and dust content of their host galaxies. Thus GRB-selected galaxies provide a unique method for sampling star-forming galaxies throughout the Universe, without being affected by a luminosity bias.

The presence of the GRB afterglows makes it possible to study their host galaxies through the absorption features that their interstellar media (ISM) imprint on the GRBs' spectra. Even at the highest redshifts, where the hosts are often too faint to be detected in emission, their properties can be inferred through absorption, making GRBs powerful tracers of the earliest galaxies in the Universe. Since GRBs are transients, emission studies of their host galaxies do not suffer from their presence (see McGuire et al., 2016, for HST detection of three GRB host galaxies at $z \sim 6$). This is not the case for the absorbers in the sightlines of quasars, where even at low redshifts detecting the counterpart galaxies have proven to be extremely challenging due to the bright background quasars. Thus, GRBs provide the unique opportunity of studying a population of star-forming galaxies in both emission and absorption (see for e.g. Thöne et al., 2007).

The emission and absorption profiles trace different regimes and phases of gas. As a result, the two sets of line profiles typically have different kinematic signatures (e.g. Castro-Tirado et al., 2010). Also, metallicity measurements from absorption and emission methodes not only trace the metal enrichment of gas in different regions of galaxies but also are based on totally different measurement methods. The information inferred from the two methods are complementary to each other. Independent measurements of galaxy properties, such as metallicity and gas kinematics, using both absorption and emission methods and comparing them provide us with the most complete picture of galaxy properties. GRB host galaxies provide an excellent choice for such studies.

Absorption studies of GRB host galaxies have led to accurate measurements of abundances, metallicities, dust, and kinematic properties up to redshifts $z \sim 6.0$ (e.g. Prochaska et al., 2008; Fynbo et al., 2009; Zafar et al., 2011; Arabsalmani et al., 2015a; Cucchiara et al., 2015). Emission studies have provided stellar masses and emission line metallicity measurements at redshifts as high as $z \sim 3.0$. (e.g. Savaglio et al., 2009b; Castro Cerón et al., 2010; Krühler et al., 2015). But yet the connection between the information obtained from the two methods lacks.

In this paper we present a large sample of GRB host galaxies with uniformly measured properties from absorption and emission methods. We use this sample to make a connection between our understanding of this galaxy population from absorption methods to those from emission methods. Our sample and the methods used to measure the galaxy properties are described in section 3.3. In sections 3.4 we investigate the kinematic characteristics of gas in both emission and absorption, the connection between them and their relations with other galaxy properties such as stellar mass and metallicity. We present the mass-metallicity relation for our large GRB host sample in section 3.5 and compare it with the general population of star-forming galaxies. Finally in section 3.6 we explore the relation between the emission and absorption metallicities for GRB host galaxies. Our results are summarised in section 3.7.

3.3 Sample and measurements

3.3.1 Sample

Metallicity and velocity width obtained from both absorption and emission, and stellar mass are the main properties that we include in this study. We use spectroscopic data from VLT/X-shooter, as well as spectroscopic and photometric data from the literature, to put together a large sample with emission and/or absorption observations.

Our emission study sample includes 62 GRB host galaxies, all with measured emission line velocity width, 43 of the 62 hosts with emission metallicity measurement, and 52 of them with stellar mass measurement (see Tab. 3.1). Our absorption study sample includes 23 GRB host galaxies, all with measured absorption velocity width, 19 with absorption metallicity measurement, and 7 with stellar mass measurement (see Tab. 3.2). For comparing absorption and emission kinematics, we have 10 galaxies with measured velocity widths in both emission and absorption (see Tab. 3.3, some are already listed in Tab. 3.1 and 3.2). We have only one GRB host in our sample (GRB 121024) with both emission and absorption metallicity measurements.

We uniformly measure the stellar masses (presented in section 3.3.2) for 53 GRB host galaxies. All the emission metallicity measurements are taken from Krühler et al. (2015) in order to have homogeneous measurements (and with same calibrations for strong-line diagnostics). The absorption metallicity measurements can be inferred only for the GRB hosts with detected Lyman-α absorption lines. This is possible only for GRBs at redshift $z \gtrsim 1.7$ due to the atmospheric cut-off (since the optical afterglows fade away very fast, GRBs' optical afterglows have always been detected with ground based telescopes). For those GRBs with detected Lyman-α absorption lines, and where S/N of the spectra have allowed the metallicity measurements, we take the inferred absorption metallicities from the literature. We measure the velocity widths of the absorption profiles for 28 GRB host galaxies for which GRBs' optical afterglows have high enough S/N and spectral resolution (see section 3.3.3). We take the emission line velocity width measurements from Krühler et al. (2015).

3.3.2 Stellar mass measurements (to be completed by Thomas)

Host Photometry

To derive physical parameters, in particular mass, of the stellar component of the GRBs' host galaxies, we follow a standard approach and fit broad-band spectral energy distributions with single stellar population synthesis models. We hence heavily rely on accurate and precise photometry over a large wavelength range, which traditionally has been very tedious and expensive to obtain due to the faintness of the targets.

Fortunately, we can draw now from several large photometric catalogs of GRB hosts that have just been published recently. Most importantly, these are the series of papers by D. Perley which includes extensive Spitzer and Keck data (Perley et al., 2009, 2013b, 2015, 2016b,d), the compilation of HST photometry (Blanchard et al., 2016), and VLT imagery obtained within the TOUGH survey (Hjorth et al., 2012a; Krühler et al., 2012; Schulze et al., 2015b). Smaller data sets from Savaglio et al. (2009a); McBreen et al. (2010a); Krühler et al. (2011b) and Vergani et al. (2015b) as well as further photometric data for individual galaxies as referenced in Tab. 3.1 and 3.2 are also used in the analysis.

We also obtained new photometry ourselves to complement already existing data. These include, for example, NIR data for the host GRB 090323 to sample the rest-frame optical wavelength

Table 3.1: Emission study GRB host sample (62 GRB hosts)

GRB	Redshift	$\sigma_{H\alpha}$ (km s^{-1})	12 + log(O/H)	$\log M_*/M_\odot$
050416A	0.654	47 ± 4	$8.46^{+0.11}_{-0.11}$	$9.23^{+0.21}_{-0.28}$
050824	0.828	48 ± 5	$8.11^{+0.18}_{-0.20}$	$8.23^{+0.38}_{-0.35}$
050915A	2.528	87 ± 10	...	$10.66^{+0.07}_{-0.12}$
051016B	0.936	58 ± 4	$8.27^{+0.15}_{-0.20}$	$9.45^{+0.11}_{-0.11}$
051022A	0.806	88 ± 5	$8.49^{+0.09}_{-0.09}$	$9.84^{+0.07}_{-0.06}$
051117B	0.481	85 ± 11	$9.0^{+0.16}_{-0.16}$	$10.31^{+0.09}_{-0.09}$
060204B	2.339	85 ± 8	...	$9.81^{+0.35}_{-0.23}$
060306	1.560	60 ± 14	...	$9.94^{+0.15}_{-0.08}$
060604	2.1355	68 ± 13	$8.10^{+0.35}_{-0.28}$	...
060719	1.532	42 ± 5	$8.61^{+0.20}_{-0.24}$	$9.83^{+0.13}_{-0.26}$
060729	0.543	66 ± 16	...	$8.39^{+0.11}_{-0.13}$
060814	1.922	132 ± 11	...	$10.03^{+0.16}_{-0.07}$
061021	0.345	62 ± 5	$8.61^{+0.11}_{-0.12}$	$8.52^{+0.29}_{-0.44}$
061110A	0.758	16.1 ± 4.8	..	$8.01^{+0.17}_{-0.19}$
061202	2.254	64 ± 7	...	$9.64^{+0.24}_{-0.25}$
070306	1.497	121 ± 55	$8.54^{+0.09}_{-0.09}$	$10.35^{+0.07}_{-0.10}$
070318	0.840	53 ± 5	...	$8.73^{+0.44}_{-0.27}$
070328	2.063	93 ± 14	...	$9.65^{+0.21}_{-0.26}$
070521	2.087	249 ± 108	...	$10.50^{+0.05}_{-0.07}$
071021	2.452	100 ± 17	...	$10.10^{+0.43}_{-0.07}$
080207	2.086	136 ± 18	$8.74^{+0.15}_{-0.15}$	$11.09^{+0.05}_{-0.05}$
080413B	1.101	39 ± 5	$8.29^{+0.32}_{-0.30}$	$9.06^{+0.39}_{-0.28}$
080602	1.820	91 ± 13	...	$10.20^{+0.29}_{-0.31}$
080605	1.641	80 ± 6	$8.54^{+0.09}_{-0.09}$	$9.80^{+0.13}_{-0.10}$
080805	1.505	54 ± 12	$8.49^{+0.13}_{-0.14}$	$9.96^{+0.12}_{-0.12}$
081109	0.979	108 ± 6	$8.75^{+0.09}_{-0.09}$	$9.95^{+0.07}_{-0.06}$
081210	2.063	118 ± 12	...	$10.07^{+0.20}_{-0.17}$
081221	2.259	93 ± 12	...	$10.08^{+0.05}_{-0.06}$
090113	1.749	70 ± 9	...	$9.89^{+0.16}_{-0.16}$
090323	3.583	60 ± 13	...	$10.29^{+0.20}_{-0.25}$
090407	1.448	109 ± 8	$8.85^{+0.13}_{-0.13}$	$10.17^{+0.10}_{-0.49}$
090926B	1.243	65 ± 4	$8.34^{+0.15}_{-0.17}$	$9.88^{+0.23}_{-0.22}$
091018	0.971	57 ± 10	$8.78^{+0.18}_{-0.19}$	$9.51^{+0.10}_{-0.09}$
091127	0.490	30 ± 5	$8.07^{+0.18}_{-0.20}$	$8.83^{+0.07}_{-0.07}$
100418A	0.624	56 ± 4	$8.52^{+0.10}_{-0.10}$	$9.169^{+0.13}_{-0.11}$
100424	2.4656	87 ± 5	$7.93^{+0.18}_{-0.25}$	...
100508A	0.520	80 ± 11	$8.68^{+0.10}_{-0.10}$	$9.40^{+0.13}_{-0.12}$
100606	1.5545	107 ± 36	$8.71^{+0.21}_{-0.19}$	...
100615	1.3978	45 ± 5	$8.40^{+0.13}_{-0.12}$	...
100621A	0.543	82 ± 4	$8.52^{+0.10}_{-0.10}$	$9.23^{+0.06}_{-0.06}$

Table 3.1: Continuation

GRB	Redshift	σ (km s^{-1})	12 + log(O/H)	$\log M_*/M_\odot$
110808	1.3490	40 ± 4	$7.93^{+0.23}_{-0.31}$	...
100816A	0.805	111 ± 30	$8.75^{+0.16}_{-0.18}$	$10.06^{+0.25}_{-0.13}$
110818A	3.361	89 ± 8	$8.25^{+0.17}_{-0.25}$	$10.48^{+0.39}_{-0.24}$
110918A	0.984	126 ± 18	$8.93^{+0.11}_{-0.11}$	$10.76^{+0.54}_{-0.32}$
111123	3.1513	135 ± 21	$8.01^{+0.28}_{-0.28}$	...
111211A	0.479	38 ± 8	...	$8.86^{+0.23}_{-0.22}$
111228A	0.715	19.7 ± 5.5	...	$8.82^{+0.28}_{-0.24}$
120118B	2.9428	193 ± 8	$7.89^{+0.17}_{-0.23}$	...
120119A	1.729	104 ± 17	$8.60^{+0.14}_{-0.14}$	$10.01^{+0.046}_{-0.10}$
120422A	0.283	25 ± 4	$8.39^{+0.09}_{-0.09}$	$8.91^{+0.09}_{-0.06}$
120624B	2.197	77 ± 6	$8.43^{+0.20}_{-0.27}$	$10.84^{+0.53}_{-0.37}$
120714B	0.399	34 ± 4	$8.39^{+0.11}_{-0.11}$	$8.84^{+0.14}_{-0.15}$
120722A	0.959	56 ± 4	$8.48^{+0.10}_{-0.10}$	$9.52^{+0.21}_{-0.18}$
121024A	2.301	88 ± 4	$8.41^{+0.11}_{-0.12}$	$10.16^{+0.20}_{-0.18}$
130427A	0.340	40 ± 5	$8.57^{+0.12}_{-0.13}$	$8.92^{+0.43}_{-0.15}$
130925A	0.348	49 ± 5	$8.73^{+0.08}_{-0.08}$	$9.13^{+0.13}_{-0.09}$
131103A	0.596	87 ± 7	$8.48^{+0.10}_{-0.12}$	$8.76^{+0.16}_{-0.17}$
131105	1.6854	52 ± 11	$8.61^{+0.20}_{-0.17}$	...
131231A	0.643	33 ± 4	$8.45^{+0.11}_{-0.12}$	$8.78^{+0.20}_{-0.17}$
140301	1.4155	117 ± 6	$8.89^{+0.09}_{-0.09}$	...
140430	1.6019	40 ± 7	$8.67^{+0.19}_{0.18}$	...
140506A	0.889	61 ± 9	...	$9.11^{+0.24}_{-0.21}$

Additional references for individual galaxies: Vergani et al. (2015b) for GRB 061021 and GRB 050416, Filgas et al. (2011b) for GRB 080413B, Rossi et al. (2012b) for GRB 080602, Vergani et al. (2015b) and Filgas et al. (2011a) for GRB 091127, Pérez-Ramírez et al. (2013) for GRB 100816A, Elliott et al. (2013b) for GRB 110918A, Morgan et al. (2014) for GRB 120119A, Schulze et al. (2014) for GRB 120422A, de Ugarte Postigo et al. (2013) for GRB 120624B, Friis et al. (2015b) for GRB 121024A, Xu et al. (2013) for GRB 130427A, Kelly et al. (2013) for GRB 130702A, Schady et al. (2015) for GRB 130925A, and Fynbo et al. (2014) for GRB 140506A.

Table 3.2: Absorption study GRB host sample (23 GRB hosts)

GRB	Redshift	Δv_{90} (km s^{-1})	[X/H]	$\log M_*/M_\odot$
000926	2.0379	362	-0.13±0.21	...
0507030	3.969	34	-2.18±0.11	...
050820A	2.6147	300	-0.39±0.10	$8.96^{+0.26}_{-0.28}$
050922C	2.199	89	-1.82±0.11	...
060206	4.048	441	-0.84±0.10	...
060510B	4.941	360	-0.85±0.15	...
071031	2.692	86	-1.73±0.05	...
080210	2.641	247	-1.21±0.16	...
081008	1.968	60	-0.52±0.11	...
090313	3.374	165	-1.40±0.30	...
090323	3.5832	843	0.25±0.09	$10.42^{+0.07}_{-0.13}$
090926	2.107	53	-1.85±0.10	...
091018	0.971	147	...	$9.51^{+0.10}_{-0.09}$
100219	4.667	59	-1.10±0.20	...
100418A	0.624	182	...	$9.16^{+0.13}_{-0.11}$
111008	5.0	100	-1.70±0.10	...
111211A	0.479	98	...	$8.86^{+0.23}_{-0.22}$
120327	2.815	90	-1.17±0.11	...
120815	2.358	61	-1.15±0.12	...
120909	3.9293	145	-0.66±0.16	...
121024	2.301	434	-0.40±0.12	$10.16^{+0.20}_{-0.18}$
130408	3.757	97	1.24±0.12	...
131231A	0.643	143	...	$8.78^{+0.10}_{-0.17}$

For GRBs 120909, 121024, and 130408 we have the VLT/X-shooter spectra and Δv_{90} is measured from NiII 1370, ZnII 2026, and SiII 1808 with r parameters of 0.06, 0.01, and 0.13 respectively. For these three GRB hosts metallicity measurements are taken from Cucchiara et al. (2015). The Δv_{90} measurements for the rest of the sample are presented in Arabsalmani et al. (2015a) and we refer to the references therein for metallicity measurements.

Table 3.3: The sample of GRB host galaxies with measured velocity widths in both absorption and emission. Columns 1 to 6 are GRB name, redshift, $\sigma_{H\alpha}$, velocity width of the absorption line (Δv_{90}), the absorption profile used for Δv_{90} measurements, and the smearing correction factor as defined in equation 3.2.

GRB	Redshift	$\sigma_{H\alpha}$ (km s^{-1})	Δv_{90}[a] (km s^{-1})	low ion line	r
090323	3.583	60 ± 13[b]	843	SiII, 1808	0.04
091018	0.971	57 ± 10	146	SiII, 1808	0.15
100418A	0.62	56 ± 4	181	MnII, 2576	0.10
100814A	1.439	31 ± 5	211	FeII, 2600	0.03
111209A	0.677	35 ± 5	187	FeII, 2374	0.10
111211A	0.4786	38 ± 8	98	MnII, 2594	0.31
111228A	0.7164	19.7 ± 5.5	30	MnII, 2594	1.90
120815A	2.359	28 ± 5	61	MnII, 2594	0.20
121024A	2.301	88 ± 4	437	MnII, 2594	0.01
130427A	0.340	40 ± 5	60	MnII, 2576	0.72
131231A	0.643	33 ± 4	143	FeII, 2374	0.16
140213A	1.19	34 ± 14	151	FeII, 2382	0.14

[a] VLT/X-shooter GRB spectrum is used to measure Δv_{90} for all GRB hosts in this table, except for GRB 090323 (Δv_{90} measuerement for the host of this GRB is presented in Arabsalmani et al., 2015a).

[b] The emission velocity width for the host of GRB 090323 is measured from OIII line instead of Hα line (see Krühler et al., 2015).

range. Further VLT imaging was obtained in the optical wavelength range for GRB 061110A and GRB 110818A with FORS2 (Appenzeller et al., 1998), as well as near-infrared imaging for GRBs 070318, 070328, 110818A, and 120714B with HAWK-I (Kissler-Patig et al., 2008). We also use multi-band imaging from GROND (Greiner et al., 2008) for the host galaxies of GRBs 070318A, 070328A, 111228A, 060204B, 060814A, 061202 and 120722A, which was obtained during a four night classical observing run in February 2015 awarded to S. Schulze.

SED fitting

The multi-color photometry of the hosts is fit with stellar population synthesis models as outlined in Krühler et al. (2011b). Very briefly, we use the Bruzual and Charlot (2003) models with a Chabrier (2003) initial mass function. The grid of galaxy templates contains different metallicities of the stellar component (0.2 to 1.0 of solar metallicity), e-folding timescales of the star-formation history (0.1 to 30 Gyr) and stellar population ages (10 Myr to 10 Gyr). The SED templates were attenuated following Calzetti et al. (2000) using values of E_{B-V} between 0 and 1 mag.

The fit itself is then performed with *Le Phare* (Arnouts et al., 1999; Ilbert et al., 2006), where physical parameters are reported as the median of the probability distribution over the full grid of all SED templates, with errorbars illustrating the 68 % confidence region for the respective parameter.

3.3.3 Velocity width measurements

For gas seen in emission, we adopt the measurements of Hα velocity dispersion ($\sigma_{H\alpha}$) from Krühler et al. (2015). To measure the velocity width of the neutral gas in absorption, we use Δv_{90} as a defined in Prochaska and Wolfe (1998), which is the velocity interval that contains 90% of the area under the apparent optical depth spectrum. In order to measure Δv_{90} one needs to carefully choose the metal lines that are suitable for such measurement. Such a line should neither be weak nor saturated, as these would lead to under and over estimation of the velocity width, respectively (Ledoux et al., 2006; Møller et al., 2013). Thus, we need to identify at least one low-ion metal profile in the GRB spectrum that is suitable for measuring the line-width. Identifying such a line for measuring the velocity width can be hard if the S/N of the spectrum is not high enough. In addition to this, we need to take care of the smearing effect caused by the resolution of the spectrograph. For this we use the method discussed by Arabsalmani et al. (2015a) showing that the intrinsic velocity width can be computed from

$$\Delta v_{90} = [\Delta v^2_{90,\mathrm{meas}} - (1.4 \times \mathrm{FWHM})^2]^{0.5}, \tag{3.1}$$

where $\Delta v_{90,\mathrm{meas}}$ is the measured value for the velocity width and FWHM is the corresponding Full Width Half Maximum of the instrument resolution. As discussed there, the correction can only be trusted if the resolution FWHM is not so large as to completely dominate over the intrinsic width of the line. In case the intrinsic width is equal to the resolution then the measured width will be a factor of $\approx \sqrt{2}$ larger, which is fully possible to correct for. We therefore choose the same conservative approach to only trust corrections if the measured width is less than 1.4 times the width after correction. In other words, we use the *r* parameter (introduced in Arabsalmani et al., 2015a),

$$r := \frac{\Delta v_{90,\mathrm{meas}} - \Delta v_{90}}{\Delta v_{90}} \tag{3.2}$$

and only consider systems correctable if $r \leq 0.4$ or equivalently if $\Delta v_{90} \gtrsim$ FWHM.

We have the X-shooter optical spectrum for 32 GRBs for which we can in principle measure the absorption velocity widths. Out of the 32 GRBs' spectra, we find suitable lines for measuring Δv_{90} for only 18 of the GRBs (see Tab. 3.2 and 3.3), of which the smearing effect of the instrument resolution does not allow Δv_{90} measurements for two of them (see the values of parameter r in the column 6 of Tab. 3.3). For the remaining 14 GRBs the S/N is too low to measure Δv_{90} . For 10 GRB hosts, we use the GRB spectrum published in the literature to measure Δv_{90} (the detail of these literature data are presented in Arabsalmani et al., 2015a).

3.4 Gas Kinematics

The absorption profiles in GRBs' spectra usually show several components or clouds tracing the velocity field in these high-z galaxies, similar to those of the Damped Lyman-α systems (DLAs) in the spectra of quasars. Each of these components has a broadening of a few km s^{-1}, but the total velocity width of the system is much larger, varying from a few tens of km s^{-1} to several hundreds km s^{-1}. GRB host galaxies display very high column densities of neutral Hydrogen, typically several times higher than the DLA threshold (see Fynbo et al., 2009). In systems with such high HI column densities the low-ion profiles trace the neutral hydrogen and hence the kinematic characteristics of these profile represent those of the neutral gas. The width of the low ion lines (e.g. Δv_{90}) is a measure of the spatially averaged velocity of neutral gas in these systems. Note that these absorption profiles trace only the gas in a narrow beam along the GRB sight-lines and therefore by using the width of these line we average only over the regions along the GRB sight-lines. Arabsalmani et al. (2015a) showed that the velocity width of the low-ion absorption lines correlate with the metallicity in GRB host galaxies (see also Prochaska et al., 2008). Such correlation was first found for the DLA systems in the sightlines of quasars (QSO-DLAs, Wolfe and Prochaska, 1998; Ledoux et al., 2006; Møller et al., 2013; Neeleman et al., 2013). This correlation points towards a mass-metallicity (MZ) relation for these high redshift systems (see section 3.4.4 for details). Absorption line velocity widths have been also studies in the light of galactic winds in both GRB host galaxies as well as in absorbers in sight-line of quasars (e.g. Chen et al., 2007; Barnes et al., 2011). The broadening of the bright emission lines (such as Hα line) too can be tracers of galactic winds. The kinematic features of Hα emission line is also used for studying the rotational and dispersion velocities of high redshift galaxies (see Glazebrook, 2013, and references therein).

In this section we investigate the kinematic characteristic of gas and their connections with other galaxy properties in GRB host galaxies. In emission, we use the velocity width of the Hα emission line and in absorption we use the width of low-ion lines as estimates of the spatially averaged velocity for ionised and neutral gas. We explore how the two velocities relate to each other, and to other galaxy properties.

3.4.1 Gas kinematics in absorption vs emission

We have velocity width measurements in both emission and absorption ($\sigma_{H\alpha}$ and Δv_{90} respectively) for 10 GRB host galaxies listed in Tab. 3.3. At first instance, we clearly see that the values of $\sigma_{H\alpha}$ are several times smaller than Δv_{90} values for all 10 GRB host galaxies. The larger values of absorption velocity widths should not come as a surprise. The Hα emission line trace the ionised gas in star forming regions of the galaxy. The low ion absorption lines trace the neutral gas along the GRB sight-line through the galaxy, probing gas in star forming regions where the GRB has

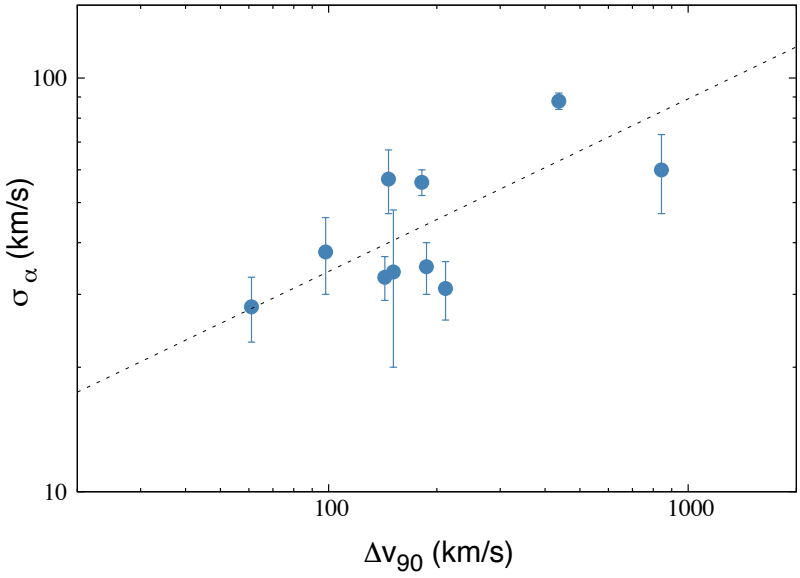

Figure 3.1: The velocity width of low ion absorption line (Δv_{90}) versus $\sigma_{H\alpha}$ for ten GRB host galaxies. The dotted line shows the best-fit line. Note that the best fit line is not obtained based on only the 10 data points (for details see section 3.4.2).

occurred, out to the outer most regions of the galaxy where the diffused gas is extended. In othere words, in absorption one detects the gas that is in a larger region and possibly as a consequence has a larger velocity variation compared to what is detected in emission. Moreover, in emission we are limited by brightness while the gas missed in emission can be detected in absorption. And finally, the contribution of galactic winds plays a role in larger absorption widths compared to those in emission. While rotation and random motions contribute to the broadening of both the profiles, galactic winds primarily affect the width of the absorption profiles. It is seen that the Hα emission line is insensitive to a large fraction of the outflow mass, while the ISM absorption lines trace the global galactic winds (e.g. Wood et al., 2015). The significantly larger values of Δv_{90} compared to $\sigma_{H\alpha}$ hints to the dominant contribution of outflows in absorption line widths.

More interestingly, we find the two velocity widths to correlate with each other (keeping in mind the small sample size; see the following section for the correlation parameters). Fig. 3.1 shows the 10 GRB host galaxies in the $\Delta v_{90} - \sigma_{H\alpha}$ plane. The relation between the two velocity widths points to the connection between the velocity widths and mass. In the following section we explore the existence of such relations directly using the stellar mass measurements of the GRB hosts in our sample.

3.4.2 Velocity width as a proxy of stellar mass

The connection between rotational velocity inferred from gas kinematic and luminosity properties was first introduced for nearby disk galaxies through the Tully-Fisher (TF) relation using the HI line width (Tully and Fisher, 1977). This was later on extended to higher redshifts using optical

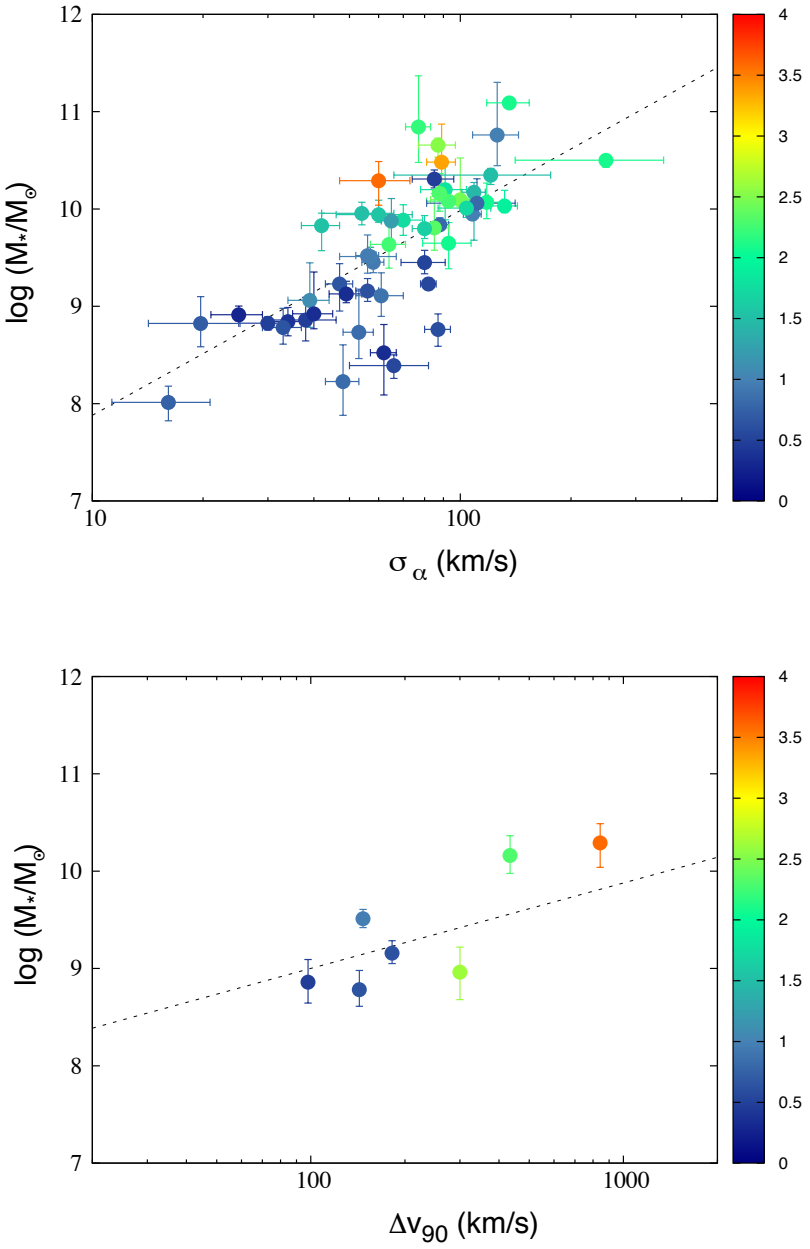

Figure 3.2: *Left panel*: Stellar mass versus velocity width of Hα emission line, $\sigma_{H\alpha}$, for 52 GRB host galaxies sampling a redshift range from $z = 0.28$ to $z = 3.58$. *Right panel*: Stellar mass versus velocity width of low-ion absorption lines for seven GRB host galaxies in our sample. The colour-bars indicate the redshifts of the GRB hosts. The dotted lines show the best fit lines obtained from the combination of data points in both plots and in fig. 3.1 (see section 3.4.2 for details).

lines instead of HI, and to the relation between stellar mass and rotational velocity known as the stellar mass TF relation. Initial investigations for high redshift galaxies found no correlation (Vogt et al., 1996; Simard and Pritchet, 1998), hinting to anomalous kinematics of high redshift galaxies. This was confirmed by studies of Lyman Break galaxies at $z \sim 3$ Pettini et al. (1998, 2001) as well as UV-selected galaxies at $z \sim 2$ Erb et al. (2006), from the integrated velocity width of nebular emission lines. However, with the help of resolved 2D kinematics, recent studies show that the stellar mass TF relation holds for high redshift galaxies, albeit with larger scatter compared to the local population (Puech et al., 2008, 2010; Miller et al., 2011; Glazebrook, 2013).

We have stellar mass and $\sigma_{H\alpha}$ measurements for 52 GRB hosts in our sample. The 52 galaxies cover a redshift range from $z = 0.28$ to $z = 3.58$ and are presented in the left panel of Fig 3.2. We clearly see a correlation between stellar mass and $\sigma_{H\alpha}$. The velocity width of the Hα emission line contains contribution from rotational velocity. But one should be careful not to erroneously interpret this width as an upper limit of the rotational velocity of the ionised gas in the galaxy. The full rotational velocity will only appear in the broadening of the Hα line if the observations are deep enough to pick up the faint emission from the full extend of the ionised gas in the star forming disk. Therefore we do not consider the $M_* - \sigma_{H\alpha}$ relation, shown in Fig. 3.2, as a stellar mass TF relation. However, the existence of such correlation for the GRB host sample with its large redshift range is interesting in the light of the TF relation.

To investigate this further, we explore the existence of a similar correlation between stellar mass and Δv_{90} . We have stellar mass measurements for 7 GRB hosts with Δv_{90} measurements (listed in Tab. 3.2). The right panel in Fig. 3.2 shows these seven galaxies. Despite the small sample size, we can clearly see a trend of increasing stellar mass with increasing Δv_{90} .

The two plots in Fig. 3.2 show that the velocity widths, measured from both absorption and emission methods, can be used as proxies of stellar mass. This also confirms the correlation between the two velocity widths shown in Fig. 3.1.

Clearly the three mentioned relations, $M_* - \sigma_{H\alpha}$, $M_* - \Delta v_{90}$, and $\sigma_{H\alpha} - \Delta v_{90}$, are not independent from each other. In order to quantitatively study these relations, we use the combination of all data points presented in Fig. 3.2 and Fig. 3.1, and obtain the correlation parameters for the three relations simultaneously. This also allows having trustworthy results for $M_* - \Delta v_{90}$ and $\sigma_{H\alpha} - \Delta v_{90}$ relations where the sample sizes are small. We present our method of finding the best fit correlation parameters using the combined data points in the Appendix.

We find the two velocity widths to relate to stellar mass as below:

$$M_* = 10^{5.8\pm0.4} \times \sigma_{H\alpha}^{2.1\pm0.2},$$
$$M_* = 10^{7.2\pm0.7} \times \Delta v_{90}^{0.9\pm0.3}, \tag{3.3}$$

with an intrinsic scatter of 0.4 and 0.3 dex in stellar mass for the two relations respectively. And consistently, the two velocity widths follow the following relation:

$$\sigma_{H\alpha} \propto \Delta v_{90}^{0.4\pm0.2}, \tag{3.4}$$

with an intrinsic scatter of 0.1 dex on $\sigma_{H\alpha}$. This appears to be much shallower a relation than expected if Δv_{90} is dominated by the velocity of infalling/outflowing gas. We discuss this issue in the following section.

3.4.3 Signatures of interacting systems

As we mentioned before, galactic winds are believed to have larger contributions to the velocity width of absorption profiles than that of Hα emission line. This is supported with the shallow slope in the $\sigma_{H\alpha}$-Δv_{90} relation presented in equation 3.4 (see section 3.4.2). However, this shallow slope, or equivalently, the steep slope of the $M_* - \Delta v_{90}$ relation is inconsistent with previous studies of galactic winds.

Several studies, based on both observations and simulation, have shown that in the general population of star-forming galaxies, the outflow velocity relates to the stellar mass as $v_{\rm out} \propto M_*^{\sim 0.2}$ (see e.g. Bordoloi et al., 2014; Karman et al., 2014; Chisholm et al., 2015, for observational study, and Barai et al., 2015, for studies based on simulation). Also, the velocity of the infalling gas is expected to be smaller that the escape velocity and hence it should relate to stellar mass as $v_{\rm infall} \propto M_*^{\lesssim 0.3}$. This together with equation 3.3 point towards significantly large contributions from effects other than outflow/infall gas in absorption velocity widths, specially ones with considerably large Δv_{90} . We speculate that such large absorption velocities are due to the effect of interacting systems and mergers. Indeed two of the GRB hosts in the sample with the largest Δv_{90} (GRBs 090323 and 121024) show signature of interaction in their absorption profiles. In both systems, the absorption profiles contain two main components separated by a few hundreds km s^{-1}in the velocity space, which could be due to two interacting galaxies (for GRBs 090323 see Savaglio et al., 2012, and for GRB 121024 see Friis et al., 2015a). Other evidences of interacting systems in GRB host galaxies have been previously discussed by Chary et al. (2002); Chen (2012); Arabsalmani et al. (2015b). Our results confirm the possible connection between interacting systems and GRB events.

Another possible explanation is that GRB host galaxies produce larger outflow velocities compared to the general population of star forming galaxies due to the compactness of their actively star forming regions. Lagos et al. (2013) through simulations show that the outflow velocity increases with the compactness of the star-forming region (see also Heckman et al., 2015). This could explain the large Δv_{90} in GRB host galaxies as they are shown to have high SFR densities (Kelly et al., 2014) compared to the general galaxy population. This scenario is also supported by the presence of compact regions with recent star-forming activities in GRB environments seen in nearby GRB hosts.

3.4.4 Velocity-metallicity correlation in both absorption and emission

Previous studies have shown that the velocity width of low ion absorption lines correlates linearly with the metallicity (inferred from absorption lines) for Damped Lyman-α galaxies (DLAs) in the sightlines of quasars (Ledoux et al., 2006; Møller et al., 2013). Moreover, Møller et al. (2013) found that the velocity-metallicity (VZ) correlation evolves linearly with redshift up to $z = 2.62$ and then remains unchanged for $z > 2.62$. This correlation is proposed to be representative of a MZ relation for this population of high redshift galaxies. Christensen et al. (2014) confirmed the consistency of the VZ correlation with the MZ relation for a sample of 12 DLA galaxies with measured stellar masses. Note that stellar mass measurements for these systems have proven to be extremely challenging (specially due to the presence of the bright background quasar).

Arabsalmani et al. (2015a) performed the same study for the DLA systems that are intrinsic to GRB host galaxies and concluded that not only a VZ correlation holds for GRB-DLAs, but also it is completely consistent with that of QSO-DLAs. They also found the VZ correlation of GRB-DLAs to obey the same redshift evolution as QSO-DLAs. Fig. 3.3 shows the VZ correlation for

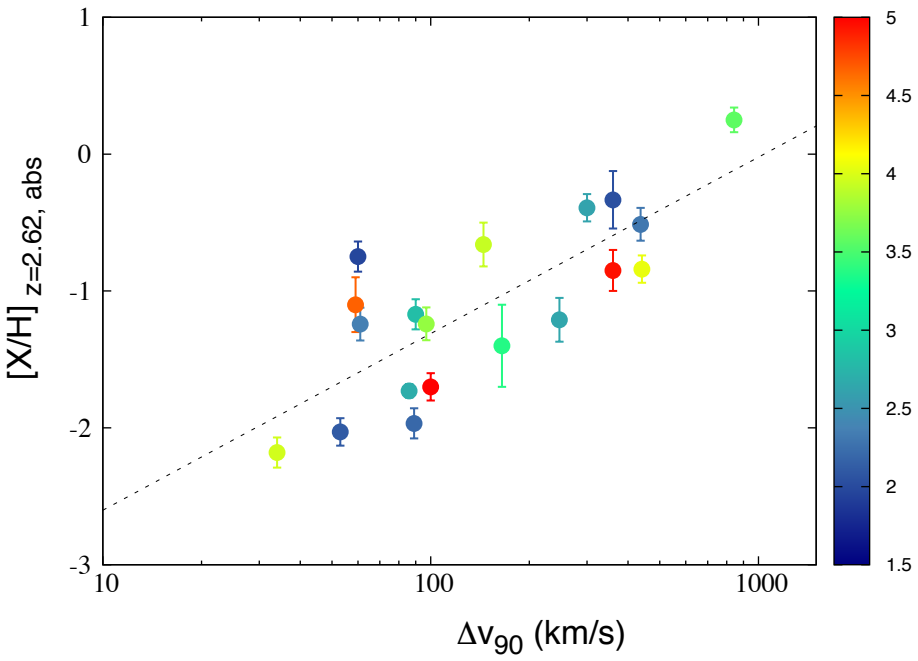

Figure 3.3: Correlation between absorption metallicity and Δv_{90} for 19 DLA syestem intrinsic to GRB host galaxies. The metallicities are corrected for redshift and are set to the corresponding values at $z = 2.62$. Note that from this redshift onwards the correlation seems to remain unchanged. The colourbar indicates the redshifts of the GRB hosts.

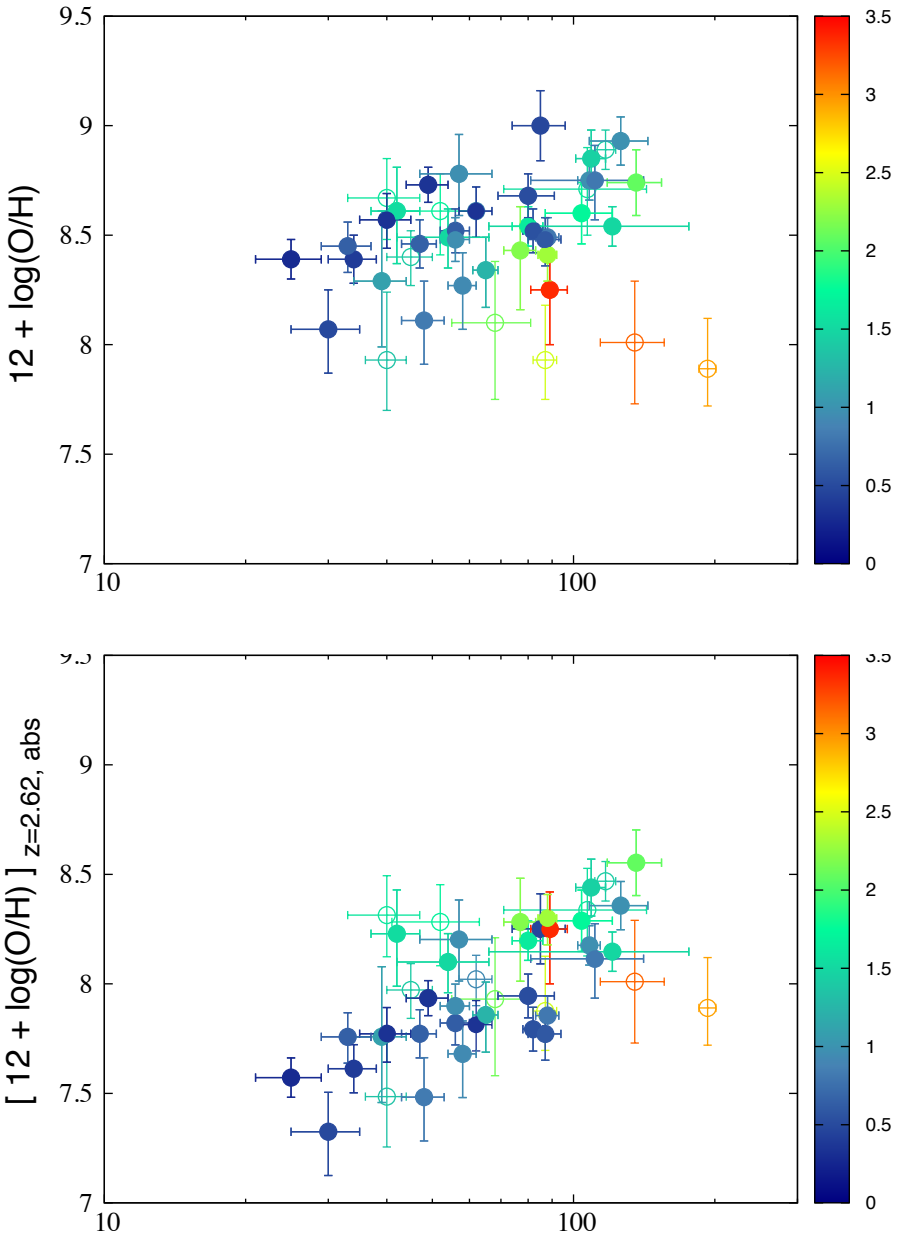

Figure 3.4: Cintinues in the next page

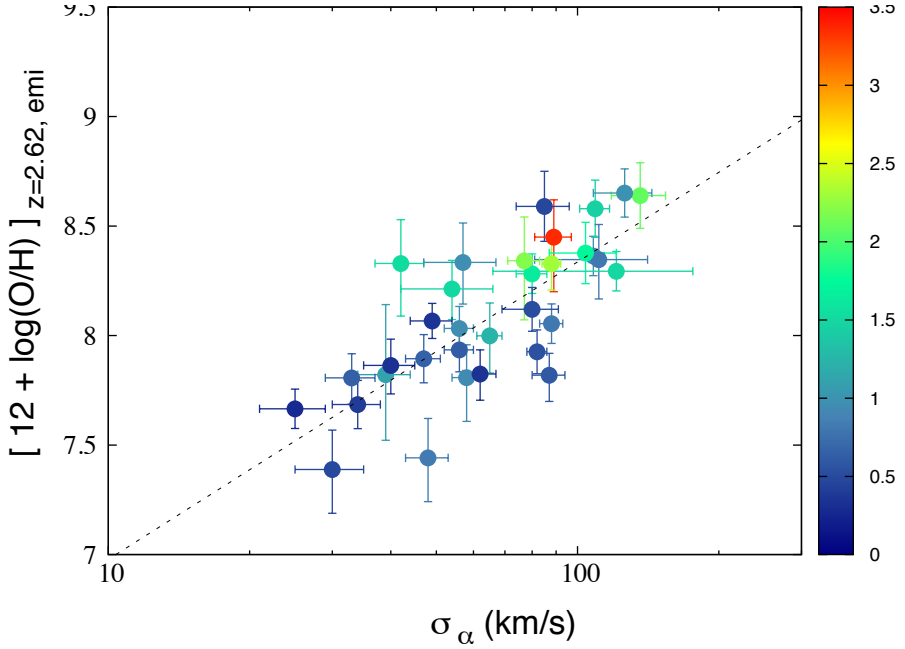

Figure 3.4: Emission metallicity versus $\sigma_{H\alpha}$. Note that y-axis is different in the three panels. In the *upper panel* y-axis shows the measured emission meatllicity, while in the other two panels it shows the emission metallicity corrected for redshift evolution and set to the corresponding value at $z = 2,62$ (metallicity measurements are shifted to the expected metallicities at redshift $z = 2.62$). In the *middle panel* the redshift correction of metallicities are based on the redshift evolution of absorption metallicities (Møller et al., 2013); In the *lower panel* the redshift corrections are based on the redshift evolution of emission metallicities obtained for general population of star forming galaxies (Maiolino et al., 2008). In *upper* and *middle panels*, the open circles show those GRB hosts in our sample for which we do not have the stellar mass measurements. We do not show these GRB hosts in the *lower panel* since redshift correction of metallicity measurements following the emission method requires the stellar mass measurements. In the *lower panel* the dotted line shows the best fit correlation line. The colour of each point indicates the redshift of the GRB host.

the 19 GRB host sample (16 of them presented in Arabsalmani et al., 2015a, , see Tab. 3.3 for the full sample). In this figure, we have followed Arabsalmani et al. (2015a) and have shifted the metallicities of the 19 hosts to the corresponding metallicties at $z = 2.62$ using the evolution of the VZ correlation.

Absorption metallicity measurements for GRB hosts have been restricted to $z \gtrsim 1.7$. Since GRBs are transient, the observations of their optical afterglows are usually limited to ground-based telescopes. This does not allow the detection of Lyman-α lines in the spectra of GRBs at $z \lesssim 1.7$ due to atmospheric cut-off. Therefore, at low redshifts the metallicity measurements are based on emission methods. It is not clear if the metallicity measurements from the two methods differ from each other. Hence, the next obvious step in our study is investigating the relation between the emission metallicity and the velocity width of gas obtained from emission lines.

We have 43 GRB hosts in our sample with measurements of both emission metallicity and velocity width, spanning a redshift range between $z = 0.28$ and $z = 3.36$. In the upper panel of Fig. 3.4 we present the 43 GRB host galaxies. At first instance one cannot see a clear correlation between the two quantities (see also Krühler et al., 2015, for the study of such correlation). But considering the large redshift range of the GRB hosts, it is important to to take the redshift evolution into account. In fact from the plot it is clear that hosts with higher redshift tend to be more scattered compared to the hosts at lower redshifts.

To further study this, we shift the metallicity measurements of all the hosts to a fixed redshift. At first, we follow the same approach used in absorption and shift all the metallicities to $z = 2.62$ using the evolution of the VZ correlation. The results are shown in the middle panel of Fig. 3.4. However, this is based on an assumption that the metallicities in absorption and emission are the same, which is not necessarily true. To have a fair analysis, we use the redshift evolution of the emission metallicities obtained for the general population of star forming galaxies (see section 3.5 which justifies using the MZ relation of general galaxy population). We adopt the evolution derived in Maiolino et al. (2008) for the MZ relation and shift the matellicities of the hosts to $z = 2.62$ based on the adopted metallicity evolution. This can only be done for those hosts with measured stellar mass, ie. 33 hosts oout of the 43, as the metallicity evolution discussed in Maiolino et al. (2008) is stellar mass dependent. Our results are shown in the lower panel of Fig. 3.4. Note that the 10 GRB hosts without stellar mass measurements which are not shown in the lower panel are presented with open circles in the upper and middle panels of Fig. 3.4. Clearly after redshift correction the emission line metallicity shows a tight correlation with the velocity width of the Hα line (see also Krühler et al., 2015, for studying the same correlation in different redshift bins).

We note that the VZ correlation has an intrinsic scatter of ~ 0.4 dex which is a about three times larger than the intrinsic scatter of the correlation between $\sigma_{\mathrm{H}\alpha}$ and emission metallicity.

3.5 Mass-metallicity relation

It appears that GRB-selected galaxies tend to have low metallicities (e.g. Graham and Fruchter, 2013; Levesque, 2014). Although, detection of several metal-rich and massive hosts put question mark on the low metallicity as a requirement for hosting GRBs (Savaglio et al., 2012; Elliott et al., 2013a; Perley et al., 2013a). In a recent study Perley et al. (2016e) show that low redshift ($z < 1.5$) GRB hosts are much fainter than the general star forming population, while at higher redshifts the differences are much more modest. This is consistent with the findings of Greiner et al. (2015) that the luminosity function of GRB hosts at $3 < z < 5$ is fully consistent with that of Lyman Break

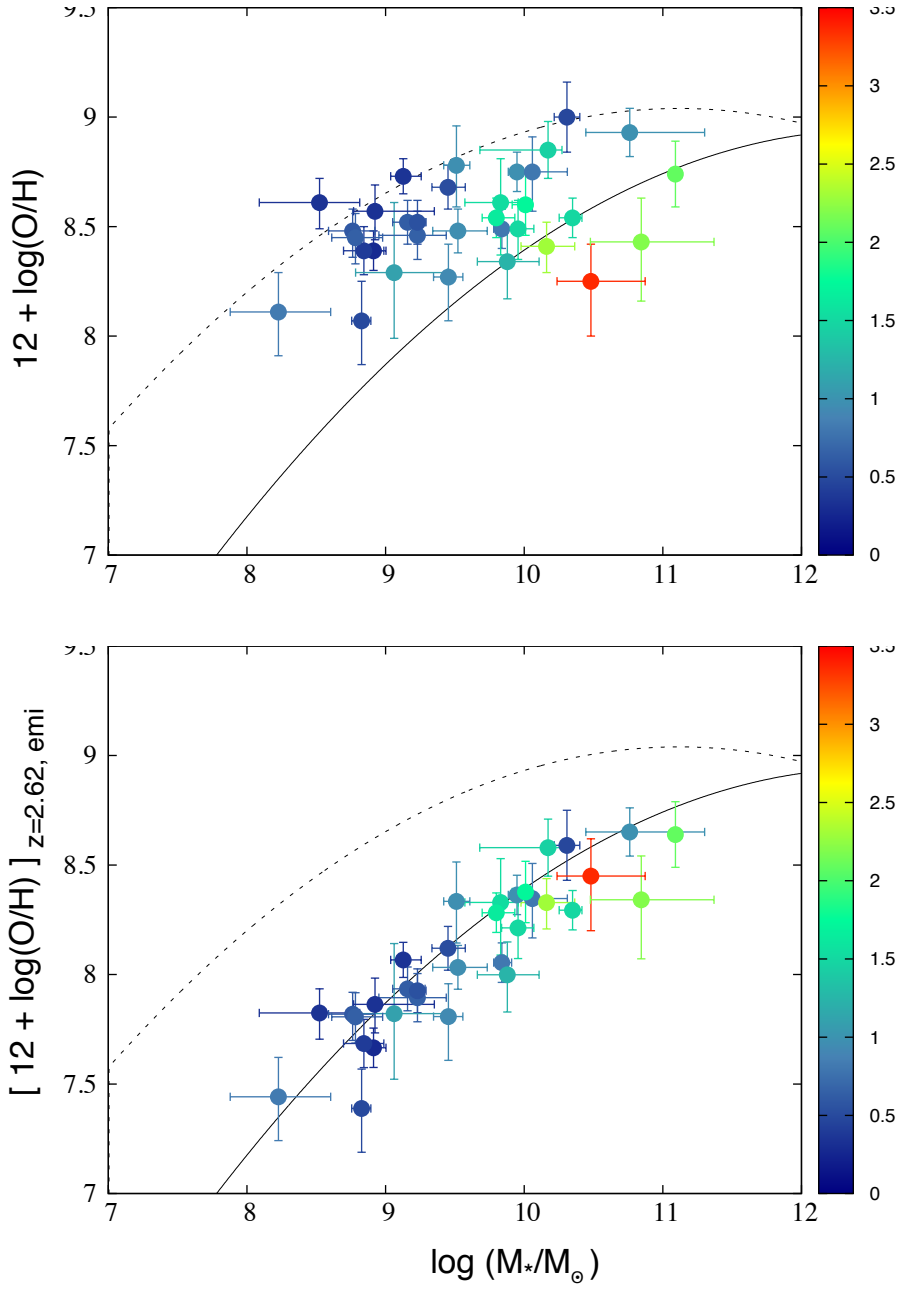

Figure 3.5: The MZ relation for 33 GRB hosts with measured stellar mass and metallicity. They y-axis in the *left panel* shows the measured emission metallicity while in the *right panel* it shows the emission metallicity corrected for redshift and set at $z = 2.62$ following the redshift evolution of metallicity from Maiolino et al. (2008). The dotted and solid lines in both panels show the MZ relation of general galaxy population at respectively $z = 0$ and $z = 2.62$ from Maiolino et al. (2008). The colourbar indicates the redshifts of the GRB hosts.

Galaxies, suggesting that GRBs provide a fair sampling of star formation process at higher redshifts.

The typical low mass and metallicity of GRB host galaxies (specifically in lower redshifts) should in principle put them on the lower mass end of the MZ relation of the general star-forming galaxy population (Tremonti et al., 2004), but still on the MZ relation. However, several studies have found GRB hosts to fall below the MZ relation towards lower metallicities (Stanek et al., 2006; Kewley et al., 2007; Levesque et al., 2010a; Mannucci et al., 2011). This means that GRBs occur in galaxies that have less metals for their stellar mass compared to other star-forming galaxies ie. GRB hosts are a distinct population os star-forming galaxies. Mannucci et al. (2011) showed that this is due to higher than average SFRs, as they found GRB hosts to be fully consistent with the fundamental metallicity relation (see also Kocevski and West, 2011). In contradiction to this, Graham and Fruchter (2013) concluded that the low-metallicity of GRB hosts are not primarily driven by the anti-correlation between star formation and metallicity, but rather must be overwhelmingly due to the astrophysics of the GRBs themselves.

We use the 33 GRB host galaxies in our sample with uniformly measured emission metallicity and stellar mass in order to study the MZ relation for our GRB sample. The left panel of Fig. 3.5 shows the mass-metallicity relation for our GRB host sample compared to the MZ relation of the general star-forming galaxy population at two different redshifts ($z = 0$ and $z = 2.62$) from Maiolino et al. (2008). We clearly see that the GRB hosts with higher redshifts have larger deviations from the local MZ relation. To investigate the effect of the redshift evolution, we plot our sample hosts with their metallicities shifted to $z = 2.62$ as explained in previous section, and compare them with the MZ relation at $z = 2.62$. Note that we are using the redshift evolution (from Maiolino et al., 2008) derived for the general population of star-forming galaxies which is independent from our GRB host sample.

The right panel of Fig. 3.5 shows the GRB host sample with metallicties set at $z = 2.62$, and it is here seen that GRB hosts are consistent with the MZ relation of the general star-forming galaxy population. In order to quantify this result we determine the offset between the GRB hosts and the relation from Maiolino et al. (2008), and find that the host sample falls 0.027 ± 0.011 dex below the relation. I.e. our GRB host sample follows, to within 2.5-sigma, the same MZ relation as emission selected galaxies in the same redshift and stellar mass range. To within 3-sigma GRB hosts at most have metallicities 0.06 dex lower. Note that the local MZ relation reported by Tremonti et al. (2004) has a 1-sigma scatter of 0.1 dex.

3.6 Metallicity in absorption vs. emission

It is not clear if the metallicity measurements from absorption and emission methods differ from each other as the methods of measuring the two metallicities are completely different. In emission, ratios of strong emission lines (like the ratio of Oxygen from OII or OIII lines to Hydrogen obtained from Hα or Hβ lines) are used to derive an Oxygen abundance 12+log(O/H) as a measure of the metal content. These methods require certain calibrations for strong-line diagnostics which are typically based on physical conditions in low-redshift galaxies (for detailed discussions see Maiolino et al., 2008; Steidel et al., 2014). In absorption the ratio of the column densities of metals to that of neutral Hydrogen provides a direct and accurate metallicity measurement. Unlike in emission, absorption metallicities do not suffer from calibration uncertainties and therefore are more reliable measurements of metal enrichment, especially at high redshifts. Though, absorption profiles provide information only on the narrow beam along the GRB sight-line. In addition, the emission and

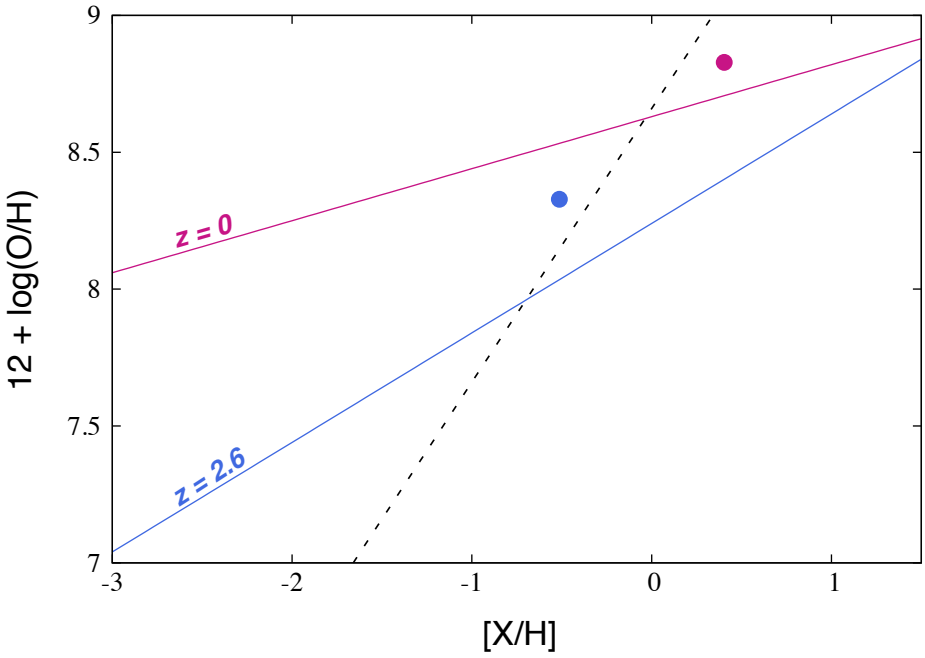

Figure 3.6: Emission metallicity versus absorption metallicity for GRB host galaxies. The solid lines present the inferred relation between the two metallicities at $z = 0$ and $z = 2.62$. The dotted black line shows the equality of the two metallicities. The circles represent GRB 121024 with its emission and absorption metalilcities set at $z = 0$ (red) and 2.62 (blue) following the emission and absorption metallicity evolutions respectively.

absorption profiles used in each method trace different phases of gas and in different regions of the galaxy. Therefore one could expect these metallicities not to be identical (see Krogager et al., 2013a; Fynbo et al., 2013, for both emission and absorption metallicty measurements of two QSO-DLAS). Note that the effect of the metallicity gradient in a galaxy is fair to be considered only if the measurements are based on the same methods and for the same phase of gas in the galaxy.

We have metallicity measurements from both absorption and emission methods for only one GRB host in our sample, GRB 121024, where the two measurements are consistent with each other (Friis et al., 2015a). However, we can use the information provided by gas kinematics to infer some information on the relation between the metallicities measured from the two methods. The correlation between velocity widths in absorption and emission, and their relationships with respectively absorption and emission metallicities leads to a relation between the two metallicities. In other words, for each GRB host with measured $\sigma_{\mathrm{H}\alpha}$, one could infer an absorption metallicity using the $\sigma_{\mathrm{H}\alpha}$-$\Delta v_{90}$ and [X/H]-Δv_{90} relations. In the same way, one could use the $\sigma_{\mathrm{H}\alpha}$-$\Delta v_{90}$ relation and the relation between $\sigma_{\mathrm{H}\alpha}$ and emission metallicity and infer an emission metallicity for each GRB host with measured Δv_{90} . We follow this method and obtain the relation between the measured and inferred metallicities for GRB host in our sample with measured emission or absorption metallicities. The results are presented in Fig. 3.6. The solid lines show the inferred relations at two different redshifts, while the dotted line is for the equal metallicity measurements from emission and absorption methods. We also show the metallicity measurements of GRB 121024 which has been corrected to the two redshifts.

The deviation between the two metallicities could be a result of the systematic difference between the two measurement methods. But let us ignore the fact that the two measurement methods are fundamentally different and try to see if the results shown in Fig. 3.6 could be interpreted based on only the difference between the gas phases that each method probes. At $z = 0$ the absorption metallicity appears to be lower that the metallicity obtained from emission, but up to a certain metallicity around solar. The lower values for absorption metallicities could be expected as absorption methods prob the metal enrichment of gas extended to the outer most regions of the galaxy. On the other hand, the metallicity obtained from emission methods measures the metal enrichment of the ionised gas in the central regions of the galaxy, where the star-forming activity is expected to have enriched the metal content of the gas. The same trend is seen at higher redshifts, though with a lower value for the turn-over metallicity. Another interesting point to note in Fig. 3.6 is the general decrease of deviation between the two metallicities with increasing redshift. This too may not be surprising as at higher redshifts galaxies are in an earlier evolutionary state with less metal enrichments, and have more uniform properties.

3.7 Summary

GRB host galaxies provide the unique opportunity of simultaneously studying their different gas phases, using both GRBs' and hosts' spectra. This includes investigating the kinematics characteristics of the gas, through both absorption and emission methods, which provides invaluable information on the structure of galaxies and processes involved in their formation and evolution. In this paper we connected the galactic properties of GRB hosts inferred from absorption methods to those from emission methods. To this end, we put together a large sample of GRB hosts with uniformly measured properties. These included stellar mass, metallicity, and spatially averaged velocity of gas inferred from absorption and emission.

We showed that the spatially averaged velocity of gas can be used as a proxy of stellar mass. This should not be surprising as all the components contributing to the velocity width of both absorption and emission lines must be controlled by the gravitational potential in the galaxy. We find the velocity width of low-ion absorption lines to be several times larger than that of emission lines in GRB hosts. This hints to the significant contribution of galactic winds in ISM absorption lines. If galactic winds dominate the velocity width of ISM absorption lines, they appear to have much larger velocities in GRB host galaxies compared to the general star-forming galaxy population with similar stellar masses. This could be a result of the high SFR densities in GRB hosts. Interacting systems could also be behind such large velocity widths. In fact the possible connection between mergers and GRB event have been previously pointed out in several cases (Chary et al., 2002; Chen, 2012; Arabsalmani et al., 2015b).

The correlation between velocity width and metallicity, both obtained from ISM absorption lines, is established for DLA systems and Arabsalmani et al. (2015a) showed the same correlation to hold for GRB hosts. We here investigated if similar relationship exist between the same properties but inferred from emission methods. Indeed we found the emission metallicity to correlate with the velocity width of the Hα emission line. We use the velocity-metallicity correlations to explore the connection between the metallicity measurements from absorption and emission methods. We speculate that the two metallicities are not identical, with an increase in the deviation between them with a decrease in redshift.

Finally, we studied the mass-metallicity relation for our GRB host sample. By considering the redshift evolution of the MZ relation, we found GRB hosts to obey the MZ relation of the general star-forming galaxy population.

Acknowledgments

M. A. thanks Roberto Maiolino, Richard Ellis, Claudia Lagos, Bernd Husemann, and Sambit Roychowdhury for helpful discussions. The research leading to these results has received funding from the European Research Council under the European Union's Seventh Framework Program (FP7/2007-2013)/ERC Grant agreement no. EGGS-278202.

APPENDIX: Correlation parameters

A. Intrinsic scatter

Throughout this paper we investigate the scaling relations between the GRB hosts properties in the form of linear correlations. We explain here the method used for obtaining the correlation parameters.

We basically need to find out the linear correlation between the two measurable quantities, y and x, in the form of $y = a + bx$, using a data set containing N data points with measured values of x_i and y_i for the ith point. In some cases, the measurement errors of data points are non-symmetric and a Monte Carlo Method should be used to obtain the best fit parameters for the correlation. However, investigating the effect of the asymmetry of the error-bars, we find it to be ignorable. One reason for this is the negligible asymmetry of the error-bars and the other is the dominating effect of the intrinsic scatter of the correlations, $\sigma_{\rm scatter}$ (discussed below), compared to the measurement error-bars. Therefore, we use the standard least square method, assuming the measurement errors of each

point to be the average of the lower and upper measurement errors of that point. But of course we include the intrinsic scatter of the correlation as a free parameter in the
rmchi^2 by adding it up to the measurement error of each point in the quadratic form (see Møller et al., 2013). The χ^2 then will be

$$\chi^2 = \sum_{i=1}^{N} \frac{(a + bx_i - y_i)^2}{\sigma_{y,i}^2 + b^2\sigma_{x,i}^2 + \sigma_{scatter}^2}, \tag{3.5}$$

where $\sigma_{x,i}$ and $\sigma_{y,i}$ are the average of the lower and upper measurement errors on x_i and y_i respectively, and a, b, and $\sigma_{scatter}$ are the three free parameters.

B. The three correlations

The three correlations between M_*, $\sigma_{H\alpha}$, and Δv_{90} are not independent from each other and hence they get defined by four parameters:

$$\begin{aligned} M_* &= a + b\,\sigma_{H\alpha}, \\ M_* &= c + d\,\Delta v_{90}. \end{aligned} \tag{3.6}$$

The two correlations in equation 3.6 automatically define the correlation between $\sigma_{H\alpha}$ and Δv_{90}. In order to find the best fits for the four parameters we use all the three sets of data points: n_i pairs of $(M_*, \sigma_{H\alpha})$, n_j pairs of $(M_*, \Delta v_{90})$, and n_k pairs of $(\sigma_{H\alpha} - \Delta v_{90})$. Some of the data points are shared between the three sets. In order to do a χ^2 minimization that takes into account all three correlations and the sharing of data points,we solve a matrix optimization as follows. We write the three correlations for all the data points:

$$\begin{aligned} a + b\,\sigma_{H\alpha,i} &= M_{*,i}, \\ c + d\,\Delta v_{90,j} &= M_{*,j}, \\ a + b\,\sigma_{H\alpha,k} - c - d\,\Delta v_{90,k} &= 0, \end{aligned} \tag{3.7}$$

where $i = 1, \ldots, n_i$, $j = n_i + 1, ..., n_i + n_j$, and $k = n_j + 1, ..., n_j + n_k$. To solve the equations, we write them as a matrix equation: A . p = M, where A is the matrix

$$\begin{bmatrix} 1 & \sigma_{H\alpha,i} & 0 & 0 \\ 0 & 0 & 1 & \Delta v_{90,k} \\ 1 & \sigma_{H\alpha,k} & -1 & -\Delta v_{90,k} \end{bmatrix}$$

and p is the vector (a,b,c,d), and M is the vector $(M_{*,i}, M_{*,j}, 0...0)$ with the last k elements being 0. The dimensions of matrix A, vector p, and vector M are 4.(i+j+k), 4, and i+j+k respectively.

In order to make this a χ^2 optimization, one has to to multiply both sides of each equation with the appropriate weights before solving it. The weights are $[\sigma_{M_{*,i}}^2 + \sigma_{scatter,\,M_* - \sigma_{H\alpha}}^2]^{-0.5}$ for equations 1 to i, $[\sigma_{M_{*,k}}^2 + \sigma_{scatter,\,M_* - \Delta v_{90}}^2]^{-0.5}$ for equation n_{i+1} to $n_i + n_j$, and $[(b\,\sigma_{M_{*,k}})^2 + \sigma_{scatter,\,\sigma_{H\alpha} - \Delta v_{90}}^2]^{-0.5}$ for equation n_{j+1} to $n_j + n_k$. With these weights, minimizing $|A.p - M|^2$ is equivalent to the χ^2 minimization.

If a point appears in two of the data sets, the weights have to be reduced in order to avoid counting that measurement twice. Though we find this not to change our results significantly. Finally, we use numpy.linalg.lstsq routine to solve the matrix equation.

Chapter 4

First HI 21 cm mapping of a GRB host

This chapter containes the folllowing paper:
"First measurement of H I 21 cm emission from a GRB host galaxy indicates a post-merger system"
Arabsalmani, Maryam; Roychowdhury, Sambit; Zwaan, Martin A.; Kanekar, Nissim; Michalowski, Michal J.
Monthly Notices of the Royal Astronomical Society: Letters, Volume 454, Issue 1, p.L51-L55

4.1 Abstract

We report the detection and mapping of atomic hydrogen in HI 21 cm emission from ESO 184-G82, the host galaxy of the gamma ray burst 980425. This is the first instance where HI in emission has been detected from a galaxy hosting a gamma ray burst. ESO 184-G82 is an isolated galaxy and contains a Wolf-Rayet region close to the location of the gamma ray burst and the associated supernova, SN 1998bw. This is one of the most luminous HII regions identified in the local Universe, with a very high inferred density of star formation. The HI 21 cm observations reveal a high HI mass for the galaxy, twice as large as the stellar mass. The spatial and velocity distribution of the HI 21 cm emission reveals a disturbed rotating gas disk, which suggests that the galaxy has undergone a recent minor merger that disrupted its rotation. We find that the Wolf-Rayet region and the gamma ray burst are both located in the highest HI column density region of the galaxy. We speculate that the merger event has resulted in shock compression of the gas, triggering extreme star formation activity, and resulting in the formation of both the Wolf-Rayet region and the gamma ray burst. The high HI column density environment of the GRB is consistent with the high HI column densities seen in absorption in the host galaxies of high redshift gamma ray bursts.

4.2 Introduction

Long-duration gamma ray bursts (GRBs) are believed to originate in the death of short-lived massive stars and hence are expected to be located in regions with high star formation (Bloom et al., 2002; Fruchter et al., 2006). This picture is in good agreement with the high star formation rates (SFRs) typically observed in galaxies hosting GRBs. While determining the stellar mass and the

SFR of GRB host galaxies at high redshifts remains challenging even with today's 10m-class telescopes, such estimates have been possible for a fair number of GRB hosts out to $z \sim 3$ (e.g. Castro Cerón et al., 2010) This remarkable recent progress in studies of GRB host galaxies has not been mirrored in emission studies of their neutral gas, which is the fuel for star formation. Such studies are critical in order to understand the interplay between interstellar medium (ISM) conditions and star formation that gives rise to the GRB progenitors. The neutral atomic hydrogen in several GRB host galaxies at z $\gtrsim$ 2 has been detected in absorption, yielding estimates of the HI column density, N(HI), and gas kinematics (e.g. Fynbo et al., 2009; Prochaska et al., 2008; Arabsalmani et al., 2015a). Indeed, molecular hydrogen has also been detected in absorption in three GRB hosts (Prochaska et al., 2009; Krühler et al., 2013; D'Elia et al., 2014). However, these absorption features only trace the gas along the narrow beam in the GRB sightline and carry little information on the whole galaxy. Understanding the nature of GRB host galaxies and the conditions for GRB formation critically requires emission studies in the atomic and molecular gas. Although CO emission has recently been detected in three galaxies hosting GRBs (Hatsukade et al., 2014; Stanway et al., 2015), uncertainties in the CO-to-H_2 conversion factor (e.g. Bolatto et al., 2013) imply large uncertainties in the inferred molecular gas mass. Unfortunately, the sensitivity of today's radio telescopes limits HI 21 cm emission studies to relatively low redshifts, $z \lesssim 0.2$ (e.g. Catinella and Cortese, 2015). To date, the information on the HI mass, which is likely to be the dominant part of the gas content of such galaxies, does not exist for any GRB host. The HI 21 cm emission line would allow a direct measurement of the total HI mass, as well as detailed studies of the spatial distribution and the kinematics of the atomic gas. Combining this information on the HI content, distribution and kinematics, with information on the star formation and the stellar mass, and, finally, with information on the molecular gas, would enable us to have a comprehensive picture of galaxies hosting GRBs.

The galaxy ESO 184-G82, the host of the closest known GRB (at $z = 0.0087$; Foley et al., 2006) and one of the first GRBs to be associated with a supernova (SN 1998bw, Galama et al., 1998), is one of the few GRB hosts where it is possible to carry out spatially-resolved spectroscopy and photometry. It hence offers the unique opportunity of a detailed study of the close environment of a GRB. The GRB occurred in one of the several high surface brightness star-forming regions of the galaxy (Fynbo et al., 2000). The host galaxy has a high specific star formation rate (SFR per unit stellar mass, sSFR); in particular, it contains a Wolf-Rayet (W-R) region with extremely high ongoing star formation, close to the GRB location. The cause of this high star formation has been an unsolved puzzle over the last decade. In this Letter, we present evidence for the possible cause of the extreme star formation properties of ESO 184-G82, via a study of the HI 21 cm line emission from this galaxy. This is the first time that HI has been detected in emission from a GRB host galaxy (see also Michalowski et al., in press).

4.3 Observations, data analysis and results

We initially obtained archival Australia Telescope Compact Array (ATCA) data covering the redshifted HI 21 cm line from the GRB 980425 host galaxy (project code: C2700). These observations were carried out on 2012 April 12 in the 1.5B configuration, with a total on-source time of 8 hours, using the Compact Array Broadband Backend with a bandwidth of 3.5 MHz. The ATCA data were analysed using "classic" AIPS, following standard procedures, and yielded a detection of HI 21 cm emission from the GRB host galaxy. Since the ATCA has only six antennas, and hence relatively

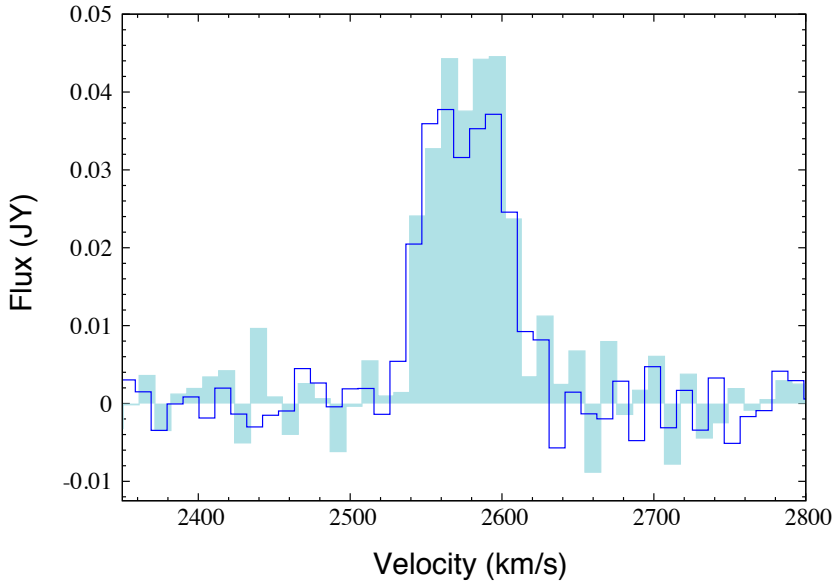

Figure 4.1: HI 21cm emission profile of the galaxy ESO 184-G82, as measured with the GMRT (shaded histogram) and the ATCA (bold line).

poor U-V coverage in a single configuration, we followed up this detection with mapping observations with the Giant Metrewave Radio Telescope (GMRT). The GMRT HI 21 cm observations of the GRB host galaxy were carried out on 2015 April 3 and 5, using a bandwidth of 4 MHz, centred at the redshifted HI 21 cm line frequency of 1410.33 MHz and sub-divided into 512 channels. The total on-source time was 2.6 hours, with observations of the standard calibrators 3C48 and 2005-489 used to calibrate the flux density scale, the system bandpass and the system gain. The initial data editing and calibration of the GMRT data were carried out in the FLAGCAL software package (Prasad and Chengalur, 2012), with the remaining analysis done in AIPS, again following standard procedures. After Hanning smoothing, re-sampling, and a detailed self-calibration process, the radio continuum was subtracted from the calibrated visibilities using the tasks UVSUB and UVLIN, and the residual visibilities mapped with different U-V tapers to produce spectral cubes at different spatial and velocity resolutions. The velocity resolution was varied in order to improve the statistical significance of the detected HI 21 cm emission in independent velocity channels. The properties of the spectral cubes that will be used here are listed in Table 4.1.

Fig. 4.1 shows the HI 21 cm emission spectra obtained from the ATCA and GMRT spectral cubes, at, respectively, spatial resolutions of $34.5'' \times 21.4''$ and $36'' \times 22''$ and velocity resolutions of 10.5 km s^{-1} for both datasets. Note that the spectra show the integrated flux density over the entire spatial extent of the detected HI 21 cm emission. We have checked that all of the source flux density is recovered at this resolution; further lowering the resolution does not increase the total flux density. The ATCA and GMRT spectra are seen to be in agreement; since the GMRT data have far better U-V coverage than the ATCA data, and also yield a significantly better angular resolution, all the following results and discussion will be based on the GMRT data. We obtain an integrated HI 21 cm line flux density of 3.0 ± 0.2 Jy km s^{-1} from the GMRT spectrum of Fig. 4.1. Using a source

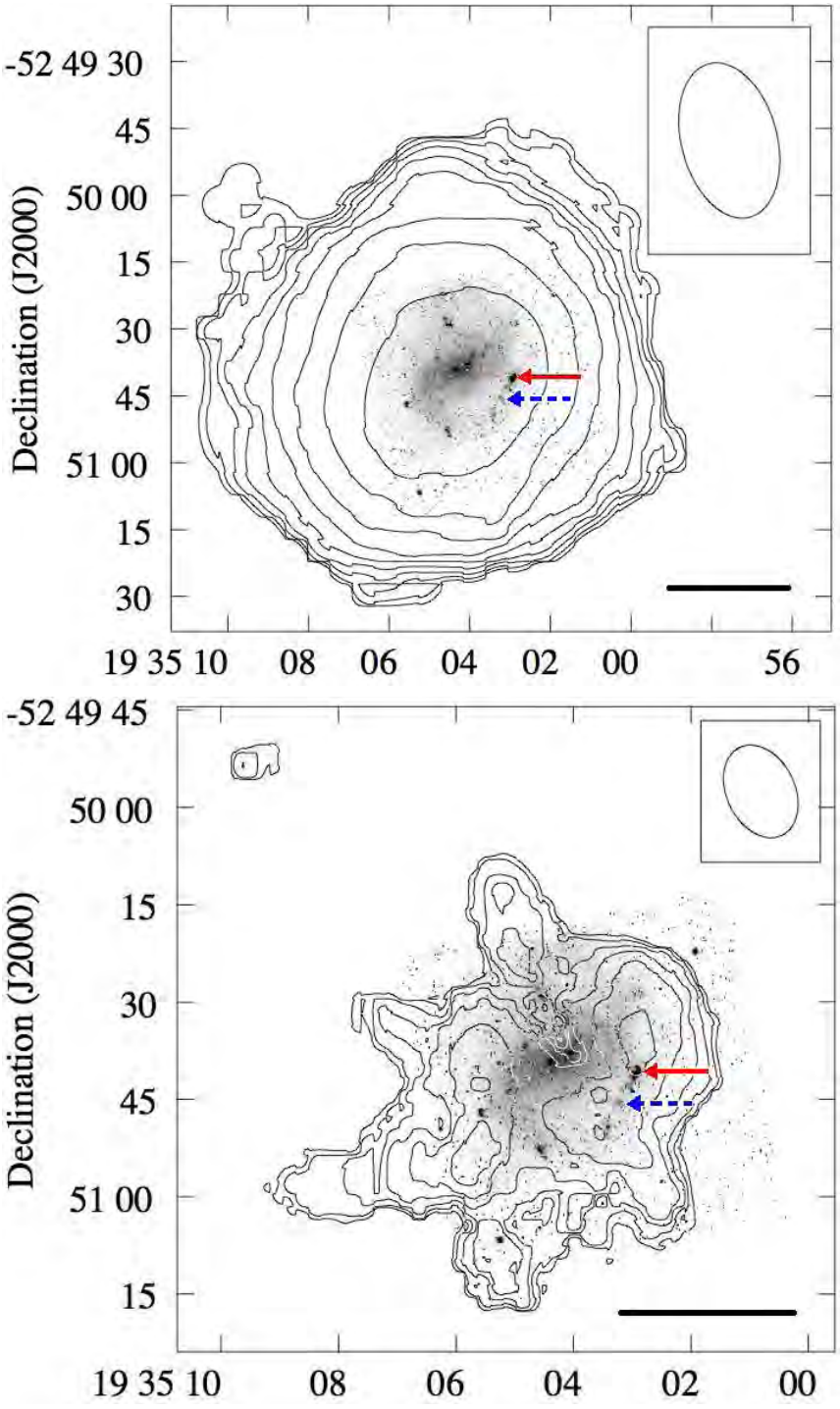

Figure 4.2: Cintinues in the next page

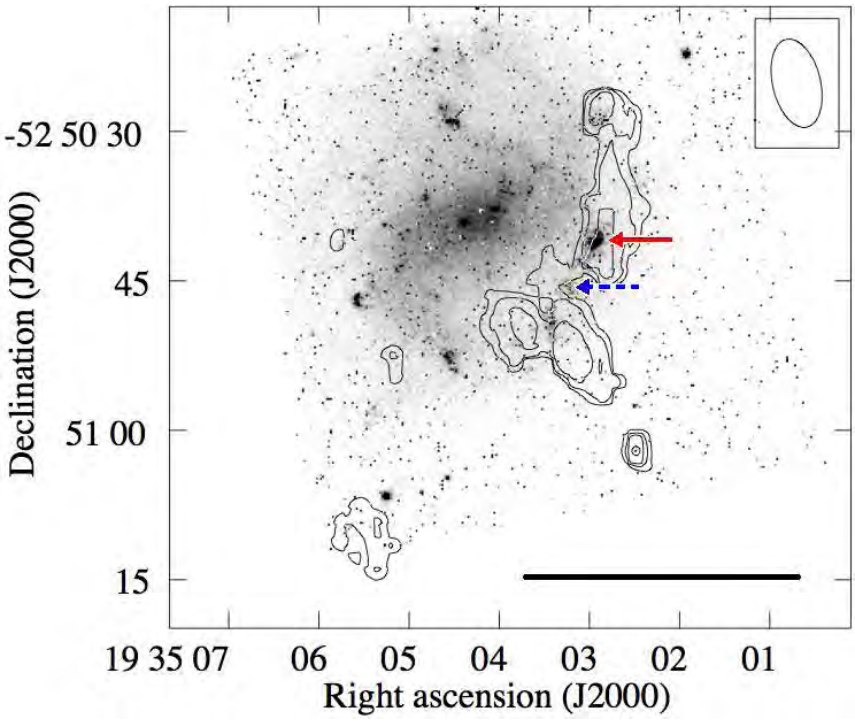

Figure 4.2: HI column density maps (in contours) overlaid on an HST image (greyscale) of ESO 184-G82. The resolutions are $36'' \times 22''$ (top), $15'' \times 11''$ (middle), and $9'' \times 5''$ (bottom), with outermost (3 σ) contours of 5×10^{19} cm^{-2}, 2×10^{20} cm^{-2}, and 5×10^{20} cm^{-2}, respectively, and subsequent contours at N(HI) intervals of $\sqrt{2}$. For reference, the solid line at the bottom right of each panel indicates a scale of 5 kpc at the distance of the galaxy. The dashed blue and solid red arrows mark the GRB location and the W-R region, respectively.

Table 4.1: Parameters of the GMRT HI data cubes

Synthesized Beam (arcs×arcs)	Channel width (km s^{-1})	Noise in line-free channel (mJy Bm^{-1})
35.6×21.5	10.5 , 7.0	1.5 , 1.8
24.6×18.1	7.0	1.6
15.0×10.5	7.0	1.3
9.1× 4.8	7.0	1.0

distance of 37.7 Mpc (assuming a flat Λ-cold dark matter cosmology with H_0 = 69.6 km $s^{-1}$$Mpc^{-1}$ and Ω_m = 0.3), this yields an HI mass of (1.00 ± 0.08) × 10^9 $M_\odot$. Using the coarsest resolution HI 21 cm map we measure the inclination angle of the HI disk to be between 42° and 50° for an intrinsic axial ratio varying between 0.1 and 0.5. This range in inclination is consistent with the inclination angle of the optical disk, $i = 50°$ (Christensen et al., 2008). The velocity width between half-power points is $W_{50} = 65$ km s^{-1}. Correcting this for the inclination angle of $i = 50°$ yields a velocity width of $W^i_{50} = 85$ km s^{-1}. The AIPS task MOMNT was used to make HI column density maps of the field, using the 7 km s^{-1} resolution data cubes, at different spatial resolutions. Fig. 4.2 shows three of these maps (in contours) overlaid on an Hubble Space Telescope (HST) optical image (with the MIRVIS filter, centred at 5737.453; in greyscale). The top panel shows that the HI disk of the galaxy is more extended than the optical disk, a feature common in sub-L_*, gas-rich galaxies (e.g. Begum et al., 2008). The broad peak of the HI distribution at the coarsest resolutions corresponds to the location of the optical galaxy. The intermediate-resolution (15″× 11″) map, in the middle panel of Fig. 4.2, shows an arc of dense gas roughly coincident with the southern spiral arm of the galaxy. The W-R region mentioned above arises in one of the denser HI regions. There appears to be a lack of high-N(HI) gas at the centre of the galaxy, as well as towards the north-east of the optical disk. An apparently isolated high-N(HI) knot is visible at the extreme north-east end of the HI disk; its signature is clear in even the low resolution map. The highest resolution (9″× 5″) map, shown in the bottom panel of Fig. 4.2, is sensitive to only the highest HI column densities. This image confirms that both the W-R region and the GRB location are coincident with the highest N(HI) regions of the galaxy. Indeed, when inspecting the N(HI) maps at higher resolution, we notice a piling up of gas on the western side of the galaxy.

To fully understand the nature of the HI distribution in the galaxy, one needs to study the velocity distribution of the gas. The intensity-weighted HI 21 cm velocity field of the full HI disk, displayed in contours in Fig. 4.3 at a low resolution (36″× 22″), shows the presence of an overall gradient from the south-east to the north-west. However, even at this coarse resolution, there are multiple features incompatible with an origin in a regularly rotating disk galaxy. For a more detailed study of the velocity field, we use the data cube of resolution 25″× 18″, which allows us to spatially distinguish different HI emission regions, while retaining some sensitivity to low N(HI) gas. The HI 21 cm velocity field at this resolution is shown in greyscale in Fig. 4.3. The rotation of the neutral gas around the galaxy's optical centre is evident at this resolution; the velocity field traced by H-α emission in a limited region around the optical centre (Christensen et al., 2008) is consistent with it.

Fig. 4.4 shows the HI 21 cm emission from individual (7 km s^{-1}) velocity channels of the 25″× 18″ data cube. A number of HI 21 cm emission regions with velocities unrelated to the main

rotational gradient of the HI distribution are easily identified in the channel maps. Table 4.2 lists the locations of four such regions, conservatively identified in at least two velocity channels. The previously mentioned isolated knot of high-N(HI) gas is also identified and marked (region c). For each region, we have identified the velocity range over which the "offset" HI 21 cm emission is detected (listed in column 3 of Table 4.2). We use the fluxes from the "offset" regions in velocity channels where they are detected to estimate their HI masses. Column 4 of the table lists the mass fraction of each region (relative to the total HI mass of ESO 184-G2, measured at the same spatial resolution). These estimates provide a conservative lower limit to the total amount of disturbed gas in the galaxy, as they only include the mass of regions that are spatially distinct from the gas undergoing regular rotation and also only include regions identified in more than one velocity channel. Summing the mass fractions of the four kinematically disturbed regions, we find that at least 21% of the HI in ESO 184-G2 appears to not be following the rotation of the main gas disk. The largest HI region with disturbed kinematics has $\sim$12% of the total HI mass of the galaxy, and is located close to the south-eastern peak of the main body of the rotating gas. To clearly discern the presence of the large amount of disturbed HI close to the rotating disk, we show a position-velocity cut along the major axis of the galaxy in Fig. 4.5. This kinematically-disturbed HI is centred at an angular offset of $-30''$ from the galaxy centre and is clearly separate from the gradient representing the main rotating gas in ESO 184-G82.

4.4 Discussion and conclusions

The GRB host galaxy ESO 184-G82, a barred spiral galaxy, is a low-luminosity object with $L_B = 0.05L_B{}^*$, but is clearly undergoing active star formation (Fynbo et al., 2000; Sollerman et al., 2005). The overall SFR and dust properties of the galaxy are consistent with those of local dwarf galaxies (Michałowski et al., 2009). The galaxy has an oxygen abundance of 0.41 solar (Sollerman et al., 2005; Christensen et al., 2008) and a stellar mass of 4.8×10^8 $M_\odot$ (Michałowski et al., 2014). The HST image of the galaxy shows that its optical appearance is dominated by several high surface brightness star-forming regions, especially in the southern spiral arm of the galaxy. The GRB occurred in one of these HII regions, whose properties (e.g. SFR, reddening, stellar mass) are similar to those of other HII regions in the galaxy (Christensen et al., 2008).

We find ESO 184-G82 to be a gas-rich galaxy, with an HI mass $\sim$ 2.1 times its stellar mass, which is consistent with the above studies showing ongoing star formation. Its SFR estimates, determined from H-α and U-V emission, lie in the range 0.25 - 0.45 $M_\odot yr^{-1}$(Sollerman et al., 2005; Christensen et al., 2008; Michałowski et al., 2009; Castro Cerón et al., 2010). The HI mass and SFR of ESO 184-G82 are consistent with the relation between the two quantities in nearby, HI-selected galaxies (Doyle and Drinkwater, 2006). Similarly, the sum of the HI and the stellar mass, and the HI 21 cm velocity width are consistent with the baryonic Tully-Fisher relation determined for nearby galaxies (Zaritsky et al., 2014). Thus, ESO 184-G82 appears to be a fairly typical star-forming galaxy, based on its global HI properties.

However, the unique feature of ESO 184-G82 is a region with a strong signature of W-R stars located at a projected distance of $\sim$ 800 pc from the GRB location (Hammer et al., 2006). This very young (a few Myr) star-forming region is possibly going through its first episode of star formation (Le Floc'h et al., 2012), with sSFR $\sim$ 11.3 Gyr^{-1} (using the SFR estimate from the Hα emission; Christensen et al., 2008), which is more than an order of magnitude larger than the overall sSFR of the galaxy. This W-R region, many of whose properties are similar to those of high-redshift

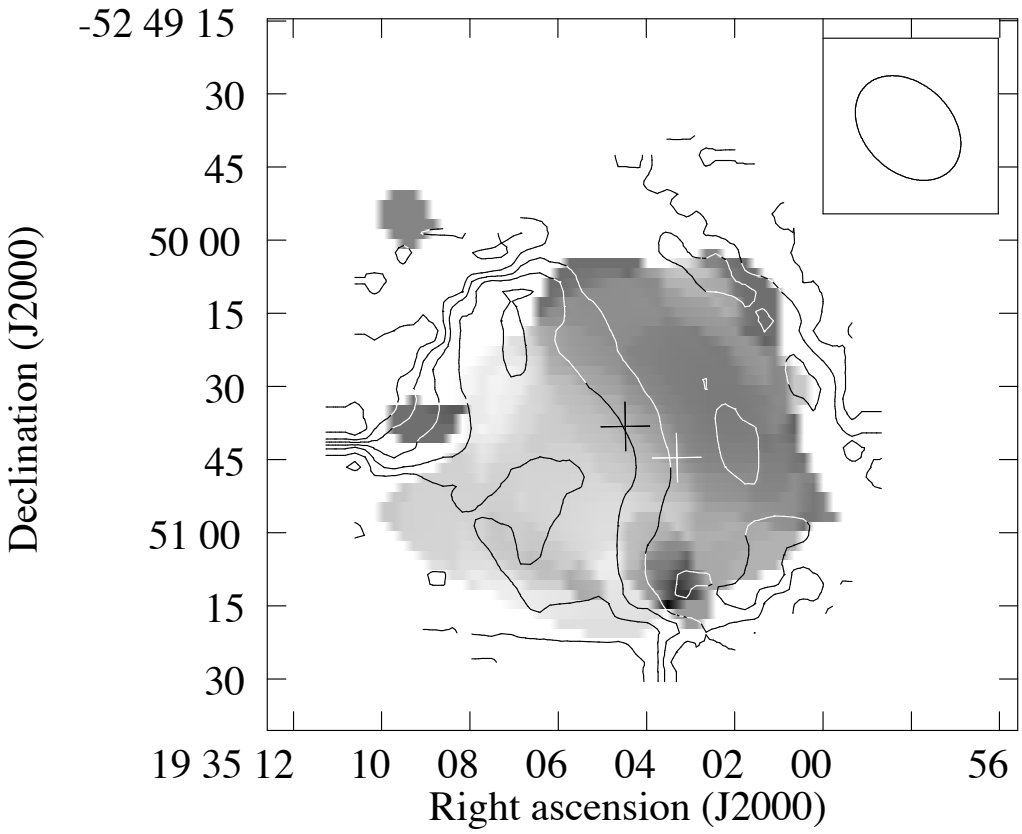

Figure 4.3: The HI 21 cm velocity field of ESO 184-G82, at two resolutions, $36'' \times 22''$(contours, ranging, in intervals of 7 km s^{-1}, from 2553 km s^{-1} at the bottom left to 2609 km s^{-1} at the top right) and $25'' \times 18''$ (greyscale, from 2550 km s^{-1} as lightest to 2630 km s^{-1} as darkest). Crosses mark the locations of the galaxy's optical centre and the GRB.

Table 4.2: Offset HI regions

Region	RA (h m s)	Dec (d ′ ″)	Channel spread (km s^{-1})	Percentage mass
a	19 35 6.7	−52 51 04	2553.2-2602.1	12
b	19 35 2.1	−52 51 20	2560.2-2574.2	04
c†	19 35 9.4	−52 49 55	2581.2-2588.2	02
d	19 35 9.0	−52 50 31	2595.2-2602.1	03
e	19 35 3.6	−52 51 07	2623.1-2630.1	02

† Region c is spatially, not kinematically, offset from the main disk.

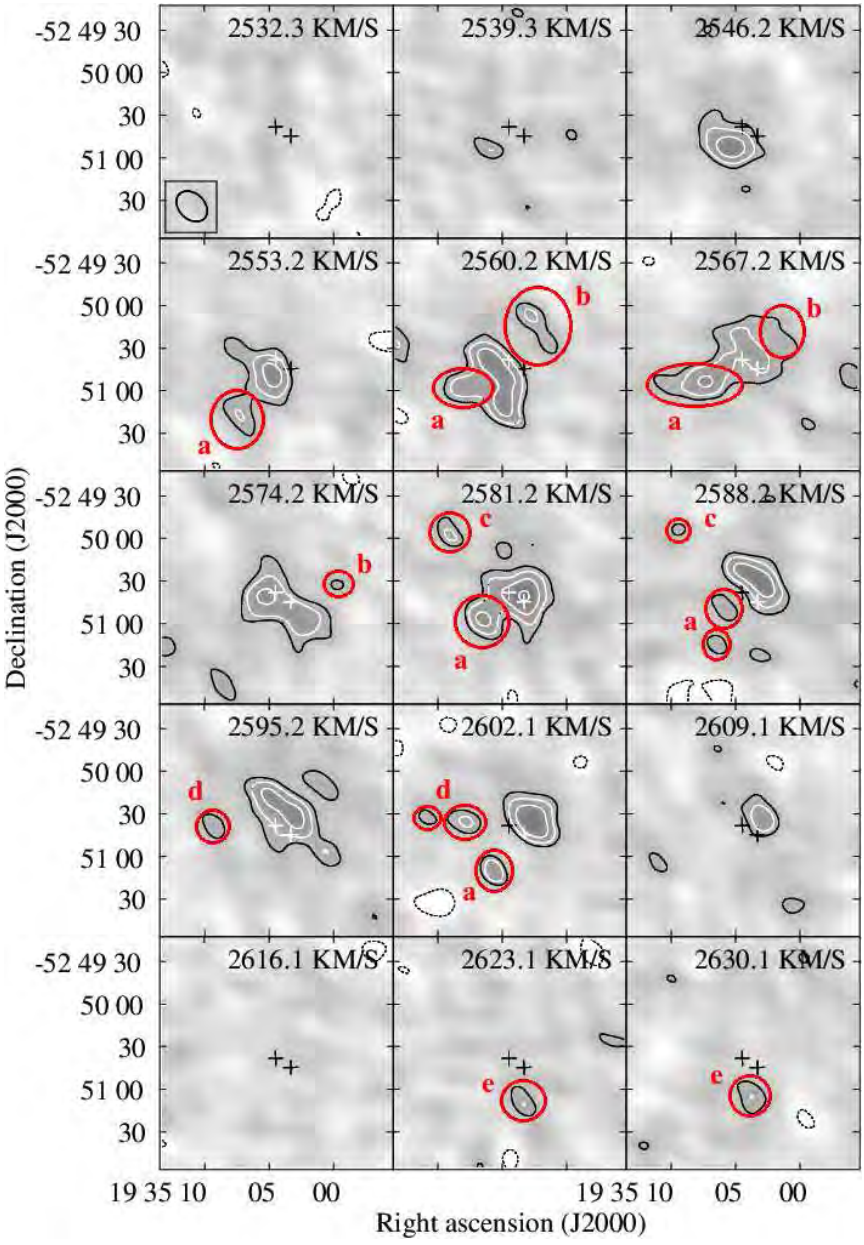

Figure 4.4: HI 21 cm emission from individual (7 km s^{-1}) velocity channels at $25'' \times 18''$ resolution. Crosses mark the locations of the galaxy's optical centre and the GRB. The outermost positive (solid) contour is at 2.5 σ level (7×10^{19} cm^{-2}), with each subsequent contour spaced at intervals of $\sqrt{2}$; the negative (dashed) contours are at -2.5 σ level. Regions with offset velocity (see main text) are marked in the channels in which they appear, following the nomenclature of Table 4.2.

GRB host galaxies, is one of the most luminous and infrared-bright HII regions identified to date in the nearby Universe. It contributes substantially to the host emission at the far- infrared, millimetre, and radio wavelengths – something rarely observed in similar galaxies (Le Floc'h et al., 2006, 2012; Michałowski et al., 2009, 2014). The total infrared luminosity of the W-R region is 5×10^8 $L_{\odot}$, which places it at the very bright end of the luminosity function of HII regions. Moreover, it has one of the highest star formation densities amongst isolated HII regions. Similar extra-nuclear, compact, star-forming complexes are rare, and usually found in starburst galaxies with far higher mass and SFR (Le Floc'h et al., 2012). We note that it has been suggested that the progenitor of the GRB was a runaway massive star ejected from this high stellar density W-R region (Hammer et al., 2006).

The origin of this W-R region has so far not been clear. Spectroscopic observations show that the six galaxies in the field of ESO 184-G82 are not associated with it, and hence, interactions with them could not have triggered such an episode of star formation (Foley et al., 2006). The HI 21 cm data, in agreement with the findings from optical spectroscopy, do not show any evidence of a large companion that might distort the velocity field of ESO 184-G82 via tidal interactions or a major merger. But interestingly, our detailed study of the spatial and kinematic structure of the HI in the galaxy shows that the gas is significantly disturbed, with more than 21% of the gas mass not following the rotation of the main gas disk. There are several cases in the literature where galaxies with small companions (with $\sim$10% of the galaxy mass), or even no detected companions, show peculiar HI structure and/or disturbed HI kinematics; the disturbed velocity field in such systems is believed to arise from minor mergers (for e.g. see Sancisi et al., 2008). This is a likely scenario for ESO 184-G82. The encounter that led to the disturbed HI distribution must have taken place relatively recently, given that its tidal effects have not been damped out by the rotation of the galaxy and the disturbed gas has remained rotationally mis-aligned with the main disk. This puts an upper limit of a few hundred Myrs, equal to the rotation period of the galaxy disk, on the time of occurrence of the encounter. Conversely, the presence of kinematically disturbed gas regions throughout the HI disk (see Figure 4.4) suggest that the encounter occurred sufficiently early on for its tidal effects to disrupt the entire HI disk. Indeed, this disruption is likely to have given rise to the W-R region. This hypothesis is corroborated by the piling up of high HI column density, clumpy gas on the west side of the galaxy, which suggests shock compression of the gas, forming a high density region in which the W-R region and GRB are located, and possibly giving rise to extreme star formation. The disturbed HI kinematics and spatial structure of ESO 184-G82 hence suggests that a minor merger in the recent past is the likely cause of the uncommon properties of the W-R region in the galaxy, which, in turn, may have led to the formation of the gamma ray burst. Finally, we obtain N(HI) $> 5 \times 10^{20}$ cm^{-2} (higher than the damped Lyman-α threshold of 2×10^{20} cm^{-2}; Wolfe et al., 2005), towards the GRB location. This is consistent with the high N(HI) values typically obtained in absorption studies of GRB host galaxies at z $\gtrsim$ 2 (e.g. Fynbo et al., 2009). Here, with the first HI 21 cm emission mapping of a GRB host, we show that the close environment of the GRB is coincident with the highest N(HI) region of the galaxy (see Fig. 4.2). To confirm whether high column densities are typical of GRB environments, systematic high resolution HI 21 cm emission mapping of a sample of GRB host galaxies is required.

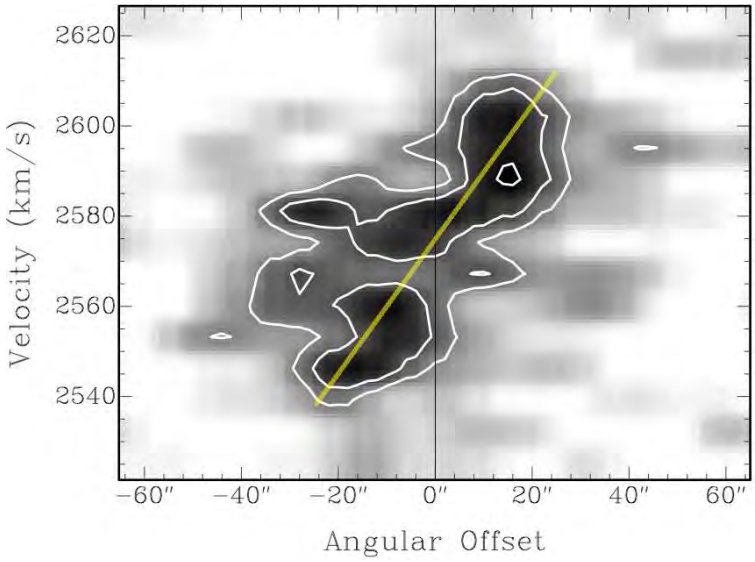

Figure 4.5: A position-velocity cut through the $25'' \times 18''$ spectral cube along the major axis of the galaxy (PA: $\sim 130^{\circ}$ east of north). The angular offset increases from south-east to north-west, with the galaxy centre at zero angular offset. The outermost contour is at the 3 σ level (8.4×10^{19} cm^{-2}), with each subsequent contour spaced in intervals of $\sqrt{2}$. Fluxes are measured within a beam centred at each pixel along the p-v cut. The faint yellow line indicates the main rotating gas disk.

Acknowledgments

We thank Johan Fynbo, Jayaram Chengalur, and especially Palle Møller, for very helpful discussions and comments. We also thank the referee, Ger de Bruyn, for a detailed and helpful report. NK thanks the DST for support via a Swarnajayanti Fellowship. We thank the GMRT staff for having made possible the observations used in this paper. The GMRT is run by the National Centre for Radio Astrophysics of the Tata Institute of Fundamental Research. This paper includes archived data obtained through the Australia Telescope Online Archive. Some of the data presented in this paper were obtained from the Mikulski Archive for Space Telescopes (MAST). STScI is operated by the Association of Universities for Research in Astronomy, Inc., under NASA contract NAS5-26555. Support for MAST for non-HST data is provided by the NASA Office of Space Science via grant NNX13AC07G and by other grants and contracts.

Chapter 5

The last Chapter

Theses come and go, but this Oktoberfest will never return.
S.R., September 2016

GRB host galaxies provide the unique opportunity of simultaneously studying their different gas phases, using both GRBs' and hosts' spectra. This includes investigating the kinematics characteristics of the gas, through both absorption and emission methods, which provides invaluable information on the structure of galaxies and processes involved in their formation and evolution. I have carried out a comprehensive study of gas kinematics in GRB host galaxies in three steps:

I. Investigating what can be learnt from the spatially averaged velocity, measured for both neutral gas (the width of the ISM absorption profiles in GRBs' spectra), and ionised gas (the width of the bright emission lines in the hosts' spectra or in some cases in GRBs' spectra), in a large GRB host sample.

II. Comparing the findings obtained for the two gas phases from the two methods.

III. Pioneering a project for studying the spatially resolved distribution, structure, and kinematics of neutral gas with high velocity resolutions by mapping the HI 21 cm line emission from GRB host galaxies.

My findings are as follows:

i. The spatially averaged velocity of gas correlates well with gas metallicity. This is regardless of the phase of gas and so the method (absorption or emission) used for the measurements. This points towards a direct connection between gas velocity and stellar mass (MZ relation).

ii. The correlation between velocity width and metallicity appears to evolve with redshift. This too reminds of the redshift evolution of the mass-metallicity (MZ) relation.

iii. The spatially averaged velocity of ionised gas correlates well with stellar mass. This appears to also be the case for the velocity width of neutral gas obtained from absorption, though based on a small sample. This is of course a direct proof that the kinematics of gas can be used as a proxy of stellar mass. Such a finding however should not come as a surprise, as stellar mass and all the components contributing to gas kinematics must be controlled by the gravitational potential in the galaxy. Having the velocity width representing the stellar mass in these galaxies automatically makes the VZ correlation a proxy for the MZ relation.

iv. As expected, the MZ relation indeed holds for GRB host galaxies.

v. The spatially averaged velocities obtained from the two methods correlate with each other (as is evident from the previous points), though with absorption velocities being unexpectedly larger than the emission velocities. The contribution of outflowing and infalling gas seem not to be enough to account for the large absorption velocity widths. Merging events are the possible cause behind the large velocity widths of neutral gas measured through absorption method.

vi. Comparing the mentioned scaling relations in absorption and emission, a relation between metallicities measured from absorption and emission methods can be inferred. The inferred relation shows that the two metallicity measurements differ form each other with a decrease in the deviation with an increase in redshift.

vii. The first spatially resolved kinematics study of atomic hydrogen (HI) in a GRB host (mapping the HI 21 cm emission line) clearly reveals that the gas is disturbed, with a large fraction of gas being kinematically offset from the main gas disk of the galaxy. This is most probably a result of a minor merger which could also have triggered the recent star-formation episode in the GRB environment. Further similar studies for a large sample of GRB hosts would be much of interest.

In the light of comparing GRB hosts with other population of galaxies:

viii. GRB-DLAs clearly fall on the same velocity-metallicity (VZ) relation as the QSO-DLAs, and with the same redshift evolution. This implies that the QSO-DLA systems, for which very little is known on mass and star formation, are consistent with being drawn from the population of low mass and low luminosity star forming galaxies, same as GRB hosts. Also, having the velocity width as a proxy of mass makes it possible to use the velocity width measurements of the QSO-DLAs in order to estimate their stellar masses, a property which has proven to be extremely challenging to measure using usual methods of stellar mass measurements for this high-z galaxy population.

ix. GRB hosts appear to obey the same mass-metallicity relation as the general star-forming galaxy population (when the redshift evolution of the relation is taken into account). This is contradictory with the findings of several previous studies that claim GRB hosts to fall below the MZ relation of the general star-forming galaxy population.

GRB hosts galaxies, as a population of star-forming galaxies, are known to have particular characteristics, such as low metallicities, high densities of star-formation and stellar mass, high sSFRs, high column densities of neutral gas, low gas consumption time-scales etc.. Some of these could be only the artefacts of selection methods or small sample sizes. For instance, the high N(HI) values of GRB-DLAs compared to QSO-DLAS could be a result of the smaller impact parameters for GRBs, and the fact that GRBs' light passes through the most actively star-forming regions of their hosts. This can be seen clearly in the HI map of GRB 980425's host, where the GRB position is coincident with the highest N(HI) region in the galaxy, while the extent of the HI gas with lower column densities exceeds much beyond the star-forming regions of the galaxy. One should also do a fair comparison between GRB hosts and other galaxy populations by choosing the samples within similar redshift ranges.

The studies presented in this thesis show that GRB hosts follow the same scaling relations as other galaxy populations which means that same physical processes are responsible for the formation and evolution of this galaxy population as in others. It would have indeed been surprising had this not been the case. In fact it seems that at higher redshifts GRB hosts do not have properties that are distinct from those of typical galaxies at similar redshifts. GRBs clearly choose a subset of galaxies with specific properties, but this does not make them behave peculiarly and differently from other galaxy populations.

Bibliography

Aloy, M. A., Müller, E., Ibáñez, J. M., Martí, J. M., and MacFadyen, A. *ApJL*, 531:L119–L122, Mar. 2000.

Appenzeller, I., Fricke, K., Fürtig, W., Gässler, W., et al. *The Messenger*, 94:1–6, Dec. 1998.

Arabsalmani, M., Møller, P., Fynbo, J. P. U., Christensen, L., et al. *MNRAS*, 446:990–999, Jan. 2015a.

Arabsalmani, M., Roychowdhury, S., Zwaan, M. A., Kanekar, N., and Michałowski, M. J. *MNRAS*, 454:L51–L55, Nov. 2015b.

Arnouts, S., Cristiani, S., Moscardini, L., Matarrese, S., et al. *MNRAS*, 310:540–556, Dec. 1999.

Baldry, I. K. and Glazebrook, K. *ApJ*, 593:258–271, Aug. 2003.

Band, D., Matteson, J., Ford, L., Schaefer, B., et al. *ApJ*, 413:281–292, Aug. 1993.

Barai, P., Monaco, P., Murante, G., Ragagnin, A., and Viel, M. *MNRAS*, 447:266–286, Feb. 2015.

Barnes, L. A., Haehnelt, M. G., Tescari, E., and Viel, M. *MNRAS*, 416:1723–1738, Sept. 2011.

Begum, A., Chengalur, J. N., Karachentsev, I. D., Sharina, M. E., and Kaisin, S. S. *MNRAS*, 386: 1667–1682, May 2008.

Belli, S., Jones, T., Ellis, R. S., and Richard, J. *ApJ*, 772:141, Aug. 2013.

Berger, E., Kulkarni, S. R., and Frail, D. A. *ApJ*, 560:652–658, Oct. 2001.

Berger, E., Penprase, B. E., Cenko, S. B., Kulkarni, S. R., et al. *ApJ*, 642:979–988, May 2006.

Bersier, D., Fruchter, A. S., Strolger, L.-G., Gorosabel, J., et al. *ApJ*, 643:284–291, May 2006.

Bird, S., Haehnelt, M., Neeleman, M., Genel, S., Vogelsberger, M., and Hernquist, L. *MNRAS*, 447: 1834–1846, Feb. 2015.

Blanchard, P. K., Berger, E., and Fong, W.-f. *ApJ*, 817:144, Feb. 2016.

Bloom, J. S., Kulkarni, S. R., Djorgovski, S. G., Eichelberger, A. C., et al. *Nature*, 401:453–456, Sept. 1999.

Bloom, J. S., Kulkarni, S. R., and Djorgovski, S. G. *AJ*, 123:1111–1148, Mar. 2002.

Böhm, A., Ziegler, B. L., Saglia, R. P., Bender, R., et al. *A&A*, 420:97–114, June 2004.

Bolatto, A. D., Wolfire, M., and Leroy, A. K. *ARA&A*, 51:207–268, Aug. 2013.

Bordoloi, R., Lilly, S. J., Hardmeier, E., Contini, T., et al. *ApJ*, 794:130, Oct. 2014.

Bothwell, M. S., Wagg, J., Cicone, C., Maiolino, R., et al. *MNRAS*, 445:2599–2620, Dec. 2014.

Bruzual, G. and Charlot, S. *MNRAS*, 344:1000–1028, Oct. 2003.

Calzetti, D., Armus, L., Bohlin, R. C., Kinney, A. L., Koornneef, J., and Storchi-Bergmann, T. *ApJ*, 533:682–695, Apr. 2000.

Campisi, M. A., Tapparello, C., Salvaterra, R., Mannucci, F., and Colpi, M. *MNRAS*, 417:1013–1021, Oct. 2011.

Castro, S., Galama, T. J., Harrison, F. A., Holtzman, J. A., et al. *ApJ*, 586:128–134, Mar. 2003.

Castro Cerón, J. M., Michałowski, M. J., Hjorth, J., Watson, D., Fynbo, J. P. U., and Gorosabel, J. *ApJL*, 653:L85–L88, Dec. 2006.

Castro Cerón, J. M., Michałowski, M. J., Hjorth, J., Malesani, D., et al. *ApJ*, 721:1919–1927, Oct. 2010.

Castro-Tirado, A. J., Møller, P., García-Segura, G., Gorosabel, J., et al. *A&A*, 517:A61, July 2010.

Catinella, B. and Cortese, L. *MNRAS*, 446:3526–3544, Feb. 2015.

Chabrier, G. *PASP*, 115:763–795, July 2003.

Chary, R., Becklin, E. E., and Armus, L. *ApJ*, 566:229–238, Feb. 2002.

Chen, H.-W. *MNRAS*, 419:3039–3047, Feb. 2012.

Chen, H.-W., Prochaska, J. X., Bloom, J. S., and Thompson, I. B. *ApJL*, 634:L25–L28, Nov. 2005.

Chen, H.-W., Prochaska, J. X., Ramirez-Ruiz, E., Bloom, J. S., Dessauges-Zavadsky, M., and Foley, R. J. *ApJ*, 663:420–436, July 2007.

Chen, H.-W., Perley, D. A., Pollack, L. K., Prochaska, J. X., et al. *ApJ*, 691:152–174, Jan. 2009.

Chisholm, J., Tremonti, C. A., Leitherer, C., Chen, Y., Wofford, A., and Lundgren, B. *ApJ*, 811: 149, Oct. 2015.

Chornock, R., Berger, E., Fox, D. B., Fong, W., Laskar, T., and Roth, K. C. *ArXiv e-prints*, May 2014.

Christensen, L., Hjorth, J., and Gorosabel, J. *A&A*, 425:913–926, Oct. 2004.

Christensen, L., Vreeswijk, P. M., Sollerman, J., Thöne, C. C., Le Floc'h, E., and Wiersema, K. *A&A*, 490:45–59, Oct. 2008.

Christensen, L., Laursen, P., Richard, J., Hjorth, J., et al. *MNRAS*, 427:1973–1982, Dec. 2012.

Christensen, L., Møller, P., Fynbo, J. P. U., and Zafar, T. *MNRAS*, 445:225–238, Nov. 2014.

Cucchiara, A., Fumagalli, M., Rafelski, M., Kocevski, D., et al. *ApJ*, 804:51, May 2015.

Cucchiara, A., Totani, T., and Tanvir, N. *SSRv*, May 2016.

Cullen, F., Cirasuolo, M., McLure, R. J., Dunlop, J. S., and Bowler, R. A. A. *MNRAS*, 440:2300–2312, May 2014.

De Cia, A., Jakobsson, P., Björnsson, G., Vreeswijk, P. M., et al. *MNRAS*, 412:2229–2240, Apr. 2011.

de Ugarte Postigo, A., Goldoni, P., Thöne, C. C., Vergani, S. D., et al. *A&A*, 513:A42, Apr. 2010.

de Ugarte Postigo, A., Campana, S., Thöne, C. C., D'Avanzo, P., et al. *A&A*, 557:L18, Sept. 2013.

Dekel, A. and Woo, J. *MNRAS*, 344:1131–1144, Oct. 2003.

D'Elia, V., Fynbo, J. P. U., Covino, S., Goldoni, P., et al. *A&A*, 523:A36, Nov. 2010.

D'Elia, V., Campana, S., Covino, S., D'Avanzo, P., Piranomonte, S., and Tagliaferri, G. *MNRAS*, 418:680–690, Nov. 2011.

D'Elia, V., Fynbo, J. P. U., Goldoni, P., Covino, S., et al. *A&A*, 564:A38, Apr. 2014.

Djorgovski, S. G., Kulkarni, S. R., Bloom, J. S., Goodrich, R., et al. *ApJL*, 508:L17–L20, Nov. 1998.

Djorgovski, S. G., Frail, D. A., Kulkarni, S. R., Bloom, J. S., Odewahn, S. C., and Diercks, A. *ApJ*, 562:654–663, Dec. 2001.

Doyle, M. T. and Drinkwater, M. J. *MNRAS*, 372:977–991, Nov. 2006.

Elíasdóttir, Á., Fynbo, J. P. U., Hjorth, J., Ledoux, C., et al. *ApJ*, 697:1725–1740, June 2009.

Elliott, J., Greiner, J., Khochfar, S., Schady, P., Johnson, J. L., and Rau, A. *A&A*, 539:A113, Mar. 2012.

Elliott, J., Krühler, T., Greiner, J., Savaglio, S., et al. *A&A*, 556:A23, Aug. 2013a.

Elliott, J., Krühler, T., Greiner, J., Savaglio, S., et al. *A&A*, 556:A23, Aug. 2013b.

Ellison, S. L., Kanekar, N., Prochaska, J. X., Momjian, E., and Worseck, G. *MNRAS*, 424:293–312, July 2012.

Epinat, B., Tasca, L., Amram, P., Contini, T., et al. *A&A*, 539:A92, Mar. 2012.

Erb, D. K., Shapley, A. E., Pettini, M., Steidel, C. C., Reddy, N. A., and Adelberger, K. L. *ApJ*, 644:813–828, June 2006.

Fernández, X., Gim, H. B., van Gorkom, J. H., Yun, M. S., et al. *ApJL*, 824:L1, June 2016.

Filgas, R., Greiner, J., Schady, P., Krühler, T., et al. *A&A*, 535:A57, Nov. 2011a.

Filgas, R., Krühler, T., Greiner, J., Rau, A., et al. *A&A*, 526:A113, Feb. 2011b.

Flores, H., Hammer, F., Puech, M., Amram, P., and Balkowski, C. *A&A*, 455:107–118, Aug. 2006.

Foley, S., Watson, D., Gorosabel, J., Fynbo, J. P. U., et al. *A&A*, 447:891–895, Mar. 2006.

Förster Schreiber, N. M., Genzel, R., Bouché, N., Cresci, G., et al. *ApJ*, 706:1364–1428, Dec. 2009.

Fox, A. J., Ledoux, C., Vreeswijk, P. M., Smette, A., and Jaunsen, A. O. *A&A*, 491:189–207, Nov. 2008.

Frail, D. A., Bertoldi, F., Moriarty-Schieven, G. H., Berger, E., et al. *ApJ*, 565:829–835, Feb. 2002.

Friis, M., De Cia, A., Krühler, T., Fynbo, J. P. U., et al. *MNRAS*, 451:167–183, July 2015a.

Friis, M., De Cia, A., Krühler, T., Fynbo, J. P. U., et al. *MNRAS*, 451:167–183, July 2015b.

Fruchter, A. S., Thorsett, S. E., Metzger, M. R., Sahu, K. C., et al. *ApJL*, 519:L13–L16, July 1999.

Fruchter, A. S., Levan, A. J., Strolger, L., Vreeswijk, P. M., et al. *Nature*, 441:463–468, May 2006.

Fynbo, J. P. U., Starling, R. L. C., Ledoux, C., Wiersema, K., et al. *A&A*, 451:L47–L50, June 2006.

Fynbo, J. P. U., Prochaska, J. X., Sommer-Larsen, J., Dessauges-Zavadsky, M., and Møller, P. *ApJ*, 683:321-328, Aug. 2008.

Fynbo, J. P. U., Jakobsson, P., Prochaska, J. X., Malesani, D., et al. *ApJS*, 185:526–573, Dec. 2009.

Fynbo, J. P. U., Geier, S. J., Christensen, L., Gallazzi, A., et al. *MNRAS*, 436:361–370, Nov. 2013.

Fynbo, J. P. U., Krühler, T., Leighly, K., Ledoux, C., et al. *A&A*, 572:A12, Dec. 2014.

Fynbo, J. U., Møller, P., and Warren, S. J. *MNRAS*, 305:849–858, May 1999.

Fynbo, J. U., Holland, S., Andersen, M. I., Thomsen, B., et al. *ApJL*, 542:L89–L93, Oct. 2000.

Fynbo, J. U., Gorosabel, J., Dall, T. H., Hjorth, J., et al. *A&A*, 373:796–804, July 2001.

Galama, T. J., Vreeswijk, P. M., van Paradijs, J., Kouveliotou, C., et al. *Nature*, 395:670–672, Oct. 1998.

Gehrels, N., Ramirez-Ruiz, E., and Fox, D. B. *ARA&A*, 47:567–617, Sept. 2009.

Genzel, R., Burkert, A., Bouché, N., Cresci, G., et al. *ApJ*, 687:59-77, Nov. 2008.

Genzel, R., Newman, S., Jones, T., Förster Schreiber, N. M., et al. *ApJ*, 733:101, June 2011.

Glazebrook, K. *PASA*, 30:e056, Nov. 2013.

Glazebrook, K., Abraham, R. G., McCarthy, P. J., Savaglio, S., et al. *Nature*, 430:181–184, July 2004.

Gnerucci, A., Marconi, A., Cresci, G., Maiolino, R., et al. *A&A*, 528:A88, Apr. 2011.

Gorosabel, J., Pérez-Ramírez, D., Sollerman, J., de Ugarte Postigo, A., et al. *A&A*, 444:711–721, Dec. 2005.

Graham, J. F. and Fruchter, A. S. *ApJ*, 774:119, Sept. 2013.

Greiner, J., Bornemann, W., Clemens, C., Deuter, M., et al. *PASP*, 120:405–424, Apr. 2008.

Greiner, J., Krühler, T., Klose, S., Afonso, P., et al. In McEnery, J. E., Racusin, J. L., and Gehrels, N., editors, *American Institute of Physics Conference Series*, volume 1358 of *American Institute of Physics Conference Series*, pages 121–124, Aug. 2011.

Greiner, J., Fox, D. B., Schady, P., Krühler, T., et al. *ApJ*, 809:76, Aug. 2015.

Hammer, F., Flores, H., Schaerer, D., Dessauges-Zavadsky, M., Le Floc'h, E., and Puech, M. *A&A*, 454:103–111, July 2006.

Hartoog, O. E., Malesani, D., Fynbo, J. P. U., Goto, T., et al. *A&A*, 580:A139, Aug. 2015.

Hashimoto, T., Ohta, K., Aoki, K., Tanaka, I., et al. *ApJ*, 719:378–384, Aug. 2010.

Hatsukade, B., Ohta, K., Endo, A., Nakanishi, K., et al. *Nature*, 510:247–249, June 2014.

Heckman, T. M., Alexandroff, R. M., Borthakur, S., Overzier, R., and Leitherer, C. *ApJ*, 809:147, Aug. 2015.

Henry, A., Scarlata, C., Domínguez, A., Malkan, M., et al. *ApJL*, 776:L27, Oct. 2013.

Hidalgo-Gámez, A. M., Olofsson, K., and Masegosa, J. *A&A*, 367:388–404, Feb. 2001.

Hjorth, J. and Bloom, J. S. *The Gamma-Ray Burst - Supernova Connection*, pages 169–190. Nov. 2012.

Hjorth, J., Møller, P., Gorosabel, J., Fynbo, J. P. U., et al. *ApJ*, 597:699–705, Nov. 2003a.

Hjorth, J., Sollerman, J., Møller, P., Fynbo, J. P. U., et al. *Nature*, 423:847–850, June 2003b.

Hjorth, J., Malesani, D., Jakobsson, P., Jaunsen, A. O., et al. *ApJ*, 756:187, Sept. 2012a.

Hjorth, J., Malesani, D., Jakobsson, P., Jaunsen, A. O., et al. *ApJ*, 756:187, Sept. 2012b.

Hunt, L., Palazzi, E., Rossi, A., Savaglio, S., et al. *ApJL*, 736:L36, Aug. 2011.

Ilbert, O., Arnouts, S., McCracken, H. J., Bolzonella, M., et al. *A&A*, 457:841–856, Oct. 2006.

Jakobsson, P., Hjorth, J., Fynbo, J. P. U., Weidinger, M., et al. *A&A*, 427:785–794, Dec. 2004.

Jensen, B. L., Fynbo, J. U., Gorosabel, J., Hjorth, J., et al. *A&A*, 370:909–922, May 2001.

Karman, W., Caputi, K. I., Trager, S. C., Almaini, O., and Cirasuolo, M. *A&A*, 565:A5, May 2014.

Kelly, P. L., Filippenko, A. V., Fox, O. D., Zheng, W., and Clubb, K. I. *ApJL*, 775:L5, Sept. 2013.

Kelly, P. L., Filippenko, A. V., Modjaz, M., and Kocevski, D. *ApJ*, 789:23, July 2014.

Kewley, L. J., Brown, W. R., Geller, M. J., Kenyon, S. J., and Kurtz, M. J. *AJ*, 133:882–888, Mar. 2007.

Kissler-Patig, M., Pirard, J.-F., Casali, M., Moorwood, A., et al. *A&A*, 491:941–950, Dec. 2008.

Klebesadel, R. W., Strong, I. B., and Olson, R. A. *ApJL*, 182:L85, June 1973.

Kocevski, D. and West, A. A. *ApJL*, 735:L8, July 2011.

Kocevski, D., West, A. A., and Modjaz, M. *ApJ*, 702:377–385, Sept. 2009.

Krogager, J.-K., Fynbo, J. P. U., Møller, P., Ledoux, C., et al. *MNRAS*, 424:L1–L5, July 2012.

Krogager, J.-K., Fynbo, J. P. U., Ledoux, C., Christensen, L., et al. *MNRAS*, 433:3091–3102, Aug. 2013a.

Krogager, J.-K., Fynbo, J. P. U., Ledoux, C., Christensen, L., et al. *MNRAS*, 433:3091–3102, Aug. 2013b.

Krühler, T., Greiner, J., Schady, P., Savaglio, S., et al. *A&A*, 534:A108, Oct. 2011a.

Krühler, T., Greiner, J., Schady, P., Savaglio, S., et al. *A&A*, 534:A108, Oct. 2011b.

Krühler, T., Malesani, D., Milvang-Jensen, B., Fynbo, J. P. U., et al. *ApJ*, 758:46, Oct. 2012.

Krühler, T., Ledoux, C., Fynbo, J. P. U., Vreeswijk, P. M., et al. *A&A*, 557:A18, Sept. 2013.

Krühler, T., Malesani, D., Fynbo, J. P. U., Hartoog, O. E., et al. *A&A*, 581:A125, Sept. 2015.

Lagos, C. d. P., Lacey, C. G., and Baugh, C. M. *MNRAS*, 436:1787–1817, Dec. 2013.

Lah, P., Pracy, M. B., Chengalur, J. N., Briggs, F. H., et al. *MNRAS*, 399:1447–1470, Nov. 2009.

Langer, N. and Norman, C. A. *ApJL*, 638:L63–L66, Feb. 2006.

Law, D. R., Steidel, C. C., Erb, D. K., Pettini, M., et al. *ApJ*, 656:1–26, Feb. 2007.

Law, D. R., Steidel, C. C., Erb, D. K., Larkin, J. E., et al. *ApJ*, 697:2057–2082, June 2009.

Le Floc'h, E., Duc, P.-A., Mirabel, I. F., Sanders, D. B., et al. *A&A*, 400:499–510, Mar. 2003.

Le Floc'h, E., Charmandaris, V., Forrest, W. J., Mirabel, I. F., Armus, L., and Devost, D. *ApJ*, 642: 636–652, May 2006.

Le Floc'h, E., Charmandaris, V., Gordon, K., Forrest, W. J., et al. *ApJ*, 746:7, Feb. 2012.

Ledoux, C., Bergeron, J., and Petitjean, P. *A&A*, 385:802–815, Apr. 2002.

Ledoux, C., Petitjean, P., Fynbo, J. P. U., Møller, P., and Srianand, R. *A&A*, 457:71–78, Oct. 2006.

Ledoux, C., Vreeswijk, P. M., Smette, A., Fox, A. J., et al. *A&A*, 506:661–675, Nov. 2009.

Lemoine-Busserolle, M. and Lamareille, F. *MNRAS*, 402:2291–2307, Mar. 2010.

Lemoine-Busserolle, M., Bunker, A., Lamareille, F., and Kissler-Patig, M. *MNRAS*, 401:1657–1669, Jan. 2010.

Levesque, E. M. *PASP*, 126:1–14, Jan. 2014.

Levesque, E. M., Berger, E., Kewley, L. J., and Bagley, M. M. *AJ*, 139:694–711, Feb. 2010a.

Levesque, E. M., Kewley, L. J., Berger, E., and Zahid, H. J. *AJ*, 140:1557–1566, Nov. 2010b.

Levesque, E. M., Kewley, L. J., Graham, J. F., and Fruchter, A. S. *ApJL*, 712:L26–L30, Mar. 2010c.

Lien, A., Sakamoto, T., Gehrels, N., Palmer, D. M., et al. *ApJ*, 783:24, Mar. 2014.

Lu, L., Sargent, W. L. W., Barlow, T. A., Churchill, C. W., and Vogt, S. S. *ApJS*, 107:475, Dec. 1996.

MacFadyen, A. I. and Woosley, S. E. *ApJ*, 524:262–289, Oct. 1999.

Maiolino, R., Nagao, T., Grazian, A., Cocchia, F., et al. *A&A*, 488:463–479, Sept. 2008.

Mannucci, F., Cresci, G., Maiolino, R., Marconi, A., and Gnerucci, A. *MNRAS*, 408:2115–2127, Nov. 2010.

Mannucci, F., Salvaterra, R., and Campisi, M. A. *MNRAS*, 414:1263–1268, June 2011.

Mazets, E. P., Golenetskii, S. V., Ilinskii, V. N., Gurian, I. A., and Kharitonova, T. V. *ZhETF Pisma Redaktsiiu*, 20:77–80, July 1974.

McBreen, S., Krühler, T., Rau, A., Greiner, J., et al. *A&A*, 516:A71, June 2010a.

McBreen, S., Krühler, T., Rau, A., Greiner, J., et al. *A&A*, 516:A71, June 2010b.

McGuire, J. T. W., Tanvir, N. R., Levan, A. J., Trenti, M., et al. *ApJ*, 825:135, July 2016.

Michałowski, M. J., Hjorth, J., Malesani, D., Michałowski, T., et al. *ApJ*, 693:347–354, Mar. 2009.

Michałowski, M. J., Kamble, A., Hjorth, J., Malesani, D., et al. *ApJ*, 755:85, Aug. 2012.

Michałowski, M. J., Hunt, L. K., Palazzi, E., Savaglio, S., et al. *A&A*, 562:A70, Feb. 2014.

Miller, S. H., Bundy, K., Sullivan, M., Ellis, R. S., and Treu, T. *ApJ*, 741:115, Nov. 2011.

Modjaz, M., Kewley, L., Kirshner, R. P., Stanek, K. Z., et al. *AJ*, 135:1136–1150, Apr. 2008.

Møller, P. and Warren, S. J. *MNRAS*, 299:661–671, Sept. 1998.

Møller, P., Warren, S. J., Fall, S. M., Fynbo, J. U., and Jakobsen, P. *ApJ*, 574:51–58, July 2002.

Møller, P., Fynbo, J. P. U., Ledoux, C., and Nilsson, K. K. *MNRAS*, 430:2680–2687, Apr. 2013.

Morgan, A. N., Perley, D. A., Cenko, S. B., Bloom, J. S., et al. *MNRAS*, 440:1810–1823, May 2014.

Neeleman, M., Wolfe, A. M., Prochaska, J. X., and Rafelski, M. *ApJ*, 769:54, May 2013.

Noterdaeme, P., Ledoux, C., Petitjean, P., and Srianand, R. *A&A*, 481:327–336, Apr. 2008.

Noterdaeme, P., Petitjean, P., Ledoux, C., and Srianand, R. *A&A*, 505:1087–1098, Oct. 2009.

Nuza, S. E., Tissera, P. B., Pellizza, L. J., Lambas, D. G., Scannapieco, C., and de Rossi, M. E. *MNRAS*, 375:665–672, Feb. 2007.

Paczyński, B. *ApJL*, 494:L45–L48, Feb. 1998.

Pérez-Ramírez, D., Norris, J. P., Gorosabel, J., Castro-Tirado, A. J., et al. In Castro-Tirado, A. J., Gorosabel, J., and Park, I. H., editors, *EAS Publications Series*, volume 61 of *EAS Publications Series*, pages 345–349, July 2013.

Perley, D. A., Cenko, S. B., Bloom, J. S., Chen, H.-W., et al. *AJ*, 138:1690–1708, Dec. 2009.

Perley, D. A., Levan, A. J., Tanvir, N. R., Cenko, S. B., et al. *ApJ*, 778:128, Dec. 2013b.

Perley, D. A., Levan, A. J., Tanvir, N. R., Cenko, S. B., et al. *ApJ*, 778:128, Dec. 2013a.

Perley, D. A., Perley, R. A., Hjorth, J., Michałowski, M. J., et al. *ApJ*, 801:102, Mar. 2015.

Perley, D. A., Krühler, T., Schulze, S., de Ugarte Postigo, A., et al. *ApJ*, 817:7, Jan. 2016a.

Perley, D. A., Krühler, T., Schulze, S., de Ugarte Postigo, A., et al. *ApJ*, 817:7, Jan. 2016b.

Perley, D. A., Niino, Y., Tanvir, N. R., Vergani, S. D., and Fynbo, J. P. U. *SSRv*, Mar. 2016c.

Perley, D. A., Tanvir, N. R., Hjorth, J., Laskar, T., et al. *ApJ*, 817:8, Jan. 2016d.

Perley, D. A., Tanvir, N. R., Hjorth, J., Laskar, T., et al. *ApJ*, 817:8, Jan. 2016e.

Péroux, C., Meiring, J. D., Kulkarni, V. P., Ferlet, R., et al. *MNRAS*, 372:369–380, Oct. 2006.

Péroux, C., Meiring, J. D., Kulkarni, V. P., Khare, P., et al. *MNRAS*, 386:2209–2220, June 2008.

Persic, M., Salucci, P., and Stel, F. *MNRAS*, 281:27–47, July 1996.

Pettini, M., Smith, L. J., King, D. L., and Hunstead, R. W. *ApJ*, 486:665–680, Sept. 1997.

Pettini, M., Kellogg, M., Steidel, C. C., Dickinson, M., Adelberger, K. L., and Giavalisco, M. *ApJ*, 508:539–550, Dec. 1998.

Pettini, M., Ellison, S. L., Steidel, C. C., Shapley, A. E., and Bowen, D. V. *ApJ*, 532:65–76, Mar. 2000.

Pettini, M., Shapley, A. E., Steidel, C. C., Cuby, J.-G., et al. *ApJ*, 554:981–1000, June 2001.

Piran, T. *PhR*, 314:575–667, June 1999.

Piranomonte, S., Ward, P. A., Fiore, F., Vergani, S. D., et al. *A&A*, 492:775–785, Dec. 2008.

Podsiadlowski, P., Ivanova, N., Justham, S., and Rappaport, S. *MNRAS*, 406:840–847, Aug. 2010.

Pontzen, A., Governato, F., Pettini, M., Booth, C. M., et al. *MNRAS*, 390:1349–1371, Nov. 2008.

Pontzen, A., Deason, A., Governato, F., Pettini, M., et al. *MNRAS*, 402:1523–1535, Mar. 2010.

Prasad, J. and Chengalur, J. *Experimental Astronomy*, 33:157–171, Mar. 2012.

Price, P. A., Songaila, A., Cowie, L. L., Bell Burnell, J., et al. *ApJL*, 663:L57–L60, July 2007.

Prochaska, J. X. and Wolfe, A. M. *ApJ*, 487:73–95, Sept. 1997.

Prochaska, J. X. and Wolfe, A. M. *ApJ*, 507:113–130, Nov. 1998.

Prochaska, J. X., Gawiser, E., Wolfe, A. M., Castro, S., and Djorgovski, S. G. *ApJL*, 595:L9–L12, Sept. 2003a.

Prochaska, J. X., Gawiser, E., Wolfe, A. M., Cooke, J., and Gelino, D. *ApJS*, 147:227–264, Aug. 2003b.

Prochaska, J. X., Bloom, J. S., Chen, H.-W., Hurley, K. C., et al. *ApJ*, 611:200–207, Aug. 2004.

Prochaska, J. X., Chen, H.-W., Dessauges-Zavadsky, M., and Bloom, J. S. *ApJ*, 666:267–280, Sept. 2007.

Prochaska, J. X., Chen, H.-W., Wolfe, A. M., Dessauges-Zavadsky, M., and Bloom, J. S. *ApJ*, 672: 59-71, Jan. 2008.

Prochaska, J. X., Sheffer, Y., Perley, D. A., Bloom, J. S., et al. *ApJL*, 691:L27–L32, Jan. 2009.

Puech, M., Flores, H., Hammer, F., Yang, Y., et al. *A&A*, 484:173–187, June 2008.

Puech, M., Hammer, F., Flores, H., Delgado-Serrano, R., Rodrigues, M., and Yang, Y. *A&A*, 510: A68, Feb. 2010.

Rafelski, M., Wolfe, A. M., Prochaska, J. X., Neeleman, M., and Mendez, A. J. *ApJ*, 755:89, Aug. 2012.

Richard, J., Jones, T., Ellis, R., Stark, D. P., Livermore, R., and Swinbank, M. *MNRAS*, 413: 643–658, May 2011.

Roberts, M. S. and Rots, A. H. *A&A*, 26:483–485, Aug. 1973.

Robertson, B. E. and Ellis, R. S. *ApJ*, 744:95, Jan. 2012.

Rossi, A., Klose, S., Ferrero, P., Greiner, J., et al. *A&A*, 545:A77, Sept. 2012a.

Rossi, A., Klose, S., Ferrero, P., Greiner, J., et al. *A&A*, 545:A77, Sept. 2012b.

Rubin, V. C. and Ford, Jr., W. K. *ApJ*, 159:379, Feb. 1970.

Rubin, V. C., Thonnard, N., and Ford, Jr., W. K. *ApJL*, 225:L107–L111, Nov. 1978.

Saintonge, A., Kauffmann, G., Kramer, C., Tacconi, L. J., et al. *MNRAS*, 415:32–60, July 2011.

Salvaterra, R., Campana, S., Vergani, S. D., Covino, S., et al. *ApJ*, 749:68, Apr. 2012.

Sancisi, R., Fraternali, F., Oosterloo, T., and van der Hulst, T. *A&ARv*, 15:189–223, June 2008.

Savaglio, S. *New Journal of Physics*, 8:195, Sept. 2006.

Savaglio, S., Glazebrook, K., Le Borgne, D., Juneau, S., et al. *ApJ*, 635:260–279, Dec. 2005.

Savaglio, S., Glazebrook, K., and Le Borgne, D. In Holt, S. S., Gehrels, N., and Nousek, J. A., editors, *Gamma-Ray Bursts in the Swift Era*, volume 836 of *American Institute of Physics Conference Series*, pages 540–545, May 2006.

Savaglio, S., Glazebrook, K., and Le Borgne, D. *ApJ*, 691:182–211, Jan. 2009a.

Savaglio, S., Glazebrook, K., and Le Borgne, D. *ApJ*, 691:182–211, Jan. 2009b.

Savaglio, S., Rau, A., Greiner, J., Krühler, T., et al. *MNRAS*, 420:627–636, Feb. 2012.

Schady, P., Krühler, T., Greiner, J., Graham, J. F., et al. *A&A*, 579:A126, July 2015.

Schulze, S., Malesani, D., Cucchiara, A., Tanvir, N. R., et al. *A&A*, 566:A102, June 2014.

Schulze, S., Chapman, R., Hjorth, J., Levan, A. J., et al. *ApJ*, 808:73, July 2015b.

Schulze, S., Chapman, R., Hjorth, J., Levan, A. J., et al. *ApJ*, 808:73, July 2015a.

Simard, L. and Pritchet, C. J. *ApJ*, 505:96–110, Sept. 1998.

Sofue, Y. and Rubin, V. *ARA&A*, 39:137–174, 2001.

Sokolov, V. V., Fatkhullin, T. A., Castro-Tirado, A. J., Fruchter, A. S., et al. *A&A*, 372:438–455, June 2001.

Sollerman, J., Östlin, G., Fynbo, J. P. U., Hjorth, J., Fruchter, A., and Pedersen, K. *NewA*, 11: 103–115, Nov. 2005.

Sparre, M., Hartoog, O. E., Krühler, T., Fynbo, J. P. U., et al. *ApJ*, 785:150, Apr. 2014.

Stanek, K. Z., Gnedin, O. Y., Beacom, J. F., Gould, A. P., et al. *AcA*, 56:333–345, Dec. 2006.

Stanway, E. R., Levan, A. J., Tanvir, N. R., Wiersema, K., and van der Laan, T. P. R. *ApJL*, 798:L7, Jan. 2015.

Steidel, C. C., Rudie, G. C., Strom, A. L., Pettini, M., et al. *ApJ*, 795:165, Nov. 2014.

Svensson, K. M., Levan, A. J., Tanvir, N. R., Fruchter, A. S., and Strolger, L.-G. *MNRAS*, 405: 57–76, June 2010.

Svensson, K. M., Levan, A. J., Tanvir, N. R., Perley, D. A., et al. *MNRAS*, 421:25–35, Mar. 2012.

Swinbank, A. M., Smail, I., Sobral, D., Theuns, T., Best, P. N., and Geach, J. E. *ApJ*, 760:130, Dec. 2012a.

Swinbank, A. M., Sobral, D., Smail, I., Geach, J. E., et al. *MNRAS*, 426:935–950, Oct. 2012b.

Tanvir, N. R., Fox, D. B., Levan, A. J., Berger, E., et al. *Nature*, 461:1254–1257, Oct. 2009.

Tanvir, N. R., Levan, A. J., Fruchter, A. S., Fynbo, J. P. U., et al. *ApJ*, 754:46, July 2012.

Tescari, E., Viel, M., Tornatore, L., and Borgani, S. *MNRAS*, 397:411–430, July 2009.

Thöne, C. C., Greiner, J., Savaglio, S., and Jehin, E. *ApJ*, 671:628–636, Dec. 2007.

Thöne, C. C., Fynbo, J. P. U., Goldoni, P., de Ugarte, A. P., et al. *MNRAS*, 428:3590–3606, Feb. 2013.

Totani, T. In Roming, P., Kawai, N., and Pian, E., editors, *Death of Massive Stars: Supernovae and Gamma-Ray Bursts*, volume 279 of *IAU Symposium*, pages 241–247, Sept. 2012.

Totani, T., Kawai, N., Kosugi, G., Aoki, K., et al. *PASJ*, 58:485–498, June 2006.

Totani, T., Aoki, K., Hattori, T., Kosugi, G., et al. *PASJ*, 66:63, June 2014.

Totani, T., Aoki, K., Hattori, T., and Kawai, N. *PASJ*, 68:15, Feb. 2016.

Tremonti, C. A., Heckman, T. M., Kauffmann, G., Brinchmann, J., et al. *ApJ*, 613:898–913, Oct. 2004.

Troncoso, P., Maiolino, R., Sommariva, V., Cresci, G., et al. *A&A*, 563:A58, Mar. 2014.

Tully, R. B. and Fisher, J. R. *A&A*, 54:661–673, Feb. 1977.

van Zee, L., Salzer, J. J., Haynes, M. P., O'Donoghue, A. A., and Balonek, T. J. *AJ*, 116:2805–2833, Dec. 1998.

Vergani, S. D., Salvaterra, R., Japelj, J., Le Floc'h, E., et al. *A&A*, 581:A102, Sept. 2015a.

Vergani, S. D., Salvaterra, R., Japelj, J., Le Floc'h, E., et al. *A&A*, 581:A102, Sept. 2015b.

Vogt, N. P., Forbes, D. A., Phillips, A. C., Gronwall, C., et al. *ApJL*, 465:L15, July 1996.

Vreeswijk, P. M., Fender, R. P., Garrett, M. A., Tingay, S. J., Fruchter, A. S., and Kaper, L. *A&A*, 380:L21–L25, Dec. 2001a.

Vreeswijk, P. M., Fruchter, A., Kaper, L., Rol, E., et al. *ApJ*, 546:672–680, Jan. 2001b.

Vreeswijk, P. M., Ellison, S. L., Ledoux, C., Wijers, R. A. M. J., et al. *A&A*, 419:927–940, June 2004.

Watson, D., Fynbo, J. P. U., Ledoux, C., Vreeswijk, P., et al. *ApJ*, 652:1011–1019, Dec. 2006.

Wisnioski, E., Glazebrook, K., Blake, C., Wyder, T., et al. *MNRAS*, 417:2601–2623, Nov. 2011.

Wolf, C. and Podsiadlowski, P. *MNRAS*, 375:1049–1058, Mar. 2007.

Wolfe, A. M. and Prochaska, J. X. *ApJ*, 545:591–602, Dec. 2000.

Wolfe, A. M. and Prochaska, J. X. *ApJL*, 494:L15–L18, Feb. 1998.

Wolfe, A. M., Gawiser, E., and Prochaska, J. X. *ARA&A*, 43:861–918, Sept. 2005.

Wood, C. M., Tremonti, C. A., Calzetti, D., Leitherer, C., Chisholm, J., and Gallagher, J. S. *MNRAS*, 452:2712–2730, Sept. 2015.

Woosley, S. E. *ApJ*, 405:273–277, Mar. 1993.

Woosley, S. E. and Heger, A. *ApJ*, 637:914–921, Feb. 2006.

Wright, S. A., Larkin, J. E., Barczys, M., Erb, D. K., et al. *ApJ*, 658:78–84, Mar. 2007.

Wright, S. A., Larkin, J. E., Law, D. R., Steidel, C. C., Shapley, A. E., and Erb, D. K. *ApJ*, 699: 421–440, July 2009.

Wuyts, E., Rigby, J. R., Sharon, K., and Gladders, M. D. *ApJ*, 755:73, Aug. 2012.

Xu, D., de Ugarte Postigo, A., Leloudas, G., Krühler, T., et al. *ApJ*, 776:98, Oct. 2013.

Yu, H., Wang, F. Y., Dai, Z. G., and Cheng, K. S. *ApJS*, 218:13, May 2015.

Zafar, T., Watson, D., Fynbo, J. P. U., Malesani, D., Jakobsson, P., and de Ugarte Postigo, A. *A&A*, 532:A143, Aug. 2011.

Zaritsky, D., Courtois, H., Muñoz-Mateos, J.-C., Sorce, J., et al. *AJ*, 147:134, June 2014.

Zhang, W., Woosley, S. E., and MacFadyen, A. I. *ApJ*, 586:356–371, Mar. 2003.

Ziegler, B. L., Böhm, A., Fricke, K. J., Jäger, K., et al. *ApJL*, 564:L69–L72, Jan. 2002.

Zwaan, M. A., van der Hulst, J. M., Briggs, F. H., Verheijen, M. A. W., and Ryan-Weber, E. V. *MNRAS*, 364:1467–1487, Dec. 2005.